

Evaluating Tumor Heterogeneity Effects on Transports and Acute Therapeutic Outcomes of Photodynamic Therapy in Pancreatic Adenocarcinoma

A Thesis

Submitted to the Faculty
in partial fulfillment of the requirements for the
degree of

Doctor of Philosophy

In

Engineering Sciences

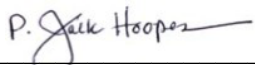
by PHUONG DIEP VINCENT


Thayer School of Engineering
Guarini School of Graduate and Advanced Studies
Dartmouth College
Hanover, New Hampshire

March 2021


Examining Committee:

Chair 
Brian W. Pogue, Ph.D.

Member 
P. Jack Hoopes, DVM, Ph.D.

Member 
Petr Brůža, Ph.D.

Member 
Kimberley S. Samkoe, Ph.D.

Member 
Tayyaba Hasan, Ph.D.

F. Jon Kull, Ph.D.

Dean of the Guarini School of Graduate and Advanced Studies

Abstract

Pancreatic ductal adenocarcinoma (PDAC) is the most common form of pancreatic cancer, yet 80% of the patients are not eligible for curative surgical resection due to the tumor invasion into surrounding major blood vessels. Alternative treatment options, from conventional chemotherapy to more novel approaches such as immunotherapy, mainly rely on systemic drug delivery and intratumoral distribution. While the tumor microenvironment has been established as a key factor that affects drug transport efficiency, it is a challenge to obtain transport-relevant tumor information in clinical settings to assess therapeutic outcomes. This thesis focused on understanding the PDAC tumor microenvironment parameters that could be a surrogate for drug uptake and using low-dose photodynamic therapy (PDT) to modulate such parameters to improve tumor drug distribution. Preclinical findings along with early evidence from clinical CT scans are presented.

The first aim of this thesis introduces an *ex vivo* imaging system that helps demonstrate the relationship between tumor stiffness heterogeneity and tumor collagen content, both of which are inversely correlated to drug uptake. This finding encourages the development of elastography as a feasible clinical imaging procedure that could predict treatment outcome. The second aim further improves the capability of this imaging system to visualize collagen distribution in fresh tissue samples by employing tumor staining and fluorescence imaging with ultraviolet excitation. The system is utilized in the third aim of this thesis which demonstrates that low-dose focal PDT treatment in PDAC mouse models could reduce desmoplasia and relieve stiffness heterogeneity. Such modulating effects of PDT makes this light treatment an effective neoadjuvant therapy to prime PDAC tumors

for subsequent chemo or immunotherapy. Lastly, the fourth aim of this work shows that tumor priming effects could be quantified from CT scans of PDAC patients receiving PDT treatment by texture analysis, emphasizing the promise of PDT when used in combination with more conventional therapies.

Acknowledgements

Looking back upon my journey to pursue a PhD, I realize the most important stepping stones that led to this path are the people that I have met. Professor Darren Roblyer introduced me to the field of biomedical optics with the best guidance a college junior at a loss for career direction could have asked for. At my first job, I had the good fortune to work under the tutelage of Dr. Robert Holt, who motivated me to pursue higher education. I was greatly inspired by the intellectual freedom that often comes only after spending years of technical training. Fortunately, I was surrounded by people that best exemplify this idea at Dartmouth. Their continued support and expert mentoring have had a major impact on my education and greatly contributed to my thesis. In particular, I want to thank:

- Dr. Tayyaba Hasan, for her expertise and guidance on the large scope of my thesis as well as the financial support made possible through NIH grant P01 CA084203.
- Dr. Kimberley Samkoe, for the example she set of having excellent technical skills in both engineering and medicine. I am deeply grateful for the training and mental support I have received from her.
- Dr. Jack Hoopes, for always asking the most interesting questions about my research, and for encouraging me to freely use all the equipment in his lab, especially during the initial phase of my project.
- Dr. Petr Brůža, for his impressive imaging and electronic hardware knowledge base. I am thankful for his candid feedback on my progress and all the moments he made me feel like I needed to work ten times harder.

- Kayla Marra, Jason Gunn and Rendy Strawbridge, for providing me with the best lab support throughout all phases of my experiments, and for lending their ears to help me go through those difficult days.
- My awesome lab mates and friends in the Optics in Medicine lab, for truly making my experience at Dartmouth a wholesome one. I am grateful the program granted me a chance to establish lasting relationships with such wonderful people.
- And most importantly, I would like to express my deepest respect and gratitude towards my PI, Dr. Brian Pogue. From reading his papers in college to becoming a PhD student under his guidance, I am thankful to have received his training during my early career development. If research is a multivariable function, Dr. Pogue has shown and taught me the most important coefficients.

I would also like to acknowledge the unconditional support and love I have received from my family. My parents are one of the greatest gifts in my life. They are both engineers with a work ethic which I have always looked up to. I would also like to thank my sisters and my in-laws for their support and company, which were crucial to my graduate school experience. I am forever thankful for the on-time arrival of my daughter shortly after my defense. She has surprisingly given me the energy and spirit to complete my study throughout the last year at Dartmouth.

Finally, I am struggling to describe how grateful and fortunate I feel every day to have my husband's love and support during my journey at Dartmouth. Without Evan, I would not have made it. Thank you for believing in me more than I do myself.

Table of Contents

Abstract	ii
Acknowledgments	iv
Table of Contents	vi
List of Tables	x
List of Figures	xi
List of Acronyms	xx
Chapter 1: Introduction	1
1.1 Problem Statement.....	1
1.2 Overview of Research and Specific Aims	2
1.2.1 Overview of Research.....	2
1.2.2 Specific Aims.....	2
1.3 References	4
Chapter 2: Background	5
2.1 PDAC Drug Resistance Mechanisms	5
2.2 Physical Transport Barriers in the PDAC TME	6
2.2.1 Elevated Solid Stress.....	6
2.2.2 Elevated Interstitial Fluid Pressure	7
2.2.3 Intratumoral Heterogeneity	7
2.3 TME Measurement Techniques	8
2.3.1 Tissue Pressure Measurement Techniques	8
2.3.2 Vasculature Imaging to Characterize Transport	9
2.3.3 Stiffness as a New Biomarker to Reflect TME Changes	11
2.3.4 Stiffness Imaging Feasibility for Clinical Adoption	11
2.4 Overview of PDAC Treatment	12
2.4.1 Conventional PDAC Chemotherapy options and Evolving Targeted Therapies.....	12
2.4.2 Photodynamic Therapy and the Promise of Low-dose PDT	13
2.5 Tumor Heterogeneity Information in Clinical Translation.....	14
2.5.1 Radiomics as a Tool to Assess Heterogeneity from Clinical Image Data	14

2.5.2 Radiomics Analysis in the Context of PDAC.....	17
2.6 References.....	17
Chapter 3: Relationship of tumor vasculature and collagen content to verteporfin heterogeneity in PDAC tumors	24
3.1 Introduction.....	24
3.2 Materials and Methods.....	25
3.3 Results.....	29
3.4 Conclusion	32
3.5 Acknowledgments.....	33
3.6 References.....	33
Chapter 4: Relationship of tumor stiffness to tumor collagen and using stiffness as a surrogate for drug delivery assessment	35
4.1 Introduction.....	35
4.2 Materials and Methods.....	39
4.3 Results.....	45
4.4 Discussion.....	50
4.5 Conclusion	53
4.6 Acknowledgments.....	53
4.7 References.....	53
Chapter 5: Imaging tumor collagen from fresh tissue	57
5.1 Introduction.....	57
5.2 Materials and Methods.....	59
5.3 Results.....	67
5.4 Discussion.....	74
5.5 Conclusion	76
5.6 Acknowledgments.....	77
5.7 References.....	77
Chapter 6: Modifying PDAC tumor stroma with angiotensin II receptor blockers to improve verteporfin delivery	80
6.1 Introduction.....	80
6.2 Materials and Methods.....	81

6.3 Results.....	85
6.4 Conclusion	88
6.5 Acknowledgements.....	88
6.6 References.....	88
Chapter 7: Stiffness Heterogeneity as an Indicator of Drug Delivery Enhancement by Photodynamic Priming in PDAC	90
7.1 Introduction.....	90
7.2 Materials and Methods.....	92
7.3 Results.....	95
7.4 Discussion.....	99
7.5 Conclusion	102
7.6 Acknowledgments.....	102
7.7 References.....	103
Chapter 8: Radiomics Analysis on CT Scans of Patients Receiving PDT Treatment to Quantify PDP Effects	105
8.1 Introduction.....	105
8.2 Materials and Methods.....	107
8.3 Results.....	111
8.4 Discussion.....	118
8.5 Conclusion	120
8.6 Acknowledgments.....	121
8.7 References.....	121
Chapter 9: Conclusion	124
9.1 Overview.....	124
9.2 Conclusion for Aim 1.....	124
9.3 Conclusion for Aim 2.....	126
9.4 Conclusion for Aim 3.....	129
9.5 Conclusion for Aim 4.....	132
9.6 Final Remarks	134
9.7 References.....	135

Appendices	137
A.1 Pressure Data to Stiffness Map	137
A.2 Image Data Co-Registration	139
A.3 Color Segmentation on Pathology Images	140
A.4 Lectin Percentage Calculation from Pathology Images	141
A.5 Collagen Analysis to Obtain Structural Information	141

List of Tables

Table 8.1: Summary of patient characteristics	108
---	-----

List of Figures

- Figure 3.1:** All types of image data collected for this study as taken from pathology slices for Masson’s trichrome stain, and Lectin stain, while the Verteporfin fluorescence was taken from thick sections but at the same location28
- Figure 3.2:** The relationship of verteporfin uptake in pancreatic tumor to the collagen percentage and patent vessel area fraction. Each data point represented a whole tumor slice. Fluorescence signal were normalized with a blue foam material29
- Figure 3.3:** Examples of pancreatic tumor tissues with complexed distribution of collagen and vasculature. 3a-c (low collagen – high lectin – high drug uptake) and 3d-f (high collagen – low lectin – low drug uptake) were two of some regions displayed to not only highlight the heterogeneity within a tumor for all tissue parameters, but also to provide evidence for the potential of tissue microenvironment regional analysis.31
- Figure 4.1:** Tumor biomechanics and relevant biology information are actively studied at different spatial scales: sub-microscopic¹⁰, microscopic¹² and mesoscopic¹³. Current elastography tools offer either biologically relevant spatial resolution or clinically relevant field of view, none exists that could meet both requirements. Stiffness information as a clinical application to evaluate drug transport brings most benefit when whole tumor stiffness is assessed at inter-capillary distance spatial resolution36
- Figure 4.2:** Current experimental techniques for assessing features related to tumor stiffness. Common elastography assessment tools and their positions in the field include AFM: atomic force microscopy, MPM: multi-photon microscopy harmonic imaging, OCE: optical coherence elastography, UE: ultrasound elastography, MRE: magnetic resonance elastography. Ideal elastography imaging tools should be placed in the overlap between microscopic resolution region and whole-tissue FOV region. Since no current imaging tool could meet these requirements, ex vivo elastography (EVE) mapping was developed to study PDAC stiffness at relevant biological size scales, with 300-micron spatial resolution and a field of view that would cover a whole PDAC tumor.38

Figure 4.3: Ex vivo elastography (EVE) system and sample preparation. A) Overall system consists of an xyz- motorized table and a commercial fiber optic pressure sensor. B) Sample preparation procedure includes a tumor embedded in 10% gelatin. Metal pins are inserted to provide markers for image coregistration with pathology data. C) Pressure sensor operates based on Fabry-Perot interferometer technology. The cavity deformation due to external force is calibrated to give a corresponding pressure reading. D) Young’s modulus calibration curve between UE and EVE established by phantom measurements at different concentrations and temperatures. E) A simplified flow chart illustrates important steps of stiffness measurement, which includes tumor surface identification and 3-step compression testing.....40

Figure 4.4: Image data and tissue parameter identification process. A) Top row from left to right: fresh tumor surface in gel with inserted metal pins, BPD fluorescence, stiffness map. Bottom row: Masson’s Trichrome staining, lectin fluorescence, segmented collagen map from MT staining. All images are co-registered to MT staining data. B) Average stiffness detected from spleen (4.0 ± 0.3 kPa) and pancreas (2.3 ± 0.3 kPa). These regions are excluded from tumor analysis by manual ROI drawn on pathology data.....44

Figure 4.5: Comparison between UE and EVE stiffness map. A) Elastography imaging data from both systems are displayed to highlight similar pattern of stiffness heterogeneity. B) Stiffness map obtained from EVE system with better spatial resolution allows for direct comparison between stiffness and collagen pattern in the tumor. C) Expanded images of different ROIs highlight the correlation between stiffness and collagen percentage in PDAC tumors46

Figure 4.6: Stiffness and collagen content in PDAC tumors are highly correlated both globally and regionally. A) Visualization of stiffness, collagen and the overlay between two parameters show a good correlation in both AsPC-1 and BxPC-3 tumor lines. B) AsPC-1 tumors contain 9.6 ± 2.7 percent collagen and average stiffness of 32 ± 11 kPa. As for BxPC-3, collagen percentage is averaged at 13 ± 3 percent and stiffness measured at 46 ± 24 kPa. Both of these quantities are statistically significant between AsPC-1 and BxPC-3 tumors. C) Regional analysis to examine high stiffness and low stiffness regions

demonstrates a linear correlation between Young’s modulus and collagen profile with $R^2 = 0.59$. For each tumor, two high-stiffness and two low-stiffness regions were chosen (AsPC-1: n = 13, ROIs = 52; BxPC-3: n = 14, ROIs = 56)47

Figure 4.7: PDAC tumor stiffness is inversely correlated with drug uptake and patent vessel data. A) Whole-tumor visualization of BPD fluorescence distribution and stiffness heterogeneity obtained from EVE. B) Close-up regions of low and high drug uptake reveal the inverse relationship with stiffness and collagen distribution. C) Tumor YM is inversely correlated to BPD distribution in AsPC-1 and BxPC-3, with higher uptake in AsPC-1 tumors. D) Tumor YM limits patent vessels which explains the limited drug penetration. For each tumor, two high-stiffness and two low-stiffness regions were chosen. There were 3 ROIs omitted since the vessel density percentage was essentially zero, and those ROIs had stiffness values greater than 100 kPa. (AsPC-1: n = 7, ROIs = 27; BxPC-3: n = 7, ROIs = 26)49

Figure 5.1: UV-fluorescence imaging system setup. A) A schematic of the imaging system with camera tube lens and either 7.5X or 10X objective lens. Illumination sources were 2 UV-LEDs mounted symmetrically. B) The imaging field of view and spatial resolution test are shown. C) The illumination spot size generated by the UV-LEDs is shown with irradiance 10 mW/mm². D) Emission spectra of UV-excited staining dyes when illuminated at 275-nm covered the detection range of the RGB camera59

Figure 5.2: Schematic of primary image processing steps. A) At each location, an image stack was acquired by moving tissue samples on a motorized translation stage. High-pass filtering was applied to reduce out of focus information. Depth of field correction was then applied. Scale bar = 100 μm. B) Nuclei and collagen were identified by color segmentation in HSV space. Fiber analysis was done on segmented collagen to yield information such as fiber length, thickness, orientation and crosslinking profile. UV-fluorescence images were also color-map transferred to mimic the color palette of Masson’s Trichrome staining (blue collagen, dark purple nuclei and light pink cytoplasm). The color remapping process was executed in L*a*b space, utilizing the mean and standard deviation of each channel to create a color scaling factor. C) Image stitching was performed with 10% overlap to create

a whole-tumor view. Rigid image co-registration was performed on the whole-tumor size UV-fluor images, histology images and brightfield photos of freshly resected tumors to facilitate comparison across imaging modalities. Scale bar = 2 mm62

Figure 5.3: Demonstration of collagen segmentation and quantification methods for UV-fluor data with validation testing on Trichrome data, summarized in 3 main steps. A) Step 1 generated collagen thickness maps using the matlab function `bwdist.m` performed on segmented collagen in HSV space. B) Step 2 resulted in skeletonized maps of collagen in combination with thickness maps. Necessary refinements on UV-fluor data were highlighted. A thresholding value was applied on the UV-fluor collagen thickness map to eliminate inaccurate connections of clusters and small cross-sections of collagen due to tissue cut orientation. Skeletonization using `bwskel.m` and cluster breakdown using `bwconncomp.m` yielded individual collagen strands. C) Fiber analysis in Step 3 was performed on each collagen strand to measure the length, thickness and orientation. Statistical analysis to compare fiber analysis between UV-fluor and Trichrome data was conducted to validate the feasibility of using UV-fluor imaging data to obtain quantified collagen information65

Figure 5.4: UV-fluorescence imaging is capable of capturing stromal content in PDAC tumors. A) Deep UV-illumination below 300 nm provides excellent image contrast, revealing morphology at the microscopic level. Collagen content from peritumoral and intratumoral regions are illustrated, scale bar = 100 μm . B) Optical sectioning and depth of field correction provides semi-3D depth information, which highlights 3D structures such as vessel, collagen crosslinking and bundling. C) Rapid imaging allows tumor visualization at macroscopic level, scale bar = 2 mm. D) Demonstration of strong yellow-green collagen signal was obtained from an RGB camera of fresh tissue imaging, and this is compared to Masson's Trichrome staining data68

Figure 5.5: Color remapping of UV-fluorescence images allows visualization using Masson's Trichrome staining color scheme. A) UV fluorescence image after color remapping showed collagen in blue and nuclei in dark purple, similar to Masson's Trichrome staining results, scale bar = 30 μm . B) Illustration of color remapping in L^*a^*b color space, based on structural segmentation. Corresponding histograms of reference,

input and output images show that the distribution of color intensities and hues was preserved.69

Figure 5.6: Quantification of collagen content in PDAC tumors. A) Different types of collagen observed in both Trichrome and UV-fluorescence data sets. B) Quantification of collagen fibers. C) Distribution of fiber length, fiber thickness and fiber orientation obtained from both data sets D) Statistical analysis was performed to show that there is no significant difference in means in terms of tumor collagen content, fiber length and fiber orientation between UV-fluorescence and Trichrome data. However, there was a statistical difference between two data sets for fiber thickness. Mean and standard deviation of UV vs. Trichrome data, respectively, for each category are 18.8 ± 4.2 vs. 15.6 ± 8.1 (collagen content %), 15.9 ± 7.8 vs. 7.9 ± 7.3 (collagen thickness in μm), 48.5 ± 36 vs. 49.3 ± 47 (collagen fiber length in μm), 2.53 ± 51 vs. -0.85 ± 51.3 (collagen fiber orientation in degrees). Data was analyzed for 5 tumors, necrosis areas were excluded, 50 ROIs were randomly selected with ROI size of 0.6×0.4 mm each, total collagen strands from UV data = 6442, from Trichrome data = 6606.....71

Figure 5.7: UV-fluorescence imaging as a fresh tissue assay platform to evaluate photodynamic priming responses. A) Perfusion imaging of dextran tagged with Texas Red in kidney samples. UV-excited Texas Red shows perfused dextran in kidney samples (middle) as compared to endogenous fluorescence without any dextran injection (left). Dextran-perfused tissues could then undergo pathological staining (right) to obtain structural information, scale bar = $500 \mu\text{m}$. B) Tissue imaging surface was outline in yellow. Necrosis outlined in red is hard to distinguish in brightfield image (left), but observable under UV-fluorescence imaging (middle) which is confirmed by trichome staining (right), scale bar = 1 mm . C) A comparison of collagen content in control and PDP treated tumors. Collagen modulation effect was observed, in which the PDP treated tumors show a 13% reduction in collagen content ($n = 2$ animals per group, control ROIs = 23, treated ROIs = 19), scale bar = $100 \mu\text{m}$ 73

Figure 6.1: Tumor image data (A) Fresh tumor tissue was embedded in 10% gelatin with metal pins inserted to provide common points for image coregistration. (B) H&E staining of the corresponding tumor section provided markers for tissue identification (more details

explained in section 2.7). (C) Masson’s Trichrome staining highlighted collagen fibers in blue from which a systemic segmentation was performed to extract collagen content of tumor tissue. (D) Stiffness map of tumor tissue was coregistered to pathology data to assess regional stiffness of the tumor83

Figure 6.2: Tissue identification from H&E staining was a first crucial step in assessing tumor biological parameters from pathology data. (A) On the left tissue, green arrows indicated normal pancreas tissue which was stained dark purple. On the right tissue, the red arrow showed the necrosis area which should be excluded from tumor analysis since this area mostly contained dead cells. The yellow arrow pointed out the spleen tissue which was often attached to the resected tumor in mouse models. Spleen tissue was also excluded before implementing any tumor analysis. (B) The two images on this second row represented the tissue samples after eliminating non-tumor artifacts such as pancreas tissue, spleen tissue and tumor necrosis84

Figure 6.3: Normalized verteporfin uptake in control and treated AsPC-1 bearing mice (n = 3 per group). Error bars indicate one standard deviation. Preliminary data showed photosensitizer uptake enhancement in treated mice85

Figure 6.4: Collagen structure modification in treated mice was observed. (A) In the control group, collagen structure appeared to be made of thick bundles which included randomly oriented strands. (B) In the treated group, collagen structure was comprised of singular strands organized into thinner bundles.....86

Figure 7.1: PDAC Tumor Microenvironment Modulation Effects from Photodynamic Priming Treatment A) Tumor size measured after resection showed no statistical difference between the control and the treated group ($p = 0.65$), implying that tumors were harvested at the same growing stage which eliminated potential for collagen proliferation variations due to different tumor progression time. B) There was a statistical difference in necrotic areas after PDT, as identified from H&E staining between the groups ($p = 0.018$). The control group had inherent necrosis due to the nature of tumor progression and the treated group resulted in 2-fold of necrosis, confirming successful PDT treatment. C) Normalized dextran fluorescence intensity was used to evaluate drug uptake. There was a 22% increase in drug uptake from the treated group ($p = 0.011$). D) Lectin fluorescence was quantified

to show that vascular patent area increases by 28% in the treated tumors ($p = 0.073$). E) Collagen content percentage calculated from Masson's Trichrome staining showed a 30% decrease as a result of PDT treatment ($p = 0.001$). F) Average tumor stiffness was decreased by 21% as compared to the control group ($p = 0.008$). Control group $n = 5$, treated group $n = 7$ (Figure A-E) and $n = 6$ (Figure 1F).96

Figure 7.2: PDP relieves overall stiffness and collagen density which allowed more dextran delivery in treated tumors A) A panel of tumors divided into three categories is presented (control = 5 tumors, responding = 6 tumors, outlier = 1 tumors). Visualization of collagen distribution as blue staining from Trichrome data is displayed in the first column. Necrosis areas are identified by the red dotted line to confirm that treatment was given. The middle column shows stiffness heterogeneity with values ranging from 0 to 150 kPa. The last column highlights dextran fluorescence as tumor drug distribution. B) For all the tumors in this study ($n = 12$), dextran uptake and vascular patency are strongly correlated ($R^2 = 0.79$). Average stiffness is inversely correlated to drug uptake ($R^2 = 0.71$) but is correlated to tumor collagen content ($R^2 = 0.58$). The linear regression generated with stiffness data in the last two plots excluded the outlier tumor (blue dot) due to its unusually high stiffness value.....97

Figure 7.3: Texture Analysis of Tumor Stiffness Shows Homogeneity as an Indicator of Treatment Response A) Results of GLCM texture analysis on tumor stiffness data is demonstrated. Homogeneity and Energy (or Uniformity) of stiffness values are found to be increased after PDT treatment ($p = 0.013$ and $p = 0.017$, respectively), while GLCM contrast or variation is decreased after treatment ($p = 0.046$). B-C) GLCM Homogeneity is correlated with dextran uptake in both control and treated tumors ($R^2 = 0.62$) and is inversely correlated with collagen content ($R^2 = 0.67$), indicating that this texture feature could be used to predict treatment outcome. D) Visualization of stiffness homogeneity in control and treated tumors with their corresponding GLCM Homogeneity scores.....98

Figure 8.1: Overview of texture analysis in assessment of photodynamic therapy treatment on PDAC patients. Each patient received a pre-treatment and a post-treatment CT scan.

Pancreatic tumor segmentation was performed, and texture analysis was carried out to extract underlying features that showed significant differences after the treatment.....106

Figure 8.2: Overview of PDT-induced changes observed between pre- and post-treatment CT scans. A) Tumor size measured from 3D segmentation of tumors shows no significant change (paired t-test, p-value = 0.36). B) All patients show a reduction in mean tumor CT number, indicating the tumor density has decreased after PDT treatment (paired t-test, p-value = 0.01). C) 6 out of 7 patients show a reduction in standard deviation of tumor CT number, suggesting that the intratumor variation has decreased after treatment (paired t-test, p-value = 0.04). D) Range of CT number is decreased for 5 out of 7 patients which indicates the reduction of intratumor variation after PD (paired t-test, p-value = 0.47)112

Figure 8.3: Treatment-induced necrosis areas could be predicted by texture analysis in the Pre-Tx scan. A) Visualization of tumor in Post-Tx (top row) and Pre-Tx (bottom row) CT scans. Observable necrosis area (PDT) in pink and remaining tumor region (PDP) in yellow are delineated in Post-Tx scans, which were then mapped onto Pre-Tx scans for texture analysis. GLCM Contrast feature for both regions in the Pre-Tx scans is illustrated to show that necrosis occurred at the area with lower contrast. B) Other first-order texture features that are found to be statistically significant when comparing the PDT and the PDP regions in Pre-Tx scans (n = 40 tumor slices).....113

Figure 8.4: Percentage of changes after light treatment between pre-treatment and post-treatment scans in the PDP regions of tumors, as compared to the normal liver and spleen values. For each patient, the percentage change in CT mean was reported for the non-necrotic regions of PDAC tumor, liver and spleen. Mean CT number decreased in all ROIs from all patients, with the tumor regions consistently expressing the biggest reduction in CT number. This observation suggested that there were treatment-induced effects on the tumor CT numbers across the patient cohort114

Figure 8.5: Figure 8. 5 PDP effects after light treatment are seen with texture analysis. A) A visualization of intratumor changes due to light treatment quantified by GLCM texture analysis. Means of tumor CT number before and after treatment are 74 ± 23 HU and 67 ± 17 HU, respectively. Tumor homogeneity is increased, while levels of contrast and

dissimilarity are decreased, indicating a more uniform tumor attenuation profile. B) Texture features that showed a statistical significance between Pre-Tx and Post-Tx scans are reported (n = 235 tumor slices)116

Figure 8.6: Classification for each feature and a combined classifier by SVM model A) Mean ROC curve for each reported feature calculated for all patients except for Patient 01, showing AUC values in the range of 0.75 to 0.80. B) Mean ROC curve of combined classifiers using SVM model in blue yielded a better performance than any single classifier (AUC value is 0.93 ± 0.07). Leave-one-patient-out cross validation ROC curves are showed for all patients except Patient 01, and the shaded area indicated the ± 1 standard deviation of this cross validation.....117

List of Acronyms

Acronym	Definition
AFM	Atomic Force Microscopy
AUC	Area Under the ROC Curve
BPD	Benzoporphyrin Derivative
CMOS	Complementary Metal Oxide Semiconductor
CT	Computed Tomography
ECM	Extracellular matrix
EOS	Electro-Optical System
EVE	Ex vivo elastography
FOV	Field of View
FRAP	Fluorescence Recovery After Photobleaching
GLCM	Gray-Level Co-Occurrence Matrix
GLNU	Gray-level Non-Uniformity
GLRLM	Gray-Level Run-Length Matrix
H&E	Hematoxylin and Eosin
HA	Hyaluronan Acid
HSV	Hue-Saturation-Value
HU	Hounsfield Units
IFP	Interstitial Fluid Pressure
LED	Light-emitting Diode
MPM	Multi-photon Microscopy
MRE	Magnetic Resonance Elastography
MT	Masson's Trichrome
NGLDM	Neighborhood Gray-Level Different Matrix
OCE	Optical Coherence Elastography
PaSC	Pancreatic stellate cell
PDAC	Pancreatic ductal adenocarcinoma
PDP	Photodynamic priming

PDT	Photodynamic therapy
RBF-SVM	Radial Basis Function - Support Vector Machine
ROC	Receiver Operating Characteristic
ROI	Region of Interest
SS	Solid Stress
TME	Tumor microenvironment
Tx	Treatment
UE	Ultrasound Elastography
UV	Ultraviolet
YM	Young's Modulus

Chapter 1: Introduction

1.1 Problem Statement

Pancreatic ductal adenocarcinoma (PDAC) accounts for 90% of pancreatic cancer,¹ which has risen to be the fourth leading cause of cancer-related death.² As the 5-year survival rate of all stages combined remains below 5% for the past decades due to late prognosis and poor resectability,³ research have identified PDAC as one of the most aggressive due to its drug-resistance biological hallmark.^{4,5} While the complexity of genetic modifications has been rigorously studied in the search for a predictive biomarker, more recent attentions turn towards the heterogeneity of the characteristic desmoplasia in the tumor microenvironment (TME) as another major cause of drug resistance. It has been reported that the TME does not only promote the compensatory molecular signaling pathways responsible for progression, but multiple TME factors are also recognized as physical drug transport barriers.^{6,7} More understanding of the PDAC biology and pathophysiology related to drug resistance has been widely established, yet clinical translation remains a challenge due to the lack of feasible methods to collect meaningful predictive information at the microscopic or sub-cellular levels.

Consistent with the growing focus on the role of PDAC TME in tumor progression and drug resistance is the considerable efforts towards developing novel therapies. Combination treatment of a targeted regimen in conjunction with a more conventional therapeutic course appears to be the most promising approach. However, mixed results from clinical trials^{8,9} continue to stress on the unsolved problem of systemic and intratumoral transport efficiency, further underscoring the need to clinically characterize a

predictive measure of the highly compensatory signaling pathways and the extreme heterogeneous TME. Preclinical research findings and observations from such clinical trial outcomes have urgently called for a reliable and translatable marker of tumor drug transport efficiency.

1.2 Overview of Research/ Specific Aims

1.2.1 Overview of Research

This research work mainly focuses on further understanding the role of the PDAC TME and exploring the use of photodynamic therapy (PDT) to modulate the TME with the ultimate goal of improving the tumor drug uptake. Realizing the characteristic heterogeneity as a major cause of drug resistance and the need for a relevant clinically translatable biomarker, the work specifically examines tumor stiffness heterogeneity imaging as such a potential indicator. Tumor stiffness heterogeneity and its relationship to the TME as well as intratumoral transport is studied with the purpose of employing predictive information in the evaluation of treatment responses, and in the context of potentiating elastography imaging in clinical PDAC treatment.

1.2.2 Specific Aims

While each following chapter is delegated to present a study whose main objective is aligned with the thesis central theme of imaging the PDAC TME heterogeneity and studying its role in intratumoral drug distribution, there are four primary Aims summarized below with relevant Chapters. These Aims have been established to specify the necessary tasks, consolidate the deliverables and are also used to organize the conclusion remarks in **Chapter 8** which reevaluates the goals and the accomplished work from a macroscopic

view, discusses the limitations and suggests future directions.

Aim 1: Image wide-field tumor stiffness heterogeneity at transport-relevant resolution to investigate the relationship between tumor stiffening, desmoplasia and drug transport

Chapter 2 provides insights on the motivation of Aim 1 to examine tumor heterogeneity, leading to the study in **Chapter 3** where an ex vivo stiffness mapping system was built to address Aim 1 objective.

Aim 2: Visualize and quantify PDAC tumor collagen network from fresh samples using fluorescence imaging with ultraviolet illumination

The development of the fluorescence imaging system to image collagen from fresh tissue samples and data quantification is fully discussed in **Chapter 4**.

Aim 3: Evaluate collagen and stiffness modulation effects by photodynamic therapy treatment to enhance intratumoral drug uptake

An attempt to modify the tumor stroma with angiotensin II receptor blocker is discussed in **Chapter 5**. **Chapter 6** provides a more comprehensive study with conclusive results on the goal of TME modulation to enhance drug uptake using photodynamic therapy.

Aim 4: Quantify photodynamic priming effects using radiomics analysis on clinical PDAC CT scans

As results from the previous Aims underscore the role of tumor heterogeneity, **Chapter 7** involves a study to examine the heterogeneity effects in PDT-treated PDAC patients using texture analysis on the CT scans before and after treatment.

1.3 References

1. Orth, M. *et al.* Pancreatic ductal adenocarcinoma: Biological hallmarks, current status, and future perspectives of combined modality treatment approaches. *Radiation Oncology* **14**, 1–20 (2019).
2. Pancreatic Cancer: Statistics | Cancer.Net. Available at: <https://www.cancer.net/cancer-types/pancreatic-cancer/statistics>. (Accessed: 12th March 2021)
3. Bengtsson, A., Andersson, R. & Ansari, D. The actual 5-year survivors of pancreatic ductal adenocarcinoma based on real-world data. *Sci. Rep.* **10**, 16425 (2020).
4. Quiñonero, F. *et al.* The challenge of drug resistance in pancreatic ductal adenocarcinoma: a current overview. *Cancer Biology and Medicine* **16**, 688–699 (2019).
5. Grasso, C., Jansen, G. & Giovannetti, E. Drug resistance in pancreatic cancer: Impact of altered energy metabolism. *Critical Reviews in Oncology/Hematology* **114**, 139–152 (2017).
6. Feig, C. *et al.* The pancreas cancer microenvironment. *Clin. Cancer Res.* **18**, 4266–76 (2012).
7. Chauhan, V. P., Stylianopoulos, T., Boucher, Y. & Jain, R. K. Delivery of Molecular and Nanoscale Medicine to Tumors: Transport Barriers and Strategies. *Annu. Rev. Chem. Biomol. Eng.* **2**, 281–298 (2011).
8. Van Mackelenbergh, M. G. *et al.* Clinical trials targeting the stroma in pancreatic cancer: A systematic review and meta-analysis. *Cancers* **11**, (2019).
9. Bijlsma, M. F. & van Laarhoven, H. W. M. The conflicting roles of tumor stroma in pancreatic cancer and their contribution to the failure of clinical trials: a systematic review and critical appraisal. *Cancer Metastasis Rev.* **34**, 97–114 (2015).

Chapter 2: Background

2.1 PDAC Drug Resistance Mechanisms

Despite the poor resectability due to involvement of major blood vessels surrounding the pancreas, drug resistance contributes significantly to the high mortality rate of PDAC. The nature of PDAC drug resistance is driven by two main mechanisms: the heterogeneity of genetic mutations and the desmoplastic TME. More than 165 genes have been found to be responsible for such molecular complexity, which results in the regulation of signaling pathways and overexpression of proteins associated with progression, invasion and metastasis.¹ The ability to mediate different mechanisms allows PDAC tumors to rapidly develop resistance via compensatory pathways, which poses a big challenge to targeted therapies. Besides the complex genetic behaviors, the TME with characteristic desmoplasia have gained increasing attention since it is involved in cellular signaling as well as creating physical barriers to drug resistance. The TME provides structural support to different cell types along with the cancer cells, making it a hub for the development of cellular crosstalk that promotes invasion and metastasis.²⁻⁴ Furthermore, the dense stroma and abnormal vasculature form physical barriers that inhibit intratumoral transport with elevated total tissue pressure.^{5,6} Whether originated from genetic signaling pathways or physical barriers existed in the TME, PDAC drug resistance highlights extreme heterogeneity observed from macroscopic to microscopic levels. The heterogeneity of the TME components responsible for physical transport barriers will be examined in the scope of this thesis work.

2.2 Physical Transport Barriers in the PDAC Tumor Microenvironment

It is widely accepted that the activated pancreatic stellate cells (PaSC) are responsible for the physical abnormalities occurring in the PDAC TME, often described as desmoplastic.⁷⁻¹⁰ In this section, these TME components are discussed in the context of their contributions to create physical transport barriers, and the nature of elevated total tissue pressure.^{6,11,12} The relevant relationships between tumor biology and tumor biomechanics are introduced. Specifically, three inhibiting phenomena are discussed: 1) Elevated solid stress due to the overproduction of TME macromolecules, 2) Elevated fluid pressure due to collapsing vessels and the lymphatic systems and 3) Extreme intratumoral heterogeneity further exacerbating these transport problems.

2.2.1 Elevated solid stress by macromolecule accumulation

Cancer-associated fibroblasts (CAFs) are believed to be responsible for the overproduction of macromolecules in the extracellular matrix during tumor progression¹³, which results in the accumulation of proteins such as collagens of different types and hyaluronans (HA). In the limited space, the overaccumulation of collagens creates a solid stress (SS) that exerts physical force upon nearby TME components. Compressed blood and lymphatic vessels lead to slow perfusion which directly affects tumor transport.^{5,14} Furthermore, evidence has shown that the decreased blood flow due to high SS causes hypoxia, another significant and very well-studied phenomenon responsible for promoting tumor progression, inflammation, and invasion, all of which contribute to lower therapeutic efficacy.¹⁵ While growth-induced SS is partially attributed to cancer cell proliferation, the major contribution of the ECM components, mostly collagen, is well-established.¹⁶⁻¹⁸

2.2.2 Elevated interstitial fluid pressure by the abnormal vasculature and lymphatic system

As the blood and lymphatic vessels are mechanically deformed due to SS, their dysfunction leads to fluid accumulation within the tumor which consequently results in elevated interstitial fluid pressure (IFP). While vessels are physically collapsed by the high SS, several other factors contribute to the vascular abnormalities of the PDAC TME. Angiogenesis, or the increasing growth and density of the microvasculature, is another hallmark of the TME. Several cancer metabolism pathways¹⁹ are responsible for the overgrowing of immature, tortuous and leaky micro-vessels as the tumor adapts and compensates for the hypovascularity due to desmoplasia. These abnormal vessels are tortuous which slows down the blood flow, and their leakiness causes fluid loss which increases viscosity.⁵ All of these changes in the vasculature significantly contribute to lower the tumor transport efficiency. Meanwhile, the dysfunctional lymphatic system results in no tumor drainage.²⁰ As fluid accumulates in the tumor space, elevated IFP is observed. The increased IFP can flatten the pressure gradient thus limits convective interstitial transport. The combination of abnormal vasculature and lymphatic system regulates the IFP and thus directly affects intratumoral drug transport.^{11,21,22}

2.2.3 Heterogeneity further exacerbates intratumoral distribution

Elevated SS and IFP, due to the desmoplastic TME, is further exacerbated by the inherent intratumoral heterogeneity. The heterogeneity of the PaSCs primarily responsible for the characteristic desmoplasia is observed within and across different tumor phenotypes.⁷ Studies have recognized that heterogeneity is correlated to tumor aggressiveness.^{23,24} Fundamental TME components that display extreme heterogeneity are

reported such as the PaSCs and CAFs, which creates a cascade of heterogeneity of different degrees to subsequent by-products such as the collagen content, blood vessels and immune cells, all of which directly affect intratumoral transport.

2.3 TME Measurement Techniques

This section discusses different measurement techniques developed to examine the TME components affecting tumor transport.

2.3.1 Tissue pressure measurement techniques

Interstitial fluid pressure measurement techniques

Recognizing the elevated tissue pressure as a byproduct of the underlying molecular changes in the TME, some research has focused on developing techniques to validate this relationship between the tumor biology and the tumor biomechanics. One of the earliest methods to characterize the interstitial fluid pressure was based on the “wick-in-needle” concept.^{25,26} Introduced by Fadnes et al., the wick-in-needle technique was designed to have a side-hole near the needle tip which was filled with nylon fibers. After the needle was inserted into the measuring sample and the pressure from insertion was stabilized, the fluid pressure was determined by the compression or decompression of the fibers, which was recorded by a pressure transducer and an amplifier.²⁵ More recent developments utilized a miniature pressure transducer that could be placed directly into the needle hole.^{27,28} While there has been debate over the comparative value of these, the operating mechanism has remained the same, i.e., a point-probe based mechanism.

Solid stress measurement techniques

SS measurement techniques are limited and a few approaches to determine this parameter requires tissue excision. Proposed by Stylianopoulos et al., SS measurements are often conducted by estimating the amount of tissue deformation from being cut.^{15,29} A recent improvement of the technique was introduced by Nia et al., in which the excised tissue deformation was imaged using high resolution ultrasound, giving SS measurements in a 2-dimensional map.²⁹ As an attempt to measure both SS and IFP, Nieskoski et al. proposed an improved technique using a piezoelectric pressure transducer inserted into a needle, which operated in a similar manner to the aforementioned wick-in-needle technique.³⁰ While there has yet to be a gold-standard technique to characterize SS, IFP and the total tissue pressure, studies have a strong agreement on the considerable degree of heterogeneity observed in these measurements and its connection to the heterogeneous components of the TME such as collagen, hyaluronan and blood vessels.

2.3.2. Vasculature imaging to characterize transport

Vascular transport measurement techniques

Drug transport in tumors could be classified into three different steps: vascular transport, transvascular transport and interstitial transport.⁵ Vascular transport describes the convective-diffusive delivery from the blood vessels into the tumor regions and is determined by perfusion rate q .

$$\text{Perfusion Rate } q = \frac{Q}{V} = \frac{\text{Volumetric Flow Rate}}{\text{Tissue Volume}}$$

The flow rate, drug concentration and tissue volume can all be measured in real time with fluorescence-based imaging techniques such as intravital imaging³¹ or multiphoton microscopy.³² Single vessel blood flow is made possible with multiphoton

laser scanning microscopy in which flow velocity can be determined by the frequency of line scanning along the vessel centerline.³³ Red blood cell velocity calculation to characterize different flow rates between a normal and a leaky vessel could also be performed by tracking the fluorescence beads with fluorescence imaging.³⁴ Vascular leakiness measurements also make use of fluorophore-tagged liposomes of different sizes. These liposomes are injected into the animal and microvascular extravasation is imaged using intravital imaging.

Interstitial transport measurement techniques

Interstitial transport or the delivery of small drug particles within the tissue space is defined mostly by diffusion, or the change in concentration with respect to time:

$$\text{Diffusion rate} = \frac{\delta C_i}{\delta t} = D \nabla^2 C_i$$

in which $\nabla^2 C_i$ represents the Laplacian of interstitial concentration and D is the diffusion coefficient. Similarly, imaging methods to calculate the diffusion rate are based on multiphoton microscopy with fluorescence imaging. One common technique is fluorescence recovery after photobleaching (FRAP) in which the spatial distribution of fluorophores is analyzed before and after photobleaching to estimate the diffusion coefficient.³⁵

Besides these in vivo fluorescence imaging methods, pathology staining provides a simple and effective way to determine function blood vessels by intravenously injecting a vascular marker such as lectin or dextran and analyzing images of thin tissue sections afterwards. While information from these thin sections does not capture the whole-tumor

vasculature profile, it is an efficient method to gain insights with whole-sample size field of view and microscopic resolution.

2.3.3 Stiffness as a new biomarker to reflect TME changes related to drug transport

Research interests focusing on understanding the PDAC complexity in either tuning genetic modifications or building a desmoplastic TME have had similar findings to link stromal stiffening as a physical properties regulating tumor aggressiveness.³⁶ Laklai et al. provided the first evidence to link tumor stiffness to both PDAC genotypes and desmoplasia.³⁷ As tumor collagen content is identified as a significant component to the elevated solid stress that affects drug transport,³⁸ the relationship between collagen deposition, alignment and crosslinking to tumor stiffness has also been demonstrated by multiple studies.³⁹⁻⁴² These findings strongly suggest that further investigation of tumor stiffness could be a promising indicator of biological changes related to PDAC drug transport.

2.3.4 Stiffness imaging feasibility for clinical adoption

Stiffness imaging methods are developed primarily based on the concept of measuring stress at different levels of strains (or indentations) to estimate the Young's modulus, or the stiffness of material.

$$\text{Young's modulus } E = \frac{\sigma}{\varepsilon} = \frac{\text{stress}}{\text{strain}}$$

While strong evidence supports the relationship between tumor stiffening and the underlying biological changes related tumor progression, tumor stiffness information has been mostly acquired at the microscopic level. Conventional elastography imaging

modalities can determine stiffness values down to micron resolution with atomic force microscopy (AFM) or multi-photon microscopy (MPM), but the sample size is limited to smaller than 100 μm . Optical coherence elastography (OCE) can offer microscopic resolution with a field of view up to hundreds of microns or even larger when coupled with a translational stage, but the technique is costly and complicated. Considering the diffusion distance of nanoparticles from the blood vessels is 100 μm at maximum,⁴³ elastography data reflecting transport profile should be capable of whole-sample imaging (a few cms) at resolution of at least a hundred microns. No such elastography imaging system is currently available, especially for the purpose of studying tumor stiffness with respect to intratumoral drug transport. However, moving towards this direction with promising developments to fulfill such imaging requirements are advances in ultrasound and magnetic resonance elastography. Ultrasound and MRI are conventional imaging modalities widely used in clinical assessment, and with current elastographic resolution of 1-mm, it is promising that near future clinical applications of these techniques will be realized in PDAC treatments as tumor stiffness heterogeneity becomes a reliable and practical indicator of transport.

2.4 Overview of PDAC Treatment

2.4.1 Conventional PDAC chemotherapy options and evolving targeted therapies

For unresectable PDAC patients, chemotherapy remains the next best option. Gemcitabine alone⁴⁴ or more recently, in combination with other agents such as nab-paclitaxel⁴⁵ or erlotinib⁴⁶ have yielded positive clinical outcomes. FOLFIRINOX, a combination of four drugs, has been reported to have even better efficacy when compared to gemcitabine and the efficacy has been confirmed in multiple clinical trials.^{47,48} However,

the significant toxicity remains the limiting problem^{49,50} and there has yet to be a reliable biomarker to predict patient responses to these therapeutic regimens. While more combinations of chemo agents are being tested, molecular-targeted therapies have emerged as a new line of therapeutic options due to promising preclinical findings, one of these focus targets is the tumor stroma.⁵¹ Anti-stromal therapies attempting to improve the PDAC TME have approached this key element of tumor progression by targeting the angiogenesis or the fibroblasts via systemic delivery of drugs that inhibit growth factors.⁵²⁻⁵⁵ However, these approaches did not yield any improvements in survival as compared to established chemo regimens, and recent studies have speculated that PDAC physical transport barriers such as hypovascularity and desmoplasia might be the explanation.⁵⁶ Therefore, it is necessary to identify an effective method to tackle the problem of drug delivery efficiency, i.e., a focal treatment course that does not fully rely on systemic delivery such as photodynamic therapy proposed in this thesis work.

2.4.2 PDT in PDAC treatment and the promise of low-dose PDT

Photodynamic therapy (PDT) is an FDA-approved treatment course in several types of cancers. The treatment efficacy is determined by the combination of three main factors: the photosensitizer uptake, the light fluence and the concentration of singlet oxygen.⁵⁷ A photosensitizer is topically or systemically administered but photodamage only occurs at the regions where light is introduced to produce singlet oxygen, which results in tumor cell death. As a localized therapy using low-toxicity photosensitizer, PDT has been employed in combination with almost every conventional therapeutic regimens either before or after without compromising their efficacy.⁵⁸ The ability to delivery light via a fiber optic has broaden the range of possible PDT applications, with recent studies investigating PDT as

part of combination treatment to improve PDAC outcome. PDT has been exploited due to its ability to target different components of the TME depending on the drug-light interval and is speculated to enhance subsequent drug delivery by producing transient vascular permeability.^{59,60}

While the concept of low-dose PDT has previously been introduced by Snyder et al.,⁶¹ preclinical findings recently have provided new insights on the feasibility of such approach to prepare the tumor for subsequent treatments. Evidence have showed that a sub-lethal dose of PDT not only enhances vascular permeability⁶² but also displays promising results with collagen depletion,⁶³ both of which could effectively target the prominent physical transport barriers of PDAC tumors. Furthermore, Huang et al. has reported the synergistic benefits of low-dose PDT in combination with irinotecan to target compensatory signaling pathways and minimize systemic toxicity.⁶⁴ As more preclinical evidence elucidates the mechanisms in which PDT modulates the TME,^{65,66} it is a reasonable approach to evaluate the benefits of low-dose PDT in targeting PDAC physical transport barriers as well as the corresponding tumor biomechanical changes.

2.5. Tumor heterogeneity information in clinical translation

2.5.1 Radiomics as a tool to assess heterogeneity from clinical image data

Overview of Radiomics Analysis Concepts

As tumor heterogeneity within and across phenotypes becomes a significant factor in disease prognosis and more evidence suggests its relationship to treatment outcome, more methods are developed to characterize heterogeneity with a strong emphasis on the feasibility of clinical translation. The field of radiomics has emerged as a result of this new

research direction. Radiomics is defined as analysis performed on image data to extract information that cannot be appreciated by the naked eye. Algorithms have been developed to characterize image texture features of a region of interest (ROI). Radiomics data includes both basic, first-order morphological information such as an ROI's size and shape, intensity histogram and relevant histogram-based parameters including skewness or kurtosis. Deeper data exploitation is often referred to as second-order analysis, which involves computations of spatially defined texture parameters such as contrast, variance, homogeneity and heterogeneity properties in multiple directions (on the x-y-z axes) and dimensions (2D vs. 3D), and with respect to a certain volume of neighboring pixels or voxels. Currently, radiomics analysis tools are applicable to a wide range of imaging data including CT, PET, MR and ultrasound, and they have become more ubiquitous with options for both open-source programming^{67,68} as well as free software packages.^{69,70}

Considerations Regarding the Interpretations of Radiomics Results

The use of radiomics in medical imaging data has burgeoned due to its functionality in addition to the availability of existing data. Texture features are extracted from clinical scans and their correlations to certain medical conditions and biological factors are evaluated. Classification algorithms and modeling are often employed in such assessments to determine the clinical value of identified features. Since the process is mainly computational and conclusions are drawn based on statistical analysis, it is important to have access to a large amount of image data and a careful evaluation of systemic errors during image acquisition, data preprocessing such as voxel resampling or binning, and parameter settings for texture analysis.

Two concerning problems regarding the authenticity and reproducibility of the

identified texture features involve the inherent variability of patient characteristics or image acquisition procedure, and the sensitivity of texture features with respect to image noise or computational parameter settings. Therefore, the rapid adoption of radiomics in medical imaging also brings along more attentions towards such quality control concerns. Normalization tools to account for multi-center image data collection are developed such as the ComBat Method proposed by Orlhac et al.^{71,72} More studies have been conducted to identify the effects of imaging parameters such as voxel size, number of gray levels or in the case of CT scans, tube current and voltage on the outcome of highly computational texture features.⁷³⁻⁷⁵ Trial and error still remains a reliable method to determine certain parameter settings for texture analysis. As heterogeneity calculation algorithms are developed based on either the variation of image intensity, spatial information or a combination of those two, choosing the adequate resampling voxel size, binning levels and the neighboring voxels will strongly affect the outcome.⁷³ For example, too many gray levels (or too little binning) results in the possibility of reporting image noise as texture heterogeneity. On the other hand, too few gray levels (or too much binning) could end up over-smoothing the image data thus overlooking important texture features. Additionally, patient variability produces sources of variation that are both inevitable, making data normalization a challenging task. For instance, radiomics analysis on contrast CT scans is prone to the variation of patient metabolism rate, which could significantly affect the level of circulating contrast agent – a factor that determines the image intensity on CT scans. While the strength of radiomics lies in the robustness of algorithms that could account for the variation of biological factors, mostly by using large image data to prove its sensitivity and reproducibility, it is important to acknowledge possible sources of bias especially at

the early phase of a study with trial-and-error testing or algorithm training with a modest data set. Therefore, a clear understanding of the computation concepts of radiomics as well as keen insights on the biological factors being assessed is of paramount importance to researchers in this emerging field.

2.5.2 Radiomics analysis in the context of PDAC

Since tumor heterogeneity is a hallmark of PDAC cancer, an increasing number of studies have exploited radiomics analysis to evaluate clinical PDAC image data. Texture features are identified and employed in a wide range of applications such as classification of resection margin status,⁷⁶ prediction of chemotherapy outcome or local control after radiation therapy,^{77,78} lesion stratification,⁷⁹ or monitoring of chemoradiation treatment responses.⁸⁰ The common features reported with significant clinical values are first-order parameters such as the mean and the standard deviation of CT intensity, histogram-based kurtosis, and second-order features extracted from the Gray Level Co-Occurrence Matrix (GLCM) to characterize texture heterogeneity.

2.6 References

1. Quiñonero, F. *et al.* The challenge of drug resistance in pancreatic ductal adenocarcinoma: a current overview. *Cancer Biology and Medicine* **16**, 688–699 (2019).
2. Mbeunkui, F., Johann, D. J. & Jr. Cancer and the tumor microenvironment: a review of an essential relationship. *Cancer Chemother. Pharmacol.* **63**, 571–82 (2009).
3. Kalluri, R. & Zeisberg, M. Fibroblasts in cancer. *Nature Reviews Cancer* **6**, 392–401 (2006).
4. Liotta, L. A. & Kohn, E. C. The microenvironment of the tumour - Host interface. *Nature* **411**, 375–379 (2001).

5. Chauhan, V. P., Stylianopoulos, T., Boucher, Y. & Jain, R. K. Delivery of Molecular and Nanoscale Medicine to Tumors: Transport Barriers and Strategies. *Annu. Rev. Chem. Biomol. Eng.* **2**, 281–298 (2011).
6. Nia, H. T., Munn, L. L. & Jain, R. K. Mapping Physical Tumor Microenvironment and Drug Delivery. *Clin. Cancer Res.* **25**, 2024–2026 (2019).
7. Haeberle, L. *et al.* Stromal heterogeneity in pancreatic cancer and chronic pancreatitis. *Pancreatology* **18**, 536–549 (2018).
8. Apte, M. V. *et al.* Pancreatic cancer: The microenvironment needs attention too! *Pancreatology* **15**, S32–S38 (2015).
9. Xu, Z., Pothula, S. P., Wilson, J. S. & Apte, M. V. Pancreatic cancer and its stroma: A conspiracy theory. *World Journal of Gastroenterology* **20**, 11216–11229 (2014).
10. Kota, J., Hancock, J., Kwon, J. & Korc, M. Pancreatic cancer: Stroma and its current and emerging targeted therapies. *Cancer Lett.* **391**, 38–49 (2017).
11. Torosean, S. *et al.* Nanoparticle uptake in tumors is mediated by the interplay of vascular and collagen density with interstitial pressure. (2013). doi:10.1016/j.nano.2012.07.002
12. Jain, R. K., Martin, J. D. & Stylianopoulos, T. The role of mechanical forces in tumor growth and therapy. *Annu. Rev. Biomed. Eng.* **16**, 321–46 (2014).
13. Nissen, N. I., Karsdal, M. & Willumsen, N. Collagens and Cancer associated fibroblasts in the reactive stroma and its relation to Cancer biology. *J. Exp. Clin. Cancer Res.* **38**, 115 (2019).
14. Padera, T. P. *et al.* Pathology: cancer cells compress intratumour vessels. *Nature* **427**, 695 (2004).
15. Stylianopoulos, T. *et al.* Causes, consequences, and remedies for growth-induced solid stress in murine and human tumors. *Proc. Natl. Acad. Sci. U. S. A.* **109**, 15101–8 (2012).
16. Wijeratne, P. A. *et al.* Multiscale modelling of solid tumour growth: the effect of collagen micromechanics. *Biomech. Model. Mechanobiol.* **15**, 1079–1090 (2016).
17. Kalli, M. & Stylianopoulos, T. Defining the Role of Solid Stress and Matrix Stiffness in Cancer Cell Proliferation and Metastasis. *Front. Oncol.* **8**, 55 (2018).
18. Pirentis, A. P. *et al.* Remodeling of extracellular matrix due to solid stress accumulation during tumor growth. *Connect. Tissue Res.* **56**, 345–354 (2015).
19. Grasso, C., Jansen, G. & Giovannetti, E. Drug resistance in pancreatic cancer:

- Impact of altered energy metabolism. *Critical Reviews in Oncology/Hematology* **114**, 139–152 (2017).
20. Aukland, K. & Reed, R. K. Interstitial-lymphatic mechanisms in the control of extracellular fluid volume. *Physiol. Rev.* **73**, 1–78 (1993).
 21. Mohammadi, M. & Chen, P. Effect of microvascular distribution and its density on interstitial fluid pressure in solid tumors: A computational model. *Microvasc. Res.* **101**, 26–32 (2015).
 22. Boucher, Y. & Jain, R. K. Microvascular pressure is the principal driving force for interstitial hypertension in solid tumors: implications for vascular collapse. *Cancer Res.* **52**, 5110–4 (1992).
 23. Galván, J. A. *et al.* Expression of E-cadherin repressors SNAIL, ZEB1 and ZEB2 by tumour and stromal cells influences tumour-budding phenotype and suggests heterogeneity of stromal cells in pancreatic cancer. *Br. J. Cancer* **112**, 1944–1950 (2015).
 24. Sugimoto, H., Mundel, T. M., Kieran, M. W. & Kalluri, R. Identification of fibroblast heterogeneity in the tumor microenvironment. *Cancer Biol. Ther.* **5**, 1640–1646 (2006).
 25. Fadnes, H. O., Reed, R. K. & Aukland, K. Interstitial fluid pressure in rats measured with a modified wick technique. *Microvasc. Res.* **14**, 27–36 (1977).
 26. Wiig, H., Reed, R. K. & Aukland, K. Measurement of interstitial fluid pressure in dogs: Evaluation of methods. *Am. J. Physiol. - Hear. Circ. Physiol.* **253**, (1987).
 27. Ozerdem, U. & Hargens, A. R. A simple method for measuring interstitial fluid pressure in cancer tissues. *Microvasc. Res.* **70**, 116–120 (2005).
 28. Ozerdem, U. Measuring interstitial fluid pressure with fiberoptic pressure transducers. *Microvasc. Res.* **77**, 226–229 (2009).
 29. Nia, H. T. *et al.* Solid stress and elastic energy as measures of tumour mechanopathology. *Nat. Biomed. Eng.* **1**, 0004 (2016).
 30. Nieskoski, M. D. *et al.* Separation of Solid Stress From Interstitial Fluid Pressure in Pancreas Cancer Correlates With Collagen Area Fraction. *J. Biomech. Eng.* **139**, 061002 (2017).
 31. Angiogenesis, microvascular architecture, microhemodynamics, and interstitial fluid pressure during early growth of human adenocarcinoma LS174T in SCID mice - PubMed. Available at: <https://pubmed.ncbi.nlm.nih.gov/1384965/>. (Accessed: 14th March 2021)
 32. Kamoun, W. S. *et al.* Simultaneous measurement of RBC velocity, flux,

- hematocrit and shear rate in vascular networks. *Nat. Methods* **7**, 655–660 (2010).
33. Kamoun, W. S. *et al.* Simultaneous measurement of RBC velocity, flux, hematocrit and shear rate in vascular networks. *Nat. Methods* **7**, 655–60 (2010).
 34. Vascular permeability and microcirculation of gliomas and mammary carcinomas transplanted in rat and mouse cranial windows - PubMed. Available at: <https://pubmed.ncbi.nlm.nih.gov/8062241/>. (Accessed: 14th March 2021)
 35. Berk, D. A., Yuan, F., Leunig, M. & Jain, R. K. Fluorescence photobleaching with spatial Fourier analysis: measurement of diffusion in light-scattering media. *Biophys. J.* **65**, 2428–2436 (1993).
 36. Rath, N. & Olson, M. F. Regulation of pancreatic cancer aggressiveness by stromal stiffening. *Nat. Med.* **22**, 462–463 (2016).
 37. Laklai, H. *et al.* Genotype tunes pancreatic ductal adenocarcinoma tissue tension to induce matricellular fibrosis and tumor progression. *Nat. Med.* **22**, 497–505 (2016).
 38. Nieskoski, M. D. *et al.* Collagen Complexity Spatially Defines Microregions of Total Tissue Pressure in Pancreatic Cancer. *Sci. Rep.* **7**, 10093 (2017).
 39. Rice, A. J. *et al.* Matrix stiffness induces epithelial–mesenchymal transition and promotes chemoresistance in pancreatic cancer cells. *Oncogenesis* **6**, e352–e352 (2017).
 40. Provenzano, P. P., Inman, D. R., Eliceiri, K. W., Trier, S. M. & Keely, P. J. Contact guidance mediated three-dimensional cell migration is regulated by Rho/ROCK-dependent matrix reorganization. *Biophys. J.* **95**, 5374–5384 (2008).
 41. Fang, M., Yuan, J., Peng, C. & Li, Y. Collagen as a double-edged sword in tumor progression. doi:10.1007/s13277-013-1511-7
 42. Pankova, D. *et al.* Cancer-associated fibroblasts induce a collagen cross-link switch in tumor stroma. *Mol. Cancer Res.* **14**, 287–295 (2016).
 43. Dewhirst, M. W. & Secomb, T. W. Transport of drugs from blood vessels to tumour tissue. *Nature Reviews Cancer* **17**, 738–750 (2017).
 44. Burris, H. A. *et al.* Improvements in survival and clinical benefit with gemcitabine as first- line therapy for patients with advanced pancreas cancer: A randomized trial. *J. Clin. Oncol.* **15**, 2403–2413 (1997).
 45. Von Hoff, D. D. *et al.* Increased Survival in Pancreatic Cancer with nab-Paclitaxel plus Gemcitabine. *N. Engl. J. Med.* **369**, 1691–1703 (2013).
 46. Moore, M. J. *et al.* Erlotinib plus gemcitabine compared with gemcitabine alone in

- patients with advanced pancreatic cancer: A phase III trial of the National Cancer Institute of Canada Clinical Trials Group. *J. Clin. Oncol.* **25**, 1960–1966 (2007).
47. Valsecchi, M. E., Díaz-Cantón, E., de la Vega, M. & Littman, S. J. Recent treatment advances and novel therapies in pancreas cancer: a review. *J. Gastrointest. Cancer* **45**, 190–201 (2014).
 48. Conroy, T. *et al.* FOLFIRINOX versus Gemcitabine for Metastatic Pancreatic Cancer. *N. Engl. J. Med.* **364**, 1817–1825 (2011).
 49. Faris, J. E. *et al.* FOLFIRINOX in Locally Advanced Pancreatic Cancer: The Massachusetts General Hospital Cancer Center Experience. *Oncologist* **18**, 543–548 (2013).
 50. Muranaka, T. *et al.* Comparison of efficacy and toxicity of FOLFIRINOX and gemcitabine with nab-paclitaxel in unresectable pancreatic cancer. *J. Gastrointest. Oncol.* **8**, 566–571 (2017).
 51. Van Mackelenbergh, M. G. *et al.* Clinical trials targeting the stroma in pancreatic cancer: A systematic review and meta-analysis. *Cancers* **11**, (2019).
 52. Kessler, E. R. *et al.* Phase i trial of vandetanib in combination with gemcitabine and capecitabine in patients with advanced solid tumors with an expanded cohort in pancreatic and biliary cancers. *Invest. New Drugs* **34**, 176–183 (2016).
 53. Javle, M. *et al.* Bevacizumab combined with gemcitabine and capecitabine for advanced pancreatic cancer: A phase II study. *Br. J. Cancer* **100**, 1842–1845 (2009).
 54. Seo, Y., Baba, H., Fukuda, T., Takashima, M. & Sugimachi, K. High expression of vascular endothelial growth factor is associated with liver metastasis and a poor prognosis for patients with ductal pancreatic adenocarcinoma. *Cancer* **88**, 2239–2245 (2000).
 55. Özdemir, B. C. *et al.* Depletion of carcinoma-associated fibroblasts and fibrosis induces immunosuppression and accelerates pancreas cancer with reduced survival. *Cancer Cell* **25**, 719–34 (2014).
 56. Neesse, A. *et al.* Stromal biology and therapy in pancreatic cancer. *Gut* **60**, 861–8 (2011).
 57. Dougherty, T. J. *et al.* Photodynamic therapy. *Journal of the National Cancer Institute* **90**, 889–905 (1998).
 58. Agostinis, P. *et al.* Photodynamic therapy of cancer: An update. *CA. Cancer J. Clin.* **61**, 250–281 (2011).
 59. Chen, B. *et al.* Tumor vascular permeabilization by vascular-targeting

- photosensitization: Effects, mechanism, and therapeutic implications. *Clin. Cancer Res.* **12**, 917–923 (2006).
60. Gao, W. *et al.* Photodynamic therapy induced enhancement of tumor vasculature permeability using an upconversion nanoconstruct for improved intratumoral nanoparticle delivery in deep tissues. *Theranostics* **6**, 1131–1144 (2016).
 61. Snyder, J. W., Greco, W. R., Bellnier, D. A., Vaughan, L. & Henderson, B. W. Photodynamic Therapy: A Means to Enhanced Drug Delivery to Tumors. *Cancer Res.* **63**, 8126–8131 (2003).
 62. Huang, H.-C. *et al.* Photodynamic Priming Mitigates Chemotherapeutic Selection Pressures and Improves Drug Delivery. *Cancer Res.* **78**, 558–571 (2018).
 63. Obaid, G. *et al.* Impacting Pancreatic Cancer Therapy in Heterotypic in Vitro Organoids and in Vivo Tumors with Specificity-Tuned, NIR-Activable Photoimmunonanoconjugates: Towards Conquering Desmoplasia? *Nano Lett.* **19**, 7573–7587 (2019).
 64. Huang, H.-C. *et al.* Photodynamic therapy synergizes with irinotecan to overcome compensatory mechanisms and improve treatment outcomes in pancreatic cancer. *Cancer Res.* **76**, 1066 (2016).
 65. Gomer, C. J., Ferrario, A., Luna, M., Rucker, N. & Wong, S. Photodynamic therapy: Combined modality approaches targeting the tumor microenvironment. *Lasers Surg. Med.* **38**, 516–521 (2006).
 66. Spring, B. Q., Rizvi, I., Xu, N. & Hasan, T. The role of photodynamic therapy in overcoming cancer drug resistance. *Photochem. Photobiol. Sci.* **14**, 1476–91 (2015).
 67. Van Griethuysen, J. J. M. *et al.* Computational radiomics system to decode the radiographic phenotype. *Cancer Res.* **77**, e104–e107 (2017).
 68. Pfaehler, E., Zwanenburg, A., de Jong, J. R. & Boellaard, R. RaCaT: An open source and easy to use radiomics calculator tool. *PLoS One* **14**, e0212223 (2019).
 69. Nioche, C. *et al.* Lifex: A freeware for radiomic feature calculation in multimodality imaging to accelerate advances in the characterization of tumor heterogeneity. *Cancer Res.* **78**, 4786–4789 (2018).
 70. Szczypiński, P. M., Strzelecki, M., Materka, A. & Klepaczko, A. MaZda-A software package for image texture analysis. *Comput. Methods Programs Biomed.* **94**, 66–76 (2009).
 71. Orlhac, F., Frouin, F., Nioche, C., Ayache, N. & Buvat, I. Validation of a method to compensate multicenter effects affecting CT radiomics. *Radiology* **291**, 53–59 (2019).

72. Orlhac, F. *et al.* A postreconstruction harmonization method for multicenter radiomic studies in PET. *J. Nucl. Med.* **59**, 1321–1328 (2018).
73. Shafiq-Ul-Hassan, M. *et al.* Intrinsic dependencies of CT radiomic features on voxel size and number of gray levels. *Med. Phys.* **44**, 1050–1062 (2017).
74. Mackin, D. *et al.* Effect of tube current on computed tomography radiomic features. *Sci. Rep.* **8**, 2354 (2018).
75. Fave, X. *et al.* Preliminary investigation into sources of uncertainty in quantitative imaging features. *Comput. Med. Imaging Graph.* **44**, 54–61 (2015).
76. Kulkarni, A. *et al.* Hypovascular pancreas head adenocarcinoma: CT texture analysis for assessment of resection margin status and high-risk features. *Eur. Radiol.* **30**, 2853–2860 (2020).
77. Cheng, S.-H., Cheng, Y.-J., Jin, Z.-Y. & Xue, H.-D. Unresectable pancreatic ductal adenocarcinoma: Role of CT quantitative imaging biomarkers for predicting outcomes of patients treated with chemotherapy. *Eur. J. Radiol.* **113**, 188–197 (2019).
78. Cozzi, L. *et al.* Computed tomography based radiomic signature as predictive of survival and local control after stereotactic body radiation therapy in pancreatic carcinoma. *PLoS One* **14**, e0210758 (2019).
79. Dalal, V. *et al.* Radiomics in stratification of pancreatic cystic lesions: Machine learning in action. *Cancer Letters* **469**, 228–237 (2020).
80. Chen, X. *et al.* Assessment of treatment response during chemoradiation therapy for pancreatic cancer based on quantitative radiomic analysis of daily CTs: An exploratory study. *PLoS One* **12**, e0178961 (2017).

Chapter 3: Relationship of Tumor Vasculature and Collagen Content to Verteporfin Distribution in PDAC tumors

This chapter is derived from:

P. Vincent, et al., “Verteporfin heterogeneity in pancreatic adenocarcinoma and the relationship to tumor vasculature and collagen distribution.” *SPIE-Intl Soc Optical Eng.* (2018) 10476, 45. <https://doi.org/10.1117/12.2309291>

3.1 Introduction

Over the past decades, cancer research has greatly improved the patient outcome for a majority of cancer types. However, patients who suffer from pancreatic adenocarcinoma have faced nearly the same outcome as of years ago. Compared to current breast cancer’s 5-year survival rate of more than 80%, the abysmal rate of 7% for PDAC have not changed considerably.^{1,2} Moreover, pancreatic cancer has risen to be the fourth leading cause of cancer death and is expected to be the second in the US in the next decade.³ This alarming trend has called for monumental efforts in improving both treatment and diagnosis for PDAC. While active research fields contributing to PDAC treatments still preserve a heavy focus on conventional methods like surgery and chemotherapy, emerging research directions have investigated novel therapy regimens involving radiation therapy or ablative treatments. Among those, photodynamic therapy – a process that uses light to kill tissues – is a potentially promising solution due to its non-mutagenic and non-scarring nature.^{4,5} PDT has been widely used and FDA approved for some skin treatments, and the method is currently going under clinical trials for pancreatic cancer.⁶

Along with attempts to come up with novel treatment methods, it is also as important to improve current treatment efficacy. This study was conducted with the motivation to explore the issue of photodynamic drug-resistance in PDT for pancreatic cancer, specifically with verteporfin as the photosensitizer. Verteporfin is being used in clinical trials and could be injected intravenously with adequate accumulation time in tumors for PDT applications. However, similar to many other drugs, verteporfin also suffers from drug-resistance nature of tumors. Drug-resistance can be attributed to both inherent or acquired mechanisms.⁷ One inherent mechanism proposed by Provenzano et al suggested that the characteristic enhancement of desmoplastic reaction in PDAC in addition to reduced vascular patency resulted in limited drug uptake in the tumors.⁸ In a recent work, Nieskoski et al. observed extreme heterogeneity in solid stress within tumor tissue, which was found to be correlated with collagen, the main component of tumor stroma.⁹ These findings and similar others have fueled the drive to carry this study. With hopes to answer the question of poor drug uptake in pancreatic PDT, this study was established to examine tissue parameters at a microenvironmental level. Collagen and vascular patency were quantified to investigate their relationships with verteporfin uptake. It was hypothesized that highly dense and complexed stroma along with limited vascular patency were responsible for the verteporfin heterogeneity in PDAC.

3.2 Materials and Methods

3.2.1 Animal and Tumor Models

All animal procedures were conducted under the protocol approved by the Dartmouth Institutional Animal Care and Use Committee (IACUC). Five female athymic nude mice between the age of 6 to 8 weeks were used in this study. Three mice were

injected with the human tumor cell line AsPC-1 (ATCC, Cat#CRL-1682) and the other two with BxPC-3 (ATCC, Cat#CRL-1687). The orthotopic implantation was done using 1×10^6 tumor cells mixed in RPMI-1640 medium and Matrigel (BD Biosciences, San Jose, CA). Tumors were allowed to grow until they reached ideal imaging size of 10-15mm diameter. Growth time period was up to 3 weeks for AsPC-1 and 5 weeks for BxPC-3. The mice went on a purified diet to limit fluorescence from food consumption and thus better prepare them for fluorescence imaging.

3.2.2 Verteporfin Preparation and ex vivo Fluorescence Acquisition

The contrast agent investigated in this study was Verteporfin (USP, Rockville, MD, USA), which is commonly used in photodynamic therapy.¹⁰ Verteporfin was dissolved in Dimethyl Sulfoxide then intravenously injected at a concentration of 1mg/kg. Two minutes before sacrificing time, the mice were injected with Lectin (Vector Laboratories, Cat#FL-1211) at a dose of 1mg/kg. Lectin acted as a fluorescent stain to mark vascular patency with more details described in the next section. The mice were sacrifice at 1 hour post injection for AsPC-1 and 30min post injection for BxPC-3. These time points were empirically determined as the optimal delivery time to yield high concentration of verteporfin uptake in pancreatic tumors for the two cell lines. Tumors were resected then thinly sliced into 3mm tissue sections for fluorescence imaging. Fluorescent signals were imaged by a flatbed scanner (GE Typhoon 9410) using a 633nm excitation source and 685nm long-pass filter. White light images of tumor sections were also obtained to keep track of the sections' orientation, which was useful in matching the corresponding pathology images. Fluorescence intensity was normalized by fluorescence signal from a

reference signal from blue foam material which was always constant. Normalization was calculated using the formula below:

$$\text{Normalized Fluorescence Signal} = \frac{\text{Sample signal} - \text{Background signal}}{\text{Reference signal} - \text{Background signal}}$$

3.2.3 Pathology Images of Tissue Parameters

After fluorescence imaging, the tumor sections were fixed in 10% formalin then embedded in paraffin. The sections were cut into 4um slices for Masson's Trichrome staining which marked collagen content within the tumors. Lectin sections were coverslipped with DAPI material to facilitate the imaging process. High-resolution images of these stained sections were provided by a PerkinElmer Vectra3 slide scanner set at 10x magnification. White light acquisition was performed to obtain Masson's Trichrome (MT) images while lectin samples required a FITC filter in fluorescent mode.

3.2.4 Image Processing to Quantify Collagen and Vascular Patency

Co-registration of all image data was performed using the function `cpselect` in MATLAB to obtain common points between the images. A selection of 4 to 7 points was used to do non-rigid transformation. Lectin and verteporfin images were registered to the MT image which acted as the reference. All co-registered image data was illustrated in **Figure 3.1** below. For visualization purposes, collagen map, lectin and verteporfin images were enhanced and contrast adjusted.

MT images were analyzed in MATLAB to extract collagen content which was represented by the blue staining. The color segmentation algorithm was adapted from the MATLAB documentation page titled “Color-based segmentation using the L*a*b color space.”¹¹ The RGB images were first converted to CIE-Lab color space. Three samples were selected to represent the main colors visualized in the images, one of which was the blue stain for collagen. These samples were calculated in Lab space and stored as the color markers. Pixel classification was performed based on the Euclidean distance between that pixel and each of the color markers. The pixel was determined to be of a color if the distance to that color was the smallest. Otsu’s global thresholding was used to obtain the total number of pixels in the image. The percentage of blue pixels over total image pixels determined the values for collagen content within a tumor section.

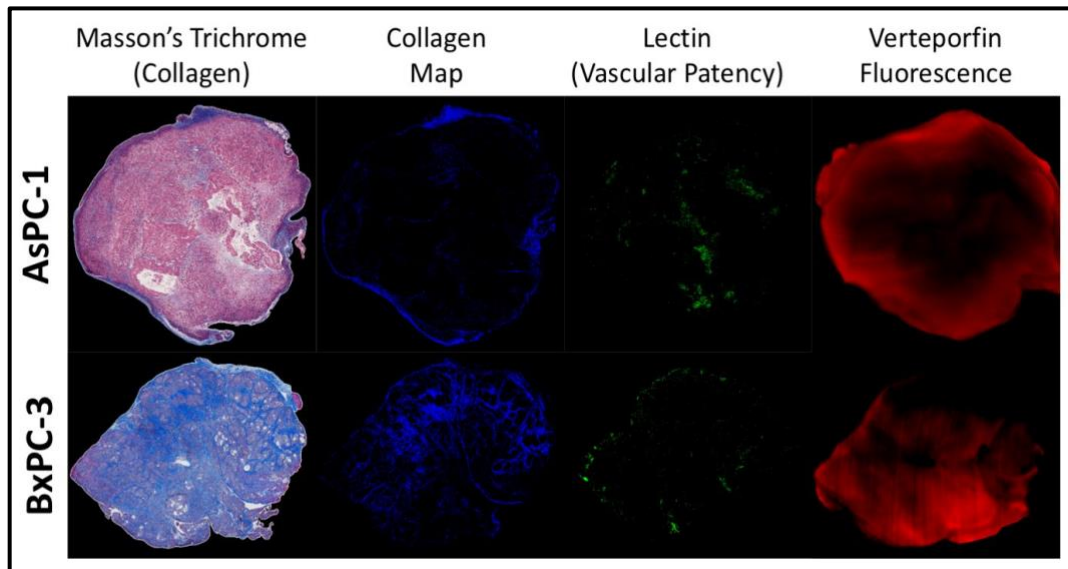


Figure 3.1 All types of image data collected for this study as taken from pathology slices for Masson’s trichrome stain, and Lectin stain, while the Verteporfin fluorescence was taken from thick sections but at the same location.

Lectin image processing started with background subtraction. A mask of tumor tissue was generated by manually drawing regions of interest to exclude adipose tissues,

pancreatic tissues, fluorescence edge effect and artifacts. The images were then thresholded at 0.15 for AsPC-1 and 0.25 for BxPC-3 under the assumption that blood vessels should fall in the range of 1-5% of total tissue area. Pixel ratio of lectin over total tissue area was calculated to yield the patent vessel area fraction percentage.

3.3 Results

3.3.1 Relationship between Verteporfin Uptake and Tissue Parameters

The tissue parameters of interest in this study were collagen and vascular patency.

Figure 3.2A and 3.2C showed the correlation between verteporfin fluorescence and blood vessel area fraction. It was noticed in both tumor cell lines that more blood vessels yielded

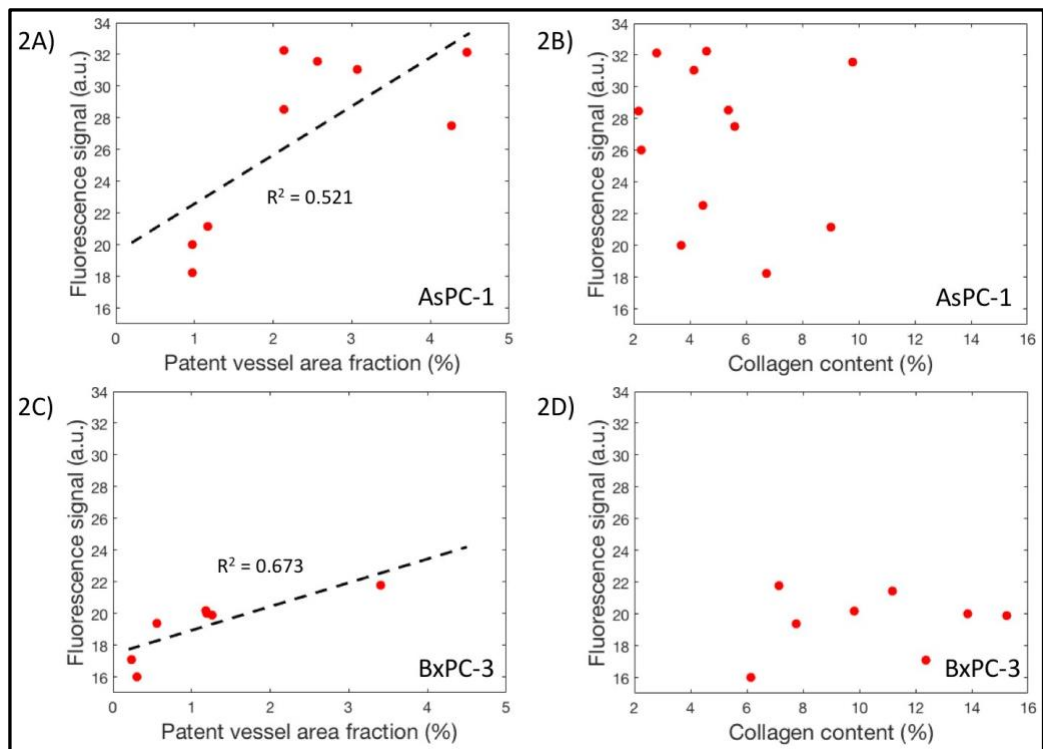


Figure 3.2 The relationship of verteporfin uptake in pancreatic tumor to the collagen percentage and patent vessel area fraction. Each data point represented a whole tumor slice. Fluorescence signal were normalized with a blue foam material.

better drug uptake, which was reasonable since verteporfin was intravenously injected into the bloodstream. Data in **Figure 3.2B and 3.2D** however, showed that drug uptake was independent from collagen content within the tumors. Interestingly, verteporfin signals from AsPC-1 were generally higher than BxPC-3 (mean of 26.94 and 19.18, respectively) while the AsPC-1 collagen values were mostly less than 8% and BxPC-3's were in the 8-15% range. Although there was not any clear correlation for the relationship between collagen and verteporfin within each cell line's data set, the values across the two sets suggested an inverse relationship between these two parameters. The idea of highly collagenated tumor tissue might be a limiting factor to drug uptake had been supported by various work.^{8,9,12,13} Nieskoski et al. proposed that high collagen content in tumor resulted in elevated solid stress, which was proven to be extremely heterogeneous.⁹ The core of his work was based on regional measurements and analysis of pressure and collagen, from which this work differed. Therefore, while whole-slice tumor analysis of collagen distribution revealed some compatible observations to other related work, a future direction this study would like to pursue was the ability to do regional analysis on these tissue parameters. Further discussion on regional analysis was described in the next section.

2.3.2 Regional analysis

Figure 3.3 showcased two examples of the relationship between tissue parameters on a regional level. The examples were taken from the tumor sections with best matches of all image data. The first row (**Figure 3.3a-c**) highlighted the case in which fluorescence sample showed high regional verteporfin uptake (**Figure 3.3c**). This observation was supported by high lectin percentage which denoted large patent vessel area (**Figure 3.3b**). In contrast, collagen map obtained from Figure 3a displayed a lack of collagen tissue in

this region. One could visually see the corresponding differences in the second row (**Figure 3.3d-f**). With high collagen content in **Figure 3.3d**, verteporfin uptake remained low (**Figure 3.3f**) with agreeable results from vascular patency in **Figure 3.3e**. These examples provided justifications for regional analysis of tissue microenvironment. They also

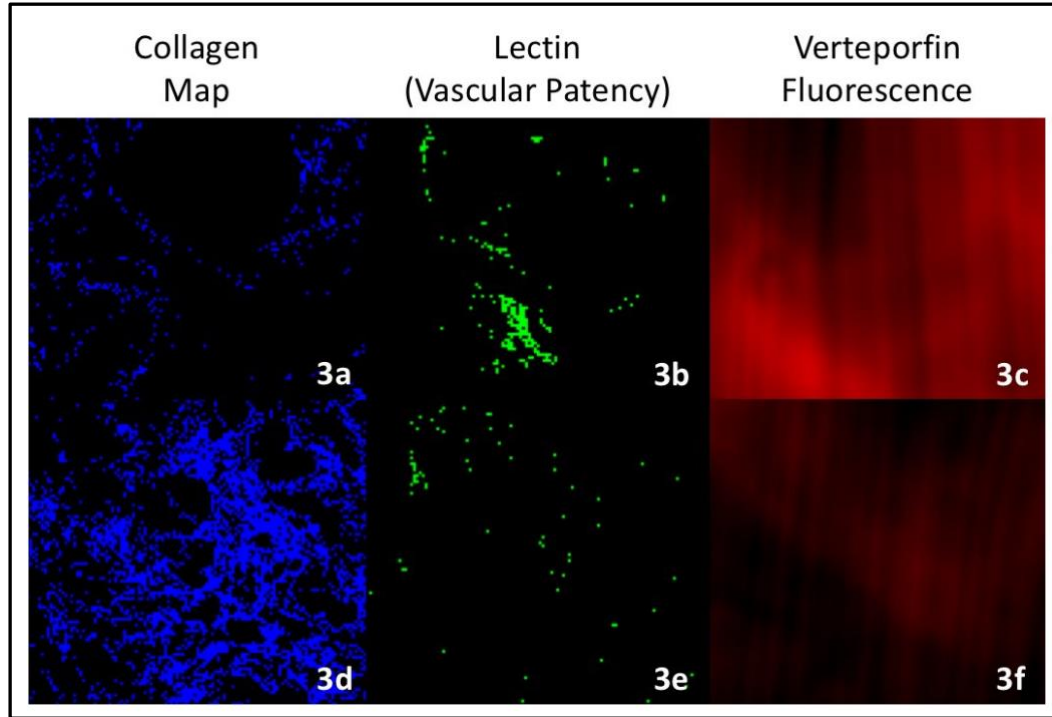


Figure 3.3 *Examples of pancreatic tumor tissues with complexed distribution of collagen and vasculature. 3a-c (low collagen – high lectin – high drug uptake) and 3d-f (high collagen – low lectin – low drug uptake) were two of some regions displayed to not only highlight the heterogeneity within a tumor for all tissue parameters, but also to provide evidence for the potential of tissue microenvironment regional analysis.* confirmed the complexity nature of tissue parameters.

This study’s initial approach was to pursue regional analysis on all types of image data. However, issues had arisen with the quality of image co-registration between fluorescence signal and pathology staining. High-resolution of 1um obtained from pathology images had not been fully exploited since fluorescence imaging of verteporfin only yielded a resolution on the order of 50um. This big mismatch resulted in high tissue

deformation from low-res data or data loss from scaling down high-res samples. Therefore, in order to obtain meaningful and accurate localized information on tissue parameters, a better image transformation algorithm could be used to minimize aforementioned artifacts. More importantly, fluorescence image quality improvement would be extremely beneficial. The current low resolution of verteporfin imaging was attributed to large tissue thickness from fresh cuts and time sensitivity of verteporfin. It would be a big improvement to overcome these two inherent characteristics of verteporfin imaging.

3.4 Conclusion

Research work on tumor microenvironment have shown considerable impact on the understanding of drug-resistance in cancer treatment, and towards solving the delivery problems. Pancreatic cancer tumors are characterized by its dense stroma resulting from fibro-inflammatory response. This study has showed that PDAC, especially BxPC-3, can display high collagen contents of up to 20%. The collagen percentage difference between AsPC-1 and BxPC-3 was reflected by the corresponding overall average drug uptake across the data sets (26.9 vs. 19.2). Although whole-slice analysis within each tumor type referred to verteporfin uptake and collagen independence, this observation gave ground to our future work of regional analysis. This future direction will also involve exploring novel imaging methods for verteporfin in fresh tissue cuts. Linear correlation between verteporfin uptake and vascular patency was supported with data from both AsPC-1 and BxPC-3. It would be beneficial to improve lectin imaging protocol so that less imaging processing would be required to exclude imaging artifacts. Further assessments of verteporfin perfusion within the tumor could be accomplished if verteporfin was imaged at a higher resolution and better co-registration across all image data. In summary, tumor stroma at

microenvironmental level had considerable influence on photosensitizer uptake, which occurred with heterogeneous characteristics.

3.5 Acknowledgments

This work was funded by NIH grant P01CA084203.

3.6 References

1. DeSantis, C., Ma, J., Bryan, L. & Jemal, A. Breast cancer statistics, 2013. *CA. Cancer J. Clin.* **64**, 52–62 (2014).
2. Cancer Statistics Review, 1975-2014 - SEER Statistics. Available at: https://seer.cancer.gov/archive/csr/1975_2014/. (Accessed: 8th March 2021)
3. Siegel, R., Ma, J., Zou, Z. & Jemal, A. Cancer statistics, 2014. *CA. Cancer J. Clin.* **64**, 9–29 (2014).
4. Kufe, D. W., Pollock, R. E., Weichselbaum, R. R., Bast, R. C., Gansler, T. S., Holland, J. F., et al., [Cancer Medicine], 7th ed. Hamilton, Ontario: Decker, Inc., 537–48 (2006).
5. Campbell, S. M., Tyrrell, J., Marshall, R. & Curnow, A. Effect of MAL-photodynamic therapy on hypertrophic scarring. *Photodiagnosis Photodyn. Ther.* **7**, 183–188 (2010).
6. Huggett, M. T. *et al.* Phase I/II study of verteporfin photodynamic therapy in locally advanced pancreatic cancer. *Br. J. Cancer* **110**, 1698–1704 (2014).
7. Spring, B. Q., Rizvi, I., Xu, N. & Hasan, T. The role of photodynamic therapy in overcoming cancer drug resistance. *Photochem. Photobiol. Sci.* **14**, 1476–91 (2015).
8. Provenzano, P. P. *et al.* Enzymatic Targeting of the Stroma Ablates Physical Barriers to Treatment of Pancreatic Ductal Adenocarcinoma. *Cancer Cell* **21**, 418–429 (2012).
9. Nieskoski, M. D. *et al.* Separation of Solid Stress From Interstitial Fluid Pressure in Pancreas Cancer Correlates With Collagen Area Fraction. *J. Biomech. Eng.* **139**, 061002 (2017).
10. Dolmans, D. E. J. G. J., Fukumura, D. & Jain, R. K. Photodynamic therapy for cancer. *Nature Reviews Cancer* **3**, 380–387 (2003).

11. Color-Based Segmentation Using the L*a*b* Color Space - MATLAB & Simulink Example. Available at: <https://www.mathworks.com/help/images/color-based-segmentation-using-the-l-a-b-color-space.html>. (Accessed: 10th March 2021)
12. Chauhan, V. P. *et al.* Angiotensin inhibition enhances drug delivery and potentiates chemotherapy by decompressing tumour blood vessels. *Nat. Commun.* **4**, 2516 (2013).
13. Nieskoski, M. D. *et al.* Collagen Complexity Spatially Defines Microregions of Total Tissue Pressure in Pancreatic Cancer. *Sci. Rep.* **7**, 10093 (2017).

Chapter 4: Relationship of Tumor Stiffness to Tumor Collagen and Using Stiffness as a Surrogate for Drug Delivery Assessment

This chapter is derived from:

P. Vincent, et al., “High-resolution ex vivo elastography to characterize tumor stromal heterogeneity in situ in pancreatic adenocarcinoma.” *IEEE Trans. Biomed. Eng.* Vol. 67, no. 9, pp. 2490-2496. (2020) doi: 10.1109/TBME.2019.2963562.

4.1 Introduction

Poor vascular perfusion leading to low drug penetration persists as a major problem in solid tumor cancer therapeutics¹ and is especially prominent in pancreatic adenocarcinoma (PDAC). When surgical resection is limited by tumor invasion into surrounding major blood vessels, almost all therapeutic options rely upon delivering systemic pharmacologic drugs into the tumor. Understanding and improving tumor drug transport efficiency therefore will benefit chemotherapy, immunotherapy and combinations of any targeted therapies² in this aggressive disease. The inherent drug-resistant nature of PDAC stems from two well-studied phenomena: the heterogeneity of genetic mutations and desmoplastic tumor microenvironment.³ Therapies targeting cancer-associated genetic pathways yield mixed results⁴⁻⁶ since the complexity of molecular signaling mechanisms could lead to upregulation of compensatory pathways. Meanwhile, the dense stroma characteristic of PDAC results in elevated total tissue pressure⁷ that damages tumor vasculature⁸ and the lymphatic system.⁹ Active research on the multifaceted origin of poor tumor transport has not only improved our understanding on the underlying biological mechanisms but has also emphasized the clinical need for a

biomarker that could reflect drug transport efficiency, and the resulting therapeutic response. The daunting search for such a biomarker faces an intrinsic dilemma of spatial size scale mismatch: the micron-scale associated with meaningful genetic and/or biological tumor information versus the clinical need to acquire this data on the centimeter-scale relevant to whole tumor size.

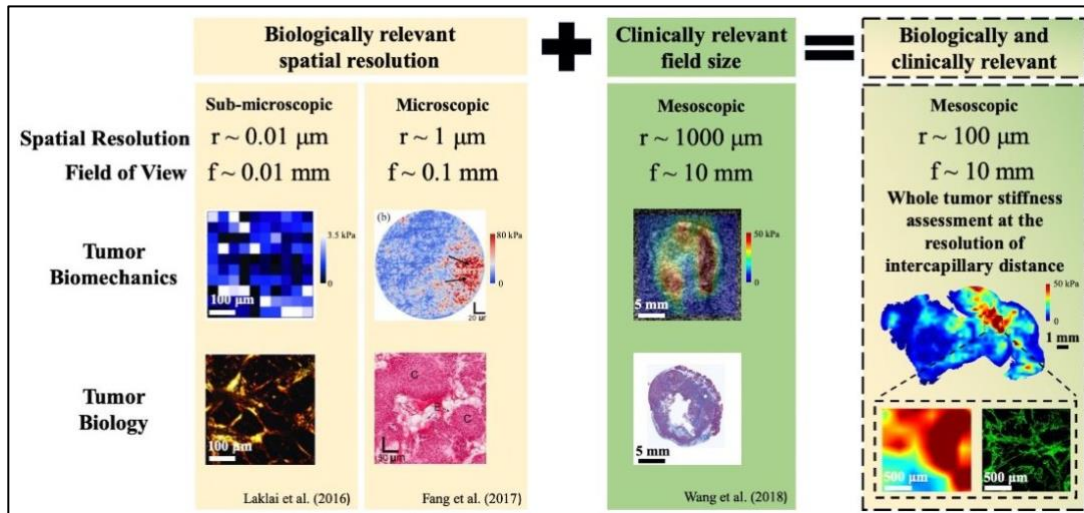


Figure 4.1 Tumor biomechanics and relevant biology information are actively studied at different spatial scales: sub-microscopic¹⁰, microscopic¹² and mesoscopic¹³. Current elastography tools offer either biologically relevant spatial resolution or clinically relevant field of view, none exists that could meet both requirements. Stiffness information as a clinical application to evaluate drug transport brings most benefit when whole tumor stiffness is assessed at inter-capillary distance spatial resolution.

Fortunately, recent findings from both ends of the aforementioned spatial scale range have reported that tumor stiffness could be a potential tool to address drug transport and therapy response. Laklai *et al.* (2010) provided the first direct evidence that linked tumor genotype with desmoplasia, the two constraints of PDAC drug-resistant nature.¹⁰ In this study, tumor stiffness was obtained by atomic force microscopy and data from both clinical and preclinical samples confirmed the potential of elastography to reflect tumor biology changes related to cancer progression and aggression. On the mesoscopic scale,

Harada *et al.* (2017) echoed the linear relationship between tissue stiffness and fibrosis content by showing ultrasound elastography and pathology data from a single patient.¹¹ Ultrasound elastography was also used by Wang *et al.* (2018) to obtain wide-field stiffness information, which was linearly correlated with tumor collagen but inversely correlated with PDAC tumor drug distribution.¹⁴ While these findings underscore the potential use of stiffness imaging, current experimental elastography tools¹⁵ do not meet the two requirements of having biologically meaningful spatial resolution and a clinically relevant field of view. **Fig. 4.2** illustrates basic elastography tools with atomic force microscopy (AFM) and multiphoton microscopy harmonic imaging (MPM) being widely explored to characterize very small regions of tissue. Optical coherence elastography (OCE) or ultrasound elastography (UE) are non-invasive, however OCE has a small field of view ($f < 1$ mm, up to 5mm with a translation stage) with high spatial resolution ($r \approx 0.01$ mm) while UE has a higher field of view ($f \approx 10$ mm) but limited spatial resolution ($r \approx 1$ mm).

In order to study PDAC tumor stiffness at a clinically relevant size scale with biologically meaningful spatial resolution, we developed a novel, cost-effective *ex vivo* elastography (EVE) mapping system. EVE equipped by a translation stage was able to map tumor stiffness at 300-micron resolution in pancreatic xenograft tumors with 1-cm diameter. This spatial resolution is sufficient to study tumor drug distribution, since intratumoral transport primarily relies on diffusion between blood vessels.¹ Additionally, our previous studies have showed that the spatial scale of relevant variation in tumor solid stress is hundreds of microns, matching the known intercapillary distances.¹⁶ Stiffness of the tumor also appears to be linked to the complexity¹⁶ and thickness¹⁰ of the collagen grown within the desmoplastic tissue. Therefore, EVE provides an adequate spatial

resolution and field of view so that elastography information could be assessed globally and regionally, compensating for both microscopic and mesoscopic elastography tools (Fig. 4.1). In this study, the methodology for whole-tumor stiffness mapping was developed and verified with data from two orthotopic PDAC xenograft models. The relationship between stiffness and tumor microenvironment was examined by quantifying tumor collagen from pathology images to provide direct visualization of stiffness and stroma variations in whole-tumor size. Finally, tumor transport parameters such as patent vessels and drug distribution via fluorescence imaging were investigated to determine the spatial relationship between stiffness, perfused vasculature and resulting drug penetration.

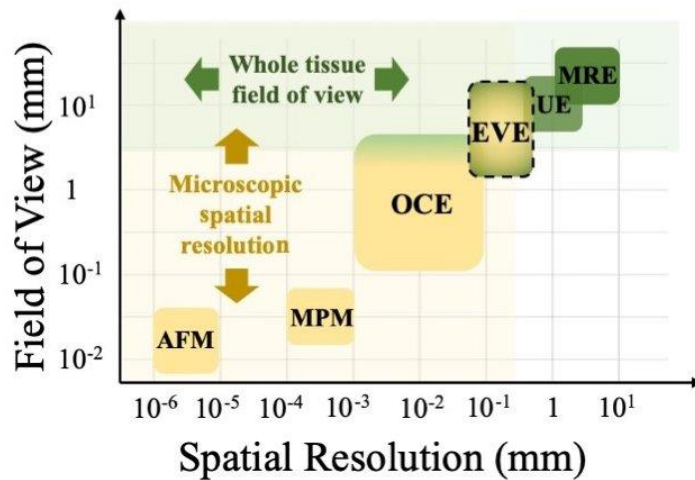


Figure 4.2 Current experimental techniques for assessing features related to tumor stiffness. Common elastography assessment tools and their positions in the field include AFM: atomic force microscopy, MPM: multi-photon microscopy harmonic imaging, OCE: optical coherence elastography, UE: ultrasound elastography, MRE: magnetic resonance elastography. Ideal elastography imaging tools should be placed in the overlap between microscopic resolution region and whole-tissue FOV region. Since no current imaging tool could meet these requirements, ex vivo elastography (EVE) mapping was developed to study PDAC stiffness at relevant biological size scales, with 300-micron spatial resolution and a field of view that would cover a whole PDAC tumor.

4.2 Materials and Methods

4.2.1 Ex vivo Elastography (EVE) mapping system

The system consisted of a fiber optic pressure sensor FOP-M260 (FISO, Quebec, Canada) coupled with a three-dimensional motorized translation table (Velmex, Bloomfield, NY) illustrated in **Fig. 4.3A**. The x-y dimension (table part# MAXY4009, stepping motor part# PK266-03A) was responsible for tracking the spatial coordinates across the tumor surface, and the z-dimension (table part# MA4006, stepping motor part# PK266-03B) controlled the compression displacements applied to determine strain and corresponding pressure values. The pressure sensor operates based on Fabry-Perot interferometer technology (**Fig. 4.3C**). This pressure sensor has been utilized in both preclinical and clinical settings.¹⁷⁻¹⁹ In this application, the pressure readings were converted into electrical signals in the range of 0-5V using the FISO signal conditioning module (part# FPI-LS, FISO, Quebec, Canada). The analog was input to LabVIEW via a data acquisition device USB-6008 (National Instruments, Austin, TX). Pressure data had a resolution of 0.02 kPa and accuracy of 0.13 kPa. The pressure detection range is ± 40 kPa relative to atmospheric pressure. The pressure sensor and the motorized xyz table were controlled by LabVIEW and a simplified flowchart on data acquisition is illustrated in **Fig. 4.3E**. Mapping grid size was adjustable based on the tumor size. On an average tumor surface of 10 x 10 mm, imaging with the 300- μ m resolution probe resulted in a grid size of 35 x 35 points.

EVE validation testing was carried out with agar phantoms to ensure the system could detect relative changes in pressure readings under tumor tissue measuring condition illustrated in **Fig. 4.3A**. Given that the mouse tumor sample thickness was on average 5 mm (L_0), 100- μ m total deformation yielded a maximum of 2% strain ensuring tissue linear elasticity. At least three pressure measurements were required to generate a stress-strain

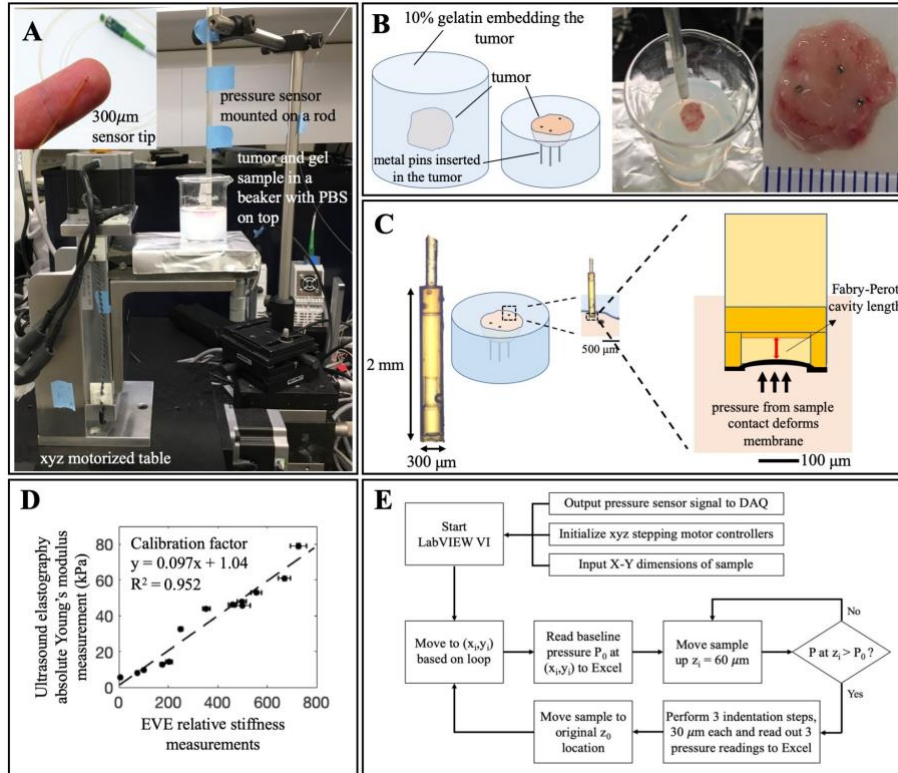


Figure 4.3 Ex vivo elastography (EVE) system and sample preparation. *A) Overall system consists of an xyz- motorized table and a commercial fiber optic pressure sensor. B) Sample preparation procedure includes a tumor embedded in 10% gelatin. Metal pins are inserted to provide markers for image coregistration with pathology data. C) Pressure sensor operates based on Fabry-Perot interferometer technology. The cavity deformation due to external force is calibrated to give a corresponding pressure reading. D) Young's modulus calibration curve between UE and EVE established by phantom measurements at different concentrations and temperatures. E) A simplified flow chart illustrates important steps of stiffness measurement, which includes tumor surface identification and 3-step compression testing.*

curve whose slope was used to determine stiffness, therefore, three indentations (ΔL) were selected to be 30, 60 and 90 μm . At each location, relative stiffness readings were calculated by measuring the slope of the stress-strain curve. For each of 6 varying concentrations of agar phantoms (1%, 1.2%, 1.5%, 1.6%, 1.8% and 2% agar), 21 relative stiffness measurements from 3 samples were obtained. Results from this test showed that EVE was able to detect the linear relationship between increasing agar concentration phantoms and increasing stiffness ($R^2 = 0.98$). There was no significant difference in phantom measurements obtained with and without the beaker confinement illustrated in **Fig. 4.3A-B**. More importantly, stiffness readings obtained from a flat phantom surface (27 ± 3.0 kPa) and from a 15° inclined surface (27 ± 2.4 kPa) were consistent. This test provided evidence that EVE is sufficient to measure stiffness from samples with a high surface irregularity, an inherent characteristic of fresh tissue with high stiffness such as solid pancreatic tumors. Tumor surface detection thus was extended and largely contributed to the average imaging time of 2 hours per tumor.

To convert from relative stiffness measurements to absolute Young's modulus values, EVE system was calibrated by a UE system. The UE system consisted of a Vantage 64 Ultrasound Scanner (Verasonics Inc.) and an L7-4 (Phillips Healthcare) linear transducer array. UE data was collected by using a 400- μs , 7-kHz push pulse to induce shear waves. Young's modulus calculation for this system is described in Wang *et al.* under "Modulus estimation."¹³ A series of gelatin phantoms was fabricated to determine the calibration factor between the EVE relative stiffness measurements and absolute Young's modulus in kPa generated by UE. The calibration curve between two systems is illustrated in **Fig. 4.3D**. The feasibility of EVE system to produce correct stiffness maps is verified

by measurement data from murine organs such as pancreas and spleen tissue. Validation results from this experiment is further discussed in Section IIIA.

4.2.2 Animal and Tumor Model

All animal procedures were conducted under the protocol approved by the Dartmouth Institutional Animal Care and Use Committee (IACUC). 27 athymic nude mice between the age of 6-8 weeks were used in this study. 13 mice were injected with human tumor cell line AsPC-1 (ATCC, Cat# CRL-1682) and the other 14 with BxPC-3 (ATCC, Cat# CRL-1687). The pancreas was exposed and tumor cells were injected with a 1:1 ratio of Matrigel. AsPC-1 and BxPC-3 required 2-4 weeks and 5-7 weeks, respectively, for tumors to reach ideal imaging size of 1 cm in diameter. The mice were on purified diet to reduce autofluorescence from food consumption.

4.2.3 Tumor Sample Preparation

After the tumors reached imaging size, the mice were anesthetized and sacrificed. The resected tumor was then embedded in gel. The gel block consisted of 10% gelatin, 1% cornstarch and 89% water designed to be just stiff enough to hold the bulk of the tumor. The gelatin phantom was sliced in half to provide a flat imaging surface for stiffness mapping (**Fig. 4.3B**). Three metal pins were inserted into the tumor to provide fiducial markers²⁰ for image co-registration between the stiffness map and pathology data. A layer of PBS was applied on the tumor surface to maintain proper hydration. Stiffness measurements from both gelatin and tumor samples confirmed no dehydration problem existed.

4.2.4 Drug Uptake Quantification via Fluorescence Imaging

Verteporfin or BPD (USP, Rockville, MD, USA) was dissolved in dimethyl sulfoxide at 1 mg/ml then diluted with PBS to obtain a final concentration of 0.1 mg/ml. Lectin (Vector Laboratories, Cat#FL-1211) at a concentration of 2 mg/ml was used as vascular patency marker. BPD (1 mg/kg) and lectin (2 mg/kg) were injected intravenously one-hour and 2-minutes, respectively, before sacrifice. Seven out of 13 AsPC-1 mice and 7 out of 14 BxPC-3 mice received these injections. After slicing the gel to expose the tumor surface, fluorescence imaging was immediately performed on fresh tissue by a flatbed scanner (GE Typhoon 700) using a 473 nm excitation source with a 670 nm LP filter. Vascular patency was determined by fluorescence imaging of lectin using a PerkinElmer Vectra3 slide scanner with a FITC filter.

4.2.5 Tumor Biological Parameter Identification

After stiffness mapping, the tumors were fixed in 10% formalin and sectioned at 4-micron thickness. H&E staining was used to identify tumor tissue while Masson's Trichrome (MT) identified collagen fibers by blue staining. All image data was co-registered to MT image (**Fig. 4.4A**) using a rigid transformation in MATLAB. The blue collagen map was segmented from the MT image by converting from RGB to HSV color space and thresholding for blue pixels ($0.5 < \text{hue} < 0.7$, $\text{saturation} > 0.5$ for BxPC-3 and $\text{saturation} > 0.3$ for AsPC-1, $\text{value} > 0.7$). Different saturation cutoffs for each tumor line was necessary to make sure segmented maps truly reflect collagen content within the tumors. Collagen percentage was obtained by finding the ratio of blue pixels over the total tumor tissue area. H&E image was used to identify and exclude non-tumor tissue from analysis. **Fig. 4.4B** showed an example of a tumor sample with pancreas and spleen tissue

attached. ROIs for these regions were manually drawn and subtracted out. Regions of necrosis or dead tumor cells were also excluded. All pathology data procedures aforementioned were confirmed with an animal pathologist.

4.2.6 Statistical Analysis

Statistical analysis was done for determining differences between groups with a Student's t-test performed in MATLAB with a two-tailed analysis and $\alpha = 0.05$. Linear regression and exponential fit of data was done in Excel for data sets with these apparent trends.

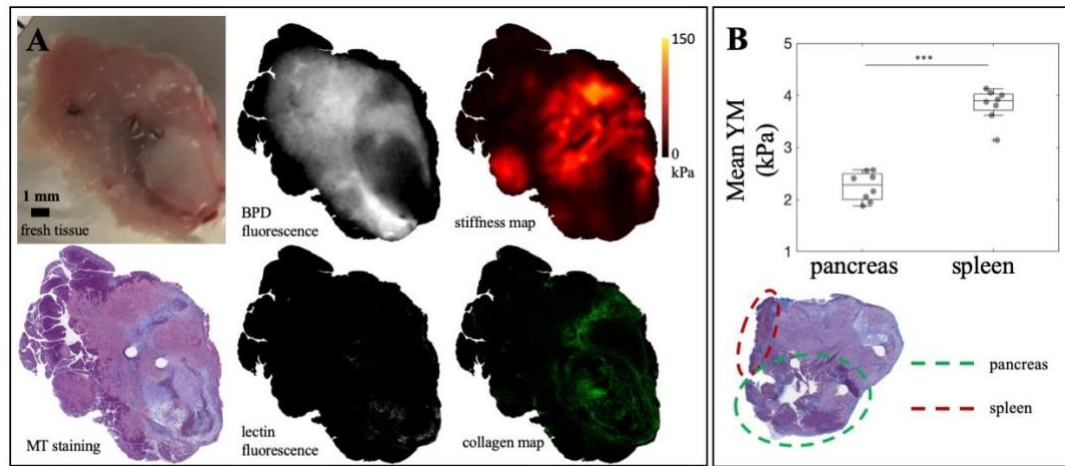


Figure 4.4 Image data and tissue parameter identification process. A) Top row from left to right: fresh tumor surface in gel with inserted metal pins, BPD fluorescence, stiffness map. Bottom row: Masson's Trichrome staining, lectin fluorescence, segmented collagen map from MT staining. All images are co-registered to MT staining data. **B)** Average stiffness detected from spleen (4.0 ± 0.3 kPa) and pancreas (2.3 ± 0.3 kPa). These regions are excluded from tumor analysis by manual ROI drawn on pathology data.

4.3 Results

4.3.1 EVE system detects tumor stiffness heterogeneity and differentiates between tumor, spleen, and pancreas tissue

Fig. 4.4 shows that EVE can detect stiffness heterogeneity as well as distinguish non-tumor tissue and necrotic regions. It is clearly visible from the MT histology image that pancreas tissue (top left) is stained in dark purple, necrotic regions (bottom right) in light pink and viable tumor tissue in darker pink. While it is virtually impossible to identify tumor from pancreas tissue in the white light images, Young's modulus (YM) maps obtained from EVE can distinguish this difference. Both pancreas and necrotic regions were much softer than tumor tissue. **Fig. 4.4B** illustrates the average YM detected from spleen and pancreas tissue, found in 8 samples to be 4.0 ± 0.3 kPa and 2.3 ± 0.3 kPa, respectively. This data set provided validation results for EVE's feasibility to produce correct stiffness maps as these values agree with previously reported YM of murine organs. Yu *et al.* (2018) showed spleen's YM of rats to be 3.9 ± 0.6 kPa while Rice *et al.* (2017) reported mouse pancreas stiffness ranging from 1 to 4 kPa as PDAC progressed in genetically engineered mouse models.^{21,22} Even though these tissues are excluded from tumor analysis in this study, the measurements help to confirm the feasibility of using EVE in tumor stiffness mapping.

4.3.2 EVE system has the resolution necessary to study extracellular matrix (ECM) heterogeneity in PDAC tumors as compared to ultrasound elastography

A comparison between UE and EVE is carried out with the result displayed in **Fig. 4.5**. Ultrasound B mode and elastography map were constructed using an established technique¹⁴. After that, EVE was used to measure tumor stiffness and a side-by-side

comparison is illustrated in **Fig. 4.5A**. Generally, both UE and EVE agree on the level of stiffness heterogeneity in the tumor as well as the location of high stiffness. However, EVE, with the ability to resolve better spatial resolution, reveals a more refined stiffness map that displays similar patterns to the collagen profile in **Fig. 4.5B**. Expanded regions in **Fig. 4.5C** again show that stiffness information at a sufficient spatial resolution can reflect the collagen distribution within tumors.

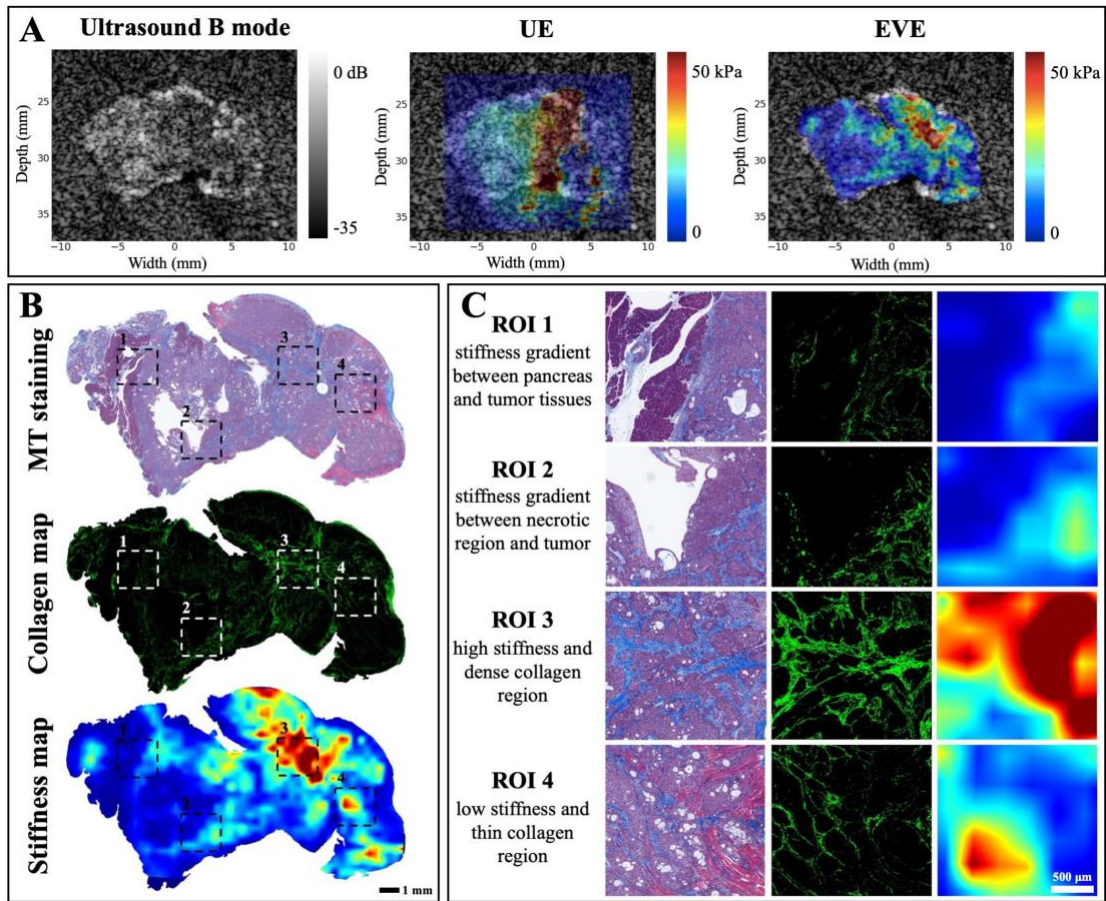


Figure 4.5 Comparison between UE and EVE stiffness map. A) Elastography imaging data from both systems are displayed to highlight similar pattern of stiffness heterogeneity. **B)** Stiffness map obtained from EVE system with better spatial resolution allows for direct comparison between stiffness and collagen pattern in the tumor. **C)** Expanded images of different ROIs highlight the correlation between stiffness and collagen percentage in PDAC tumors

4.3.3 Collagen content in PDAC tumors is correlated with reported Young's modulus values, both of which display extreme heterogeneity

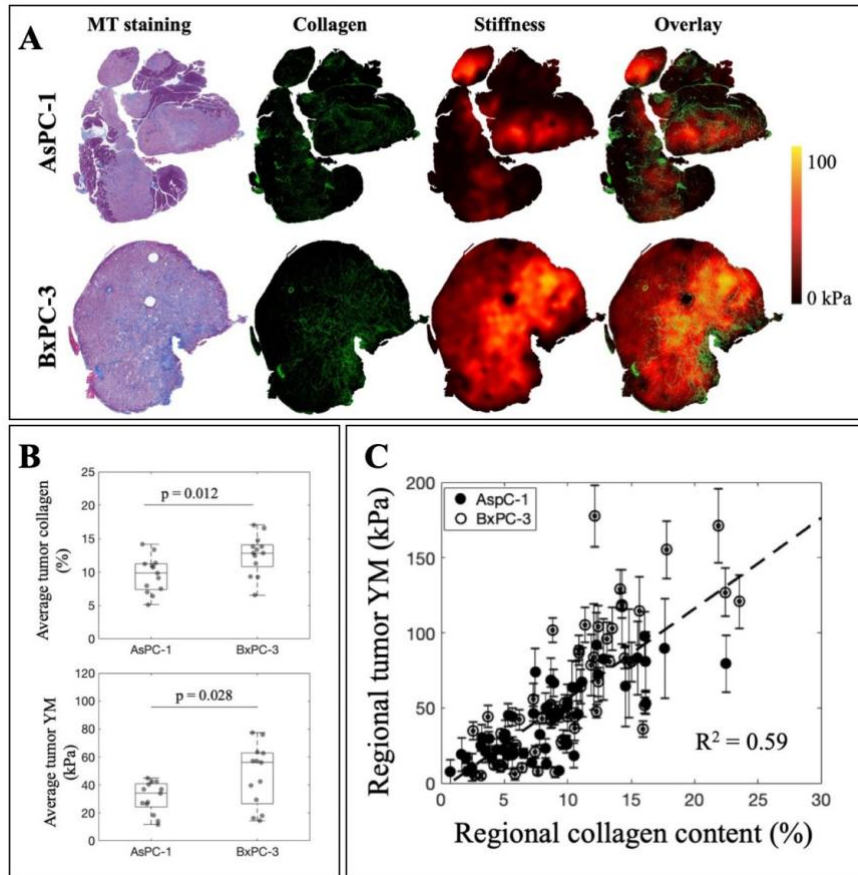


Figure 4.6 Stiffness and collagen content in PDAC tumors are highly correlated both globally and regionally. *A) Visualization of stiffness, collagen and the overlay between two parameters show a good correlation in both AsPC-1 and BxPC-3 tumor lines. B) AsPC-1 tumors contain 9.6 ± 2.7 percent collagen and average stiffness of 32 ± 11 kPa. As for BxPC-3, collagen percentage is averaged at 13 ± 3 percent and stiffness measured at 46 ± 24 kPa. Both of these quantities are statistically significant between AsPC-1 and BxPC-3 tumors. C) Regional analysis to examine high stiffness and low stiffness regions demonstrates a linear correlation between Young's modulus and collagen profile with $R^2 = 0.59$. For each tumor, two high-stiffness and two low-stiffness regions were chosen (AsPC-1: $n = 13$, ROIs = 52; BxPC-3: $n = 14$, ROIs = 56).*

Tumor analysis, both globally and regionally, shows a strong correlation between stiffness and tumor collagen. **Fig. 4.6A** visually represents the high heterogeneity observed in both stiffness and collagen maps for AsPC-1 and BxPC-3 tumors. The overlay of stiffness and collagen information illustrates the agreement of higher stiffness regions with denser collagen regions. **Fig. 4.6B** reports the global average collagen content of AsPC-1 ($n = 13$) and BxPC-3 ($n = 14$) tumors to be 9.6 ± 2.7 percent and 13 ± 3 percent, respectively. Average AsPC-1 tumor stiffness is also lower than BxPC-3 values, 32 ± 11 kPa and 46 ± 24 kPa. Both of these measurements are statistically significant. Regional analysis to investigate both lower stiffness and higher stiffness regions in each tumor shows a linear relationship between Young's modulus values and collagen percentage in tumors, as showed in **Fig. 4.6C** with $R^2 = 0.59$. Regional analysis also suggests that collagen content in the tumors could reach up to 25% and tumor stiffness in between 5 and 150 kPa.

4.3.4 The inverse relationship between stiffness and drug distribution in PDAC tumors suggests the potential of elastography as a surrogate for tumor drug uptake

Whole tumor drug distribution and Young's modulus map are displayed in **Fig. 4.7A** to demonstrate the potential of stiffness as a surrogate for drug uptake globally in PDAC tumors. **Fig. 4.7B** provides regional information to highlight the inverse relationship between drug uptake and tumor stiffness. Less drug is accumulated in ROI 1 which is stiffer and contains more collagen while more uptake is observed in ROI 2 which is softer and has less collagen. In addition, more vessels are recorded in ROI 2 as compared to ROI 1. In **Fig. 4.7C-D**, the inverse relationship of stiffness to both drug uptake and patent vessels is highlighted in both tumor lines. Young's modulus and BPD fluorescence intensity data is a linear fit for both AsPC-1 and BxPC-3 with $R^2 = 0.66$ and $R^2 = 0.59$. More drug is

accumulated in AsPC-1 tumors based on the average fluorescence intensity in **Fig. 4.7C**.

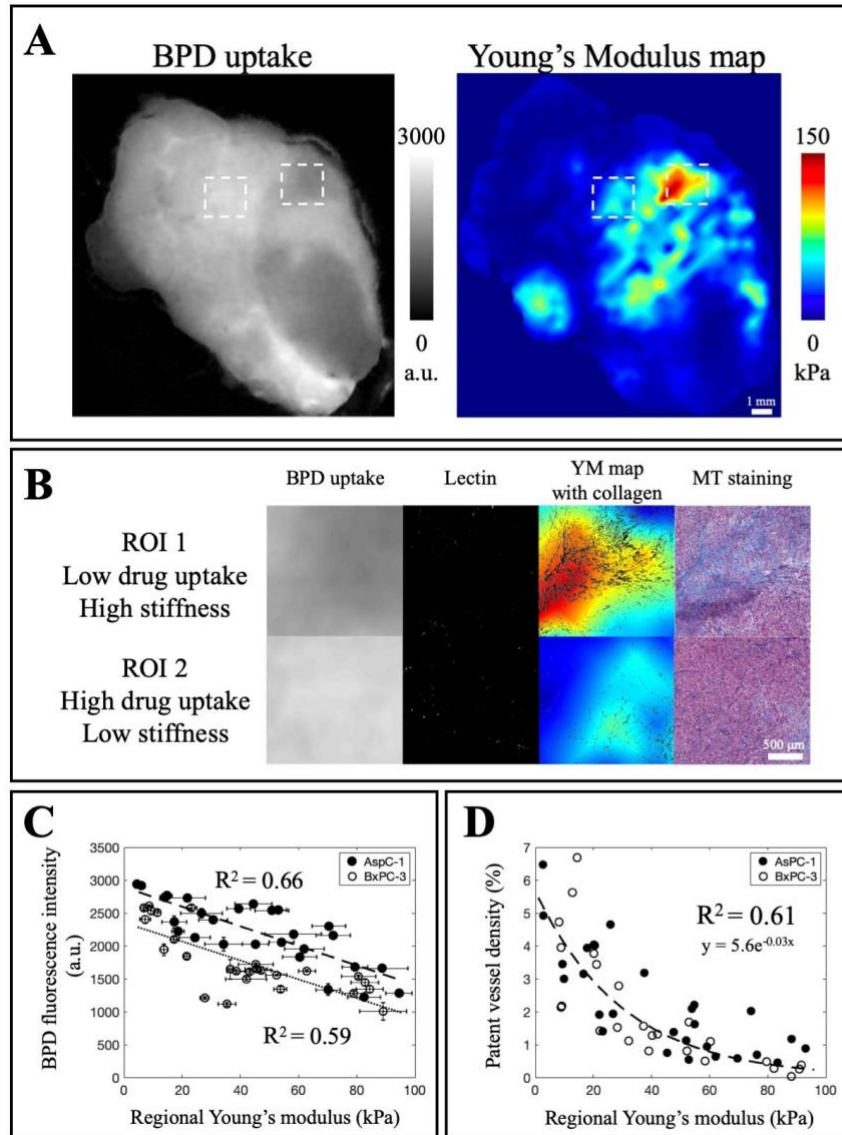


Figure 4.7 PDAC tumor stiffness is inversely correlated with drug uptake and patent vessel data. *A) Whole-tumor visualization of BPD fluorescence distribution and stiffness heterogeneity obtained from EVE. B) Close-up regions of low and high drug uptake reveal the inverse relationship with stiffness and collagen distribution. C) Tumor YM is inversely correlated to BPD distribution in AsPC-1 and BxPC-3, with higher uptake in AsPC-1 tumors. D) Tumor YM limits patent vessels which explains the limited drug penetration. For each tumor, two high-stiffness and two low-stiffness regions were chosen. There were 3 ROIs omitted since the vessel density percentage was essentially zero, and those ROIs had stiffness values greater than 100 kPa. (AsPC-1: $n = 7$, ROIs = 27; BxPC-3: $n = 7$, ROIs = 26).*

Patent vessel density drastically reduces as stiffness increases for both tumor lines as illustrated in **Fig. 4.7D**.

4.4 Discussion

This study demonstrates that ex vivo stiffness mapping at 300-micron resolution could accurately represent the entire tumor-wide stiffness heterogeneity in both AsPC-1 and BxPC-3 xenograft models. The range of variation in stiffness values is visualized by EVE for the first time, to match the same level of variation of collagen network within a tumor (**Fig. 4.5B-C**). In our previous work, Nieskoski *et al.* (2017) generated a prediction of total tissue pressure maps with profound heterogeneity due to the strong correlation between point-probed solid stress measurements and surrounding collagen area fraction in PDAC tumors.¹⁶ This work has confirmed that tumor stiffness is also strongly correlated with stroma variation. Understanding PDAC tumor physical and biological connection is crucial because the practicality of stiffness imaging surpasses other tissue biomechanics quantities due to its non-invasive potential. Meanwhile, this finding emphasizes the need for resolution improvement of wide-field elastography systems such as UE and MRE to be at least on the resolution scale of 100's of microns to truly reflect biological variations in the tumor microenvironment. Furthermore, if imaging of stiffness is not achieved on this small spatial resolution scales, it is conceivable that highly inaccurate stiffness values may be obtained by partial volume averaging of the true values.

When analyzed region by region, the linear relationship between stiffness and collagen content (**Fig. 4.6C**) not only corroborates similar findings measured by UE,¹⁴ but also resonates with clinical data from Harada *et al.* (2017) in which a patient's pancreatic stiffness was correlated with fibrosis percentage ($R^2 = 0.58$).²³ Another clinical study,²⁴ in

which advanced pancreatic cancer patients were treated with nab-paclitaxel to target tumor stroma, came to the conclusion that elastography should be further investigated as data suggested the link between tumor stiffness and stroma modification. The study pointed out that even though the number of activated cancer-associated fibroblasts (CAF) did not change for treated and untreated cohorts, overall tumor stiffness measured by UE decreased for those with treatment responses. This finding is in agreement with the results presented by Laklai *et al.* (2010) that tumor stiffening could be a better indicator of stroma modification than bulk collagen abundance or total collagen proteins, especially when dense fibrosis is a product of both physical and genetic changes.¹⁰ These findings underscore the potential use of elastography in explaining controversial results^{25,26} of anti-stromal therapies.

Despite the complexity and ongoing controversy underlying PDAC ECM remodeling, it is important to recognize that tumor stiffening is a universal physical phenotype to reflect PDAC transformation, with high potential for prognostic imaging or use in assessment of response or lack of response. However, appreciation of the value of the heterogeneity and spatial resolution can only motivate the need for further understanding of how this affects therapeutic delivery and response. Data from **Fig. 4.7** showcases the possibility of exploiting stiffness information as a surrogate for drug penetration. **Fig. 4.7A** illustrates drug distribution and stiffness map from a global view whereas **Fig. 4.7B** displays two samples in which stiffer, collagen-denser region results in lower drug uptake and limited patent vessel area. **Fig. 4.7C** demonstrates the linear relationship between drug uptake and stiffness measurements in both AsPC-1 and BxPC-3. AsPC-1 tumors have higher BPD fluorescence intensity which aligns with information

showed in **Fig. 4.7B** that on average AsPC-1 tumors are softer. The exponential fit between patent vessel area and regional stiffness corroborates the idea that growth-induced solid stress compresses blood vessels and CAF-depleted tumors had larger vessel diameters.²⁷ Considering it is widely accepted that functional blood vessels play a vital role in solid tumor interstitial transport, elastography imaging with an attempt to study the effect of tumor biology on drug transport should achieve a spatial resolution matching the capillary spacing, or hundreds of microns. Only then, tumor mechanics information will truly reflect biological changes with respect to transport efficiency.

This study has three main limitations. With pancreatic xenograft models implanting AsPC-1 and BxPC-3, the immunodeficient mice may not fully recapitulate the immune response promised by genetically-engineered mouse models.²⁸ For the purpose of demonstrating the potential of high-resolution elastography information in studying PDAC tumor microenvironment, current orthotopic xenograft models have proven to be adequate. It is necessary to acknowledge the mismatch between fresh and fixed tissue geometries, which compromises the accuracy of the image co-registration process. Inserting metal pins significantly facilitate this process of providing fiducial markers, to allow alignment and reasonable spatial match for this study. Furthermore, improved image co-registration process could allow for analysis of whole-tumor with ideal spatial resolution of hundreds of microns. Another limitation comes from the edge effect of slicing the tumor embedded in gel and tissue stress relaxation, both of which result in tissue deformation. The stiffness values obtained from the tumor boundary would take into account the soft gel beneath therefore reported YM would be lower than actual values at these locations. However,

tumor stiffness heterogeneity across the tumor area is an apparent observation despite peritumoral errors.

4.5 Conclusion

This study has demonstrated that with higher quality of elastographic imaging, stiffness information and its heterogeneity provide more spatial detail into how tumor mechanics could reflect changes in tumor biology and phenotypes. However, the fact that the spatial resolution required to allow biologically meaningful and accurate imaging is higher than what can be achieved with any diagnostic method suggests that further improvements in imaging tools must be developed before this can become a routine tool. The images in this work provide the core rationale for developing diagnostic imaging systems that might capture this level of spatial information in a non-invasive manner. Additionally, this existing system can be used as an *ex vivo* assay of response to anti-stromal therapies or acute invasive treatments such as irreversible electroporation²⁹ or photodynamic therapy.³⁰

4.6 Acknowledgements

This work was funded by NIH grant P01CA084203. The authors acknowledge the NCCC light microscopy shared resource (IPIM) supported in part by NCI Cancer Center Support Grant 5P30 CA023108-37.

4.7 References

1. Chauhan, V. P., Stylianopoulos, T., Boucher, Y. & Jain, R. K. Delivery of Molecular and Nanoscale Medicine to Tumors: Transport Barriers and Strategies. *Annu. Rev. Chem. Biomol. Eng.* **2**, 281–298 (2011).
2. Valsecchi, M. E., Díaz-Cantón, E., de la Vega, M. & Littman, S. J. Recent treatment

- advances and novel therapies in pancreas cancer: a review. *J. Gastrointest. Cancer* **45**, 190–201 (2014).
3. Adamska, A., Domenichini, A. & Falasca, M. Pancreatic Ductal Adenocarcinoma: Current and Evolving Therapies. *Int. J. Mol. Sci.* **18**, (2017).
 4. O’Neil, B. H. *et al.* A phase II/III randomized study to compare the efficacy and safety of rigosertib plus gemcitabine versus gemcitabine alone in patients with previously untreated metastatic pancreatic cancer. *Ann. Oncol. Off. J. Eur. Soc. Med. Oncol.* **26**, 1923–9 (2015).
 5. Fountzilias, G. *et al.* Gemcitabine Combined with Gefitinib in Patients with Inoperable or Metastatic Pancreatic Cancer: A Phase II Study of the Hellenic Cooperative Oncology Group with Biomarker Evaluation. *Cancer Invest.* **26**, 784–793 (2008).
 6. De Jesus-Acosta, A. *et al.* A phase II study of the gamma secretase inhibitor RO4929097 in patients with previously treated metastatic pancreatic adenocarcinoma. *Invest. New Drugs* **32**, 739–745 (2014).
 7. Jain, R. K., Martin, J. D. & Stylianopoulos, T. The role of mechanical forces in tumor growth and therapy. *Annu. Rev. Biomed. Eng.* **16**, 321–46 (2014).
 8. Padera, T. P. *et al.* Pathology: cancer cells compress intratumour vessels. *Nature* **427**, 695 (2004).
 9. Chauhan, V. P. *et al.* Angiotensin inhibition enhances drug delivery and potentiates chemotherapy by decompressing tumour blood vessels. *Nat. Commun.* **4**, 2516 (2013).
 10. Laklai, H. *et al.* Genotype tunes pancreatic ductal adenocarcinoma tissue tension to induce matricellular fibrosis and tumor progression. *Nat. Med.* **22**, 497–505 (2016).
 11. Harada, N. *et al.* Preoperative Pancreatic Stiffness by Real-time Tissue Elastography to Predict Pancreatic Fistula After Pancreaticoduodenectomy. *Anticancer Res.* **37**, 1909–1915 (2017).
 12. Fang, Q. *et al.* Ultrahigh-resolution optical coherence elastography through a micro-endoscope: towards in vivo imaging of cellular-scale mechanics. *Biomed. Opt. Express* **8**, 5127–5138 (2017).
 13. Wang, H. *et al.* Elastographic Assessment of Xenograft Pancreatic Tumors. *Ultrasound Med. Biol.* **43**, 2891–2903 (2017).
 14. Wang, H. *et al.* Elastography can map the local inverse relationship between shear modulus and drug delivery within the pancreatic ductal adenocarcinoma

- microenvironment. *Clin. Cancer Res.* clincanres.2684.2018 (2018).
doi:10.1158/1078-0432.CCR-18-2684
15. Wang, S. & Larin, K. V. Optical coherence elastography for tissue characterization: a review. *J. Biophotonics* **8**, 279–302 (2015).
 16. Nieskoski, M. D. *et al.* Collagen Complexity Spatially Defines Microregions of Total Tissue Pressure in Pancreatic Cancer. *Sci. Rep.* **7**, 10093 (2017).
 17. Leonardi, A. D. C., Bir, C. A., Ritzel, D. V & VandeVord, P. J. Intracranial pressure increases during exposure to a shock wave. *J. Neurotrauma* **28**, 85–94 (2011).
 18. Pinet, E., Pham, A. & Rioux, S. Miniature fiber optic pressure sensor for medical applications: an opportunity for intra-aortic balloon pumping (IABP) therapy. in **5855**, 234 (International Society for Optics and Photonics, 2005).
 19. Kolipaka, A., Araoz, P. A., McGee, K. P., Manduca, A. & Ehman, R. L. Magnetic resonance elastography as a method for the assessment of effective myocardial stiffness throughout the cardiac cycle. *Magn. Reson. Med.* **64**, 862–870 (2010).
 20. Laughney, A. M. *et al.* Scatter spectroscopic imaging distinguishes between breast pathologies in tissues relevant to surgical margin assessment. *Clin. Cancer Res.* **18**, 6315–25 (2012).
 21. Yu, X. *et al.* Needle-shaped ultrathin piezoelectric microsystem for guided tissue targeting via mechanical sensing. *Nat. Biomed. Eng.* **2**, 165–172 (2018).
 22. Rice, A. J. *et al.* Matrix stiffness induces epithelial–mesenchymal transition and promotes chemoresistance in pancreatic cancer cells. *Oncogenesis* **6**, e352–e352 (2017).
 23. HARADA, N. *et al.* *Anticancer research*. ([Potamitis Press], 1981).
 24. Alvarez, R. *et al.* Stromal disrupting effects of nab-paclitaxel in pancreatic cancer. *Br. J. Cancer* **109**, 926–33 (2013).
 25. Rhim, A. D. *et al.* Stromal Elements Act to Restrain, Rather Than Support, Pancreatic Ductal Adenocarcinoma. *Cancer Cell* **25**, 735–747 (2014).
 26. Özdemir, B. C. *et al.* Depletion of carcinoma-associated fibroblasts and fibrosis induces immunosuppression and accelerates pancreas cancer with reduced survival. *Cancer Cell* **25**, 719–34 (2014).
 27. Stylianopoulos, T. *et al.* Causes, consequences, and remedies for growth-induced solid stress in murine and human tumors. *Proc. Natl. Acad. Sci. U. S. A.* **109**, 15101–8 (2012).

28. Krempley, B. D. & Yu, K. H. Preclinical models of pancreatic ductal adenocarcinoma. *Chinese Clin. Oncol.* **6**, 25–25 (2017).
29. Martin, R. C. G., McFarland, K., Ellis, S. & Velanovich, V. Irreversible Electroporation Therapy in the Management of Locally Advanced Pancreatic Adenocarcinoma. *J. Am. Coll. Surg.* **215**, 361–369 (2012).
30. Huggett, M. T. *et al.* Phase I/II study of verteporfin photodynamic therapy in locally advanced pancreatic cancer. *Br. J. Cancer* **110**, 1698–1704 (2014).

Chapter 5: Imaging Tumor Collagen from Fresh Tissue

This chapter is derived from:

P. Vincent, et al., “Visualization and quantification of pancreatic tumor stroma in fresh tissue via ultraviolet surface excitation.” *J Biomed Opt.* 2021 Jan;26(1):016002. doi: 10.1117/1.JBO.26.1.016002

5.1 Introduction

The microenvironment of pancreatic adenocarcinoma (PDAC) is well recognized as a highly complex cellular-molecular-stromal milieu that hinders therapeutic response.^{1,2} The hyperdense desmoplastic nature of PDAC has been associated with drug resistant³ cancer progression,⁴ prompting a major direction of targeted therapies focusing on stromal depletion.⁵ However, attempts to alleviate the effects of dense stroma have yielded mixed results,^{6,7} and it may be that systemic molecular therapies may not be the ideal way to deal with the type of desmoplasia in PDAC. While major mechanistic efforts have elucidated the pathobiological relationship of pancreatic stellate cells with other tumor microenvironment components,^{8,9} recent findings have called for more attention towards the spatial orientation of particular biomarkers such as immune cells¹⁰ and fibroblasts.¹¹ The study of these components and contributors to the desmoplasia is challenging to examine because of how dynamic the microenvironment is and how hard it is to examine molecular signals and morphology in fresh tissues. In this study, a methodology to image and quantify stroma and some molecular signals in fresh PDAC is examined.

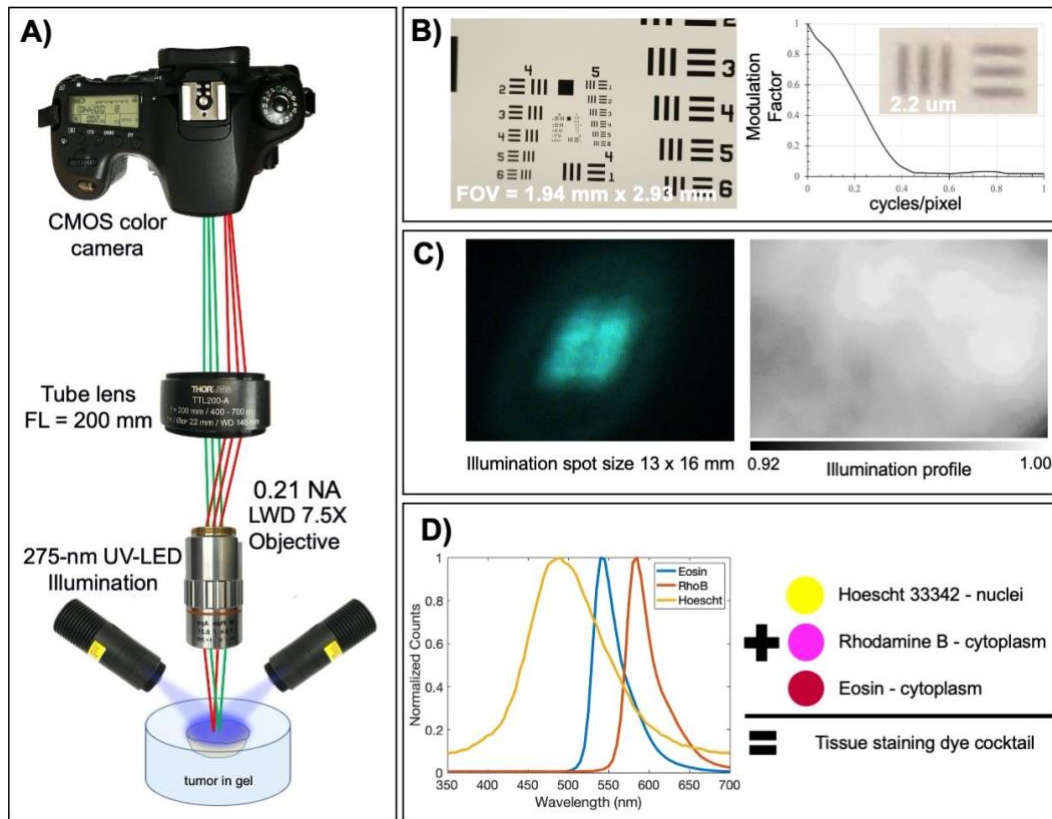
Existing approaches to retrieve quantitative stromal information include traditional histology, immunofluorescence staining,¹² and optical imaging methods such as second harmonic¹³ or birefringence imaging.¹⁴ These techniques are subject to extensive sample

preparation and/or limited specimen size, which inhibits the capability of capturing whole tissue heterogeneity. Fortunately, advancements in fresh tissue optical imaging have shown how it is possible to image intact whole specimens while mapping at the microscopic level. Microscopy with ultraviolet surface excitation (MUSE) developed by Fereidouni et al exploits UV excitation at wavelengths shorter than 300 nm to provide image contrast when imaging bulk tissues with just thin slice excitation at the surface.¹⁵ In MUSE, exogenous stains excited at 280-nm illumination are applied to highlight different tissue components as well as to overcome intrinsic autofluorescence, all of which utilizes a very simple and cost-effective optical design. While it was reported that stromal components have not yet been well-studied using this imaging technique,¹⁵ its potential capability of imaging stroma directly from fresh tissue provides an ideal tool for studying the tumor microenvironment heterogeneity, and changes to this from response to targeted therapies.

Therefore, this study developed the capability to use UV-fluorescence imaging in stromal imaging from fresh tissue of PDAC tumors, which yields strong collagen signals. The work examined BxPC-3, a human-derived tumor cell line orthotopically implanted in xenograft mouse models for analysis of the stromal network of PDAC. Previous studies have confirmed the micro-heterogeneity of collagen in this tumor type, and that the collagen density is strongly correlated to the tumor biomechanical stiffness and inversely with vascular perfusion.^{16,17} The current study examined if equivalent collagen information could also be visualized and quantified directly from fresh tissue imaging as compared to traditional pathology stained fixed tissues. Furthermore, assessment of viable tumor cells and necrotic areas was examined in the same setting from UV-fluorescence signal of Hoechst staining. If successful, this technique could provide a fast assay platform for in

situ investigation of therapeutic effects from interventional targeted therapies in a way that does not require pathology processing and post imaging registration. One of our primary goals was to use this tool as an assay of PDAC reaction to photodynamic therapy^{18,19} to examine the subtle changes that can occur with sub-lethal photodynamic therapy, sometimes referred to as “photodynamic priming” for adjuvant therapies.²⁰

5.2 Materials and Methods



Figurer 5.1 UV-fluorescence imaging system setup. *A)* A schematic of the imaging system with camera tube lens and either 7.5X or 10X objective lens. Illumination sources were 2 UV-LEDs mounted symmetrically. *B)* The imaging field of view and spatial resolution test are shown. *C)* The illumination spot size generated by the UV-LEDs is shown with irradiance 10 mW/mm². *D)* Emission spectra of UV-excited staining dyes when illuminated at 275-nm covered the detection range of the RGB camera.

5.2.1 Infinity-corrected Imaging Setup

The system utilized the simplicity of infinity-corrected optics and the versatility of a commercial RGB camera (**Fig. 5.1A**). Fluorescence signals were focused by a long working distance objective (Mitutoyo, Kawasaki, Japan) onto a 200-mm tube lens (#TTL-200A, Thorlabs, USA) which were captured by a commercial Electro-Optical System (EOS) color camera (EOS 60D, Canon, Japan). Camera settings were initialized by the native EOS Utility, including exposure time, ISO levels and image output format. The objective was able to fill up the Advanced Photo System type-C (APS-C) sensor size of the camera, given a field of view of approximately 1.94 x 2.93 mm. The imaging system was able to resolve Group 7 Element 6 on the USAF 1951 resolution target. The modulation transfer function (MTF) was computed, and resolution was found to be 0.5 μm at 10% contrast (**Fig. 5.1B**). Raw image data was obtained by LabVIEW software readout and control.

5.2.2 Ultraviolet Illumination Source

Open-faced, dark-field illumination was exploited using two 275nm UV-LEDs (#M275L4, Thorlabs, USA) mounted symmetrically to provide a more uniform light distribution. The LED emission was collimated by a 20-mm fused silica ball lens to provide an irradiance of 10 mW/mm^2 , covering an area of approximately 13 x 16 mm (**Fig. 5.1C**). The LED drivers (#LEDD1B, Thorlabs, USA) provided a current of 700mA to each LED as well as a trigger signal for hardware synchronization. The LEDs functioned in trigger mode to minimize photobleaching and ensure temperature control. The short 50- μs LED rise time as compared to 50-ms exposure time in addition to a couple seconds of moving

the translational table to a new spatial location provided adequate “off” time for the LEDs to avoid heating and any significant spectral changes.

5.2.3 Animal Models and Tumor Sample Preparation

All animal procedures were conducted under the protocol approved by the Dartmouth Institutional Animal Care and Use Committee (IACUC). A total of 5 athymic nude mice between the age of 6-8 weeks were used in this study. They were injected with human tumor cell line BxPC-3 (ATCC, Cat# CRL-1687). The pancreas was exposed, and tumor cells were injected with a 1:1 ratio of Matrigel. BxPC-3 required 5-7 weeks for tumors to reach ideal imaging size of 1cm in diameter. The mice were on purified diet to reduce autofluorescence from chlorophyll-based food consumption. After the tumors reached imaging size, the mice were anesthetized and sacrificed. Dextran Texas Red (Thermo Fisher Scientific, Cat# D1864) was intravenously injected 1-hour before sacrifice to demonstrate the capability of perfusion imaging using the same imaging setup. Tumors were resected, embedded in 2.5% agar and sliced in half. A layer of PBS was applied on the tumor surface to maintain proper hydration.

5.2.4 Photodynamic Treatment

Two out of five mice were injected with 0.5 mg/kg Visudyne photosensitizer (one hour before Photodynamic therapy (PDT) treatment with 690-nm laser at a dose of 75 J/cm² and irradiance of 100 mW/cm². The light was given by a fiber optic cable at the exposed tumor site. The mice were sacrificed two days after the treatment.

5.2.5 Tumor Staining

Conventional pathological fluorophores such as Hoechst 33342, Eosin and Rhodamine B (Sigma) were used as exogeneous stains on fresh and fixed tissue samples.

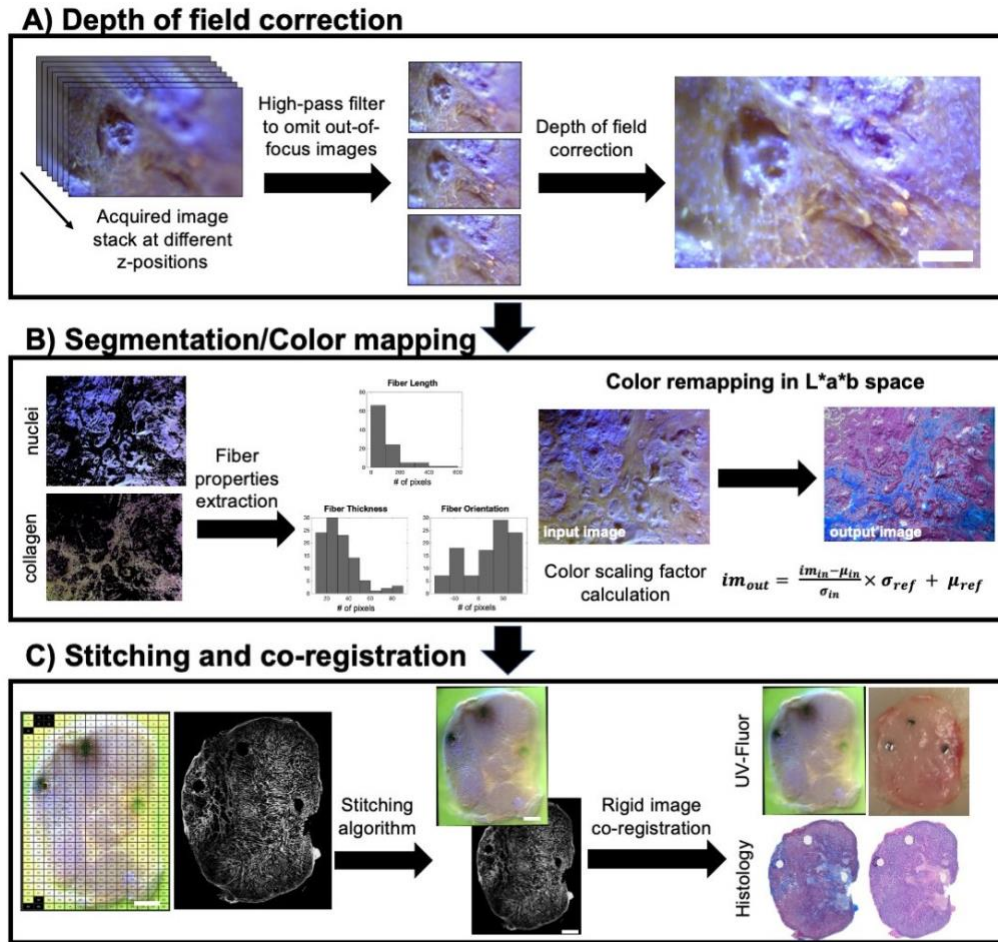


Figure 5.2 Schematic of primary image processing steps. *A)* At each location, an image stack was acquired by moving tissue samples on a motorized translation stage. High-pass filtering was applied to reduce out of focus information. Depth of field correction was then applied. Scale bar = 100 μ m. *B)* Nuclei and collagen were identified by color segmentation in HSV space. Fiber analysis was done on segmented collagen to yield information such as fiber length, thickness, orientation and crosslinking profile. UV-fluorescence images were also color-map transferred to mimic the color palette of Masson's Trichrome staining (blue collagen, dark purple nuclei and light pink cytoplasm). The color remapping process was executed in L*a*b space, utilizing the mean and standard deviation of each channel to create a color scaling factor. *C)* Image stitching was performed with 10% overlap to create a whole-tumor view. Rigid image co-registration was performed on the whole-tumor size UV-fluor images, histology images and brightfield photos of freshly resected tumors to facilitate comparison across imaging modalities. Scale bar = 2 mm.

These fluorophores could be excited by a deep UV illumination to highlight tissue

morphology (**Fig. 5.1D**). In this study, a combination of Hoechst 33342 (0.5 mg/mL in PBS), Eosin (1 mg/mL in PBS) and Rhodamine (0.2 mg/mL in PBS) was adequate for PDAC stromal imaging. The tissue sample was submerged in this dye combination for 30 seconds then washed off by PBS for a minute.

5.2.6 Image Acquisition, Depth of Field Correction and Stitching

Image acquisition was automated by LabVIEW to allow for synchronization of illumination sources, camera shutter and a motorized 3-dimensional stage. At each x-y coordinate, a series of images taken at seven 6.3- μm vertical increments provided an image stack for DOF correction (**Fig. 5.2A**). While 6.3- μm step size was the limit of our current vertical stage, smaller vertical step-size and more acquisitions for each location would result in higher image quality. Due to the high stiffness nature of PDAC tumors, tissue surface irregularity became a significant issue. Therefore, optical sectioning at multiple z-locations was necessary to maximize the number of in-focus pixels. Then, the DOF correction algorithm²¹ written by Aguet et al was executed in MATLAB. Image stitching was implemented by Microsoft Image Composite Editor software with 10% overlap to produce a whole tissue sample field of view (**Fig. 5.2C**). After imaging, the tumors were formalin fixed and prepared for staining with Masson's Trichrome to visualize collagen and Hematoxylin and Eosin to verify necrosis areas, which was essential for tumors that were treated with photodynamic therapy to evaluate treatment effects. Both the UV-fluorescence data and the Masson's Trichrome data acquired for collagen analysis were imaged with a 10x magnification lens.

5.2.7 Tumor Parameter Identification

Structural segmentation

Color segmentation in HSV space was used to distinguish nuclei and collagen (**Fig. 5.2B**). Image data was histogram stretched, then segmented in MATLAB. Hue (h), saturation (s) and value (v) cutoffs for purple nuclei were ($0.449 < h < 0.770$, $0 < s < 1$, $0.656 < v < 1$) and for green collagen ($h > 0.750$ or $h < 0.464$, $0 < s < 1$, $0.341 < v < 1$). Vacuoles which appear as round black holes in UV-fluorescence data were also segmented ($h > 0.773$ or $h < 0.113$, $0.475 < s < 1$, $0 < v < 0.477$). The distinctive color cutoffs produced no overlays between structures. Any segmented regions which contained fewer than 200 pixels were considered part of the cytoplasm since their sizes were considerably smaller than a nucleus, a collagen fiber or a vacuole. These criteria for classifying structures in the HSV space were exclusively selected for pancreatic tumor samples, thus further modifications should be considered for other tissue structures.

Collagen analysis

Collagen analysis was performed in Matlab. The binary mask of segmented collagen in the previous step was refined prior to collagen analysis. In cases in which nuclei were positioned on top of a collagen, their superficial position severely interfered with skeletonization and crosslinking analysis, therefore they needed to be removed initially by using function *bwareaopen.m* to perform hole removal on the collagen binary mask. After that, collagen thickness map was computed using the function *bwdist.m*, which calculates the distance of all positive pixels to their nearest background pixel (**Fig. 5.3A**). Thresholding was applied to the UV-fluor collagen thickness map for two purposes: 1) to eliminate small collagen areas that were the cross-sections of long strands due to the orientation of tissue cuts and 2) to reduce the blur effect due to out of focus pixels that

could inaccurately clump the nearby strands together. After these refinements,

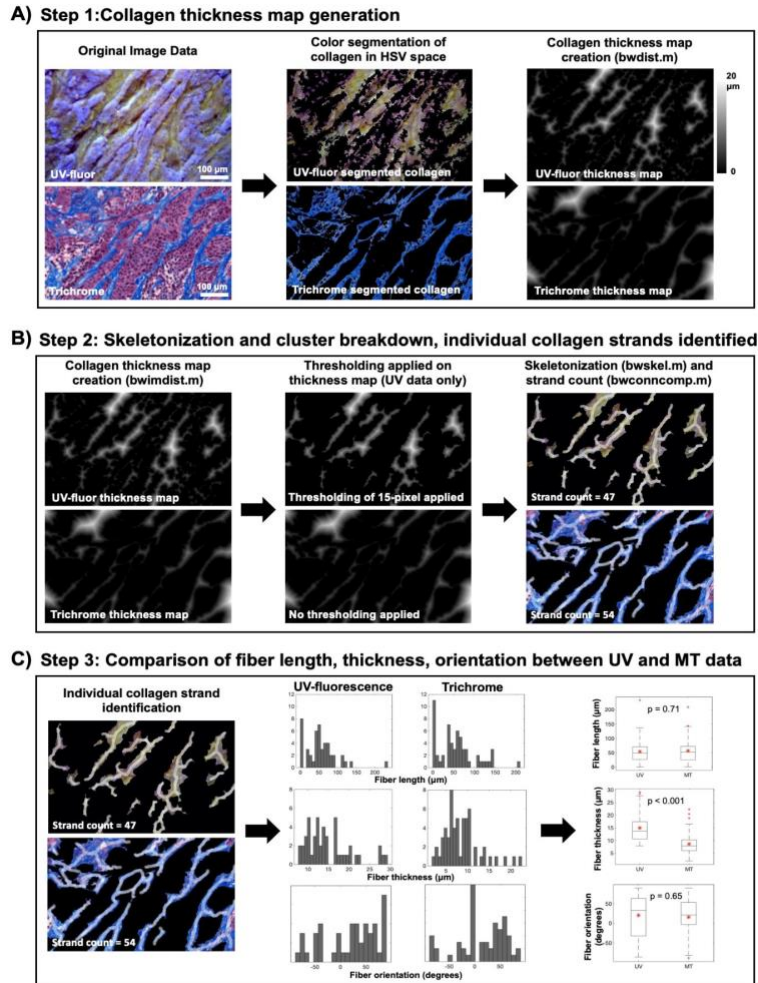


Figure 5.3 Demonstration of collagen segmentation and quantification methods for UV-fluor data with validation testing on Trichrome data, summarized in 3 main steps. A) Step 1 generated collagen thickness maps using the matlab function `bwdist.m` performed on segmented collagen in HSV space. B) Step 2 resulted in skeletonized maps of collagen in combination with thickness maps. Necessary refinements on UV-fluor data were highlighted. A thresholding value was applied on the UV-fluor collagen thickness map to eliminate inaccurate connections of clusters and small cross-sections of collagen due to tissue cut orientation. Skeletonization using `bwskel.m` and cluster breakdown using `bwconncomp.m` yielded individual collagen strands. C) Fiber analysis in Step 3 was performed on each collagen strand to measure the length, thickness and orientation. Statistical analysis to compare fiber analysis between UV-fluor and Trichrome data was conducted to validate the feasibility of using UV-fluor imaging data to obtain quantified collagen information.

skeletonization was performed on the collagen thickness map using *bwskel.m*. Intersections of collagen strands were identified using ‘branchpoints’ operation with *bwmorph.m*, and these intersection points were used to break down the collagen network into separate individual strands (**Fig. 5.3B**). For each collagen strand, average fiber thickness was determined by twice the average distances of all pixels of the skeletonized centerline to their nearest background pixel. Calling *regionprops.m* with relevant measurement properties provided analysis for fiber count, length and orientation (**Fig. 5.3C**). The whole algorithm was applied to Masson’s Trichrome (MT) data as validation testing to ensure accurate fiber analysis on UV-fluorescence (UV-fluor) data. Manual segmentation and quantification of fibers were performed on a panel of 10 test images for both UV-fluor and MT image sets, which were chosen to cover a wide range of collagen fiber lengths, thicknesses and orientations. After the algorithm was validated, auto-segmentation was performed with manual checking of key intermediate results such as the collagen thickness maps and skeletonized maps, for all ROIs reported in the Results section.

5.2.8 Color Remapping

After structural segmentation described in the previous the step, color remapping was implemented to adjust from UV-fluorescence color palette to a more conventional color scheme of Masson’s Trichrome staining. The color transfer process described in Reinhard et al²² was executed in Matlab. Image data was converted to L*a*b space (L for lightness, ‘a’ for red to green color values and ‘b’ for yellow to blue color values). For each structure (collagen, nuclei or cytoplasm), the mean and the standard deviation of each color channel were computed to create a scaling factor between the UV-fluorescence and the MT data sets (**Fig. 5.2B**). Output images resembled the color scheme from MT staining.

5.2.9 Statistical Analysis

A two-sample student's t-test was employed in Matlab without the assumption of equal variances between the tested samples to determine the difference in means using a two-tailed analysis and $\alpha = 0.05$.

5.3 Results

5.3.1 Stromal Content of Fresh PDAC Tumors can be Visualized Microscopically and Macroscopically Using UV-fluorescence Imaging

Fig. 5.4A illustrates the contrast enhancement of illuminating samples at below 300 nm. For the same tissue specimen, 275-nm excitation reveals morphological features that are undetectable at 340-nm excitation. Collagen strands in yellow-green color at both peritumoral and intratumoral regions are observable, suggesting that UV-fluorescence imaging is capable of detecting thin collagen strands with diameters down to 5 μm . Since image acquisition required optical sectioning of the specimens at different depth, the data after being depth of field corrected also yielded semi-3D morphology (**Fig. 5.4B**). Structural components such as blood vessels, collagen crosslinking and collagen bundling can also be visualized with this imaging technique. Due to rapid imaging, a translation stage coupled with the imaging system could produce whole-specimen images with microscopic resolution. The stitching algorithm provides macroscopic image data, from which regions of necrosis could be easily identified as observed in **Fig. 5.4C**. The light yellow/orange regions in the UV-fluorescence images are well-aligned with regions of necrosis inferred from H&E staining. A closed-up look at the images revealed collagen content in the tumors, as illustrated in **Fig. 5.4D**. Side-by-side comparison of UV-fluorescence data and corresponding Masson's Trichrome staining from the same

specimens shows great agreement of where tumor collagen is located and the complexity of collagen network.

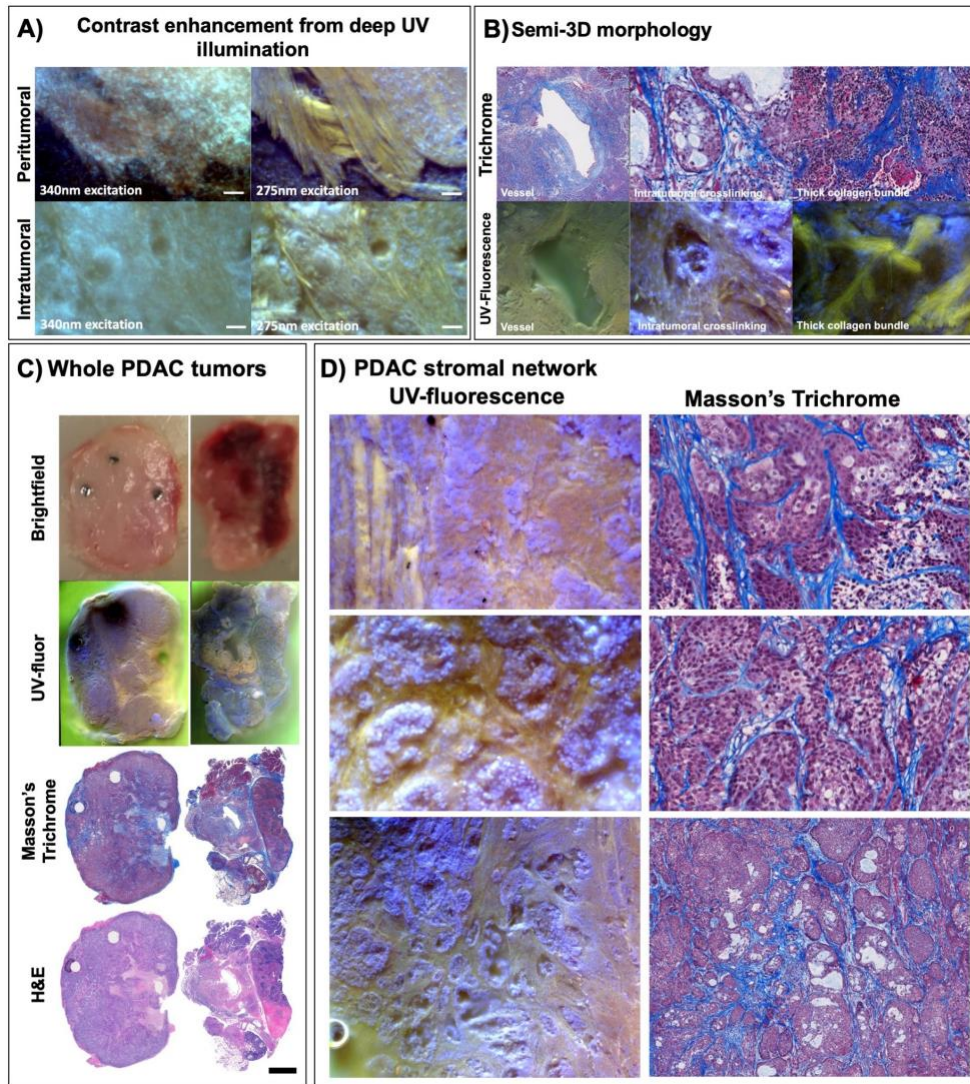


Figure 5.4 UV-fluorescence imaging is capable of capturing stromal content in PDAC tumors. **A)** Deep UV-illumination below 300 nm provides excellent image contrast, revealing morphology at the microscopic level. Collagen content from peritumoral and intratumoral regions are illustrated, scale bar = 100 μ m. **B)** Optical sectioning and depth of field correction provides semi-3D depth information, which highlights 3D structures such as vessel, collagen crosslinking and bundling. **C)** Rapid imaging allows tumor visualization at macroscopic level, scale bar = 2 mm. **D)** Demonstration of strong yellow-green collagen signal was obtained from an RGB camera of fresh tissue imaging, and this is compared to Masson's Trichrome staining data.

5.3.2 UV-fluorescence Image Data with a 3-dye Staining Technique can Mimic Masson's Trichrome Staining

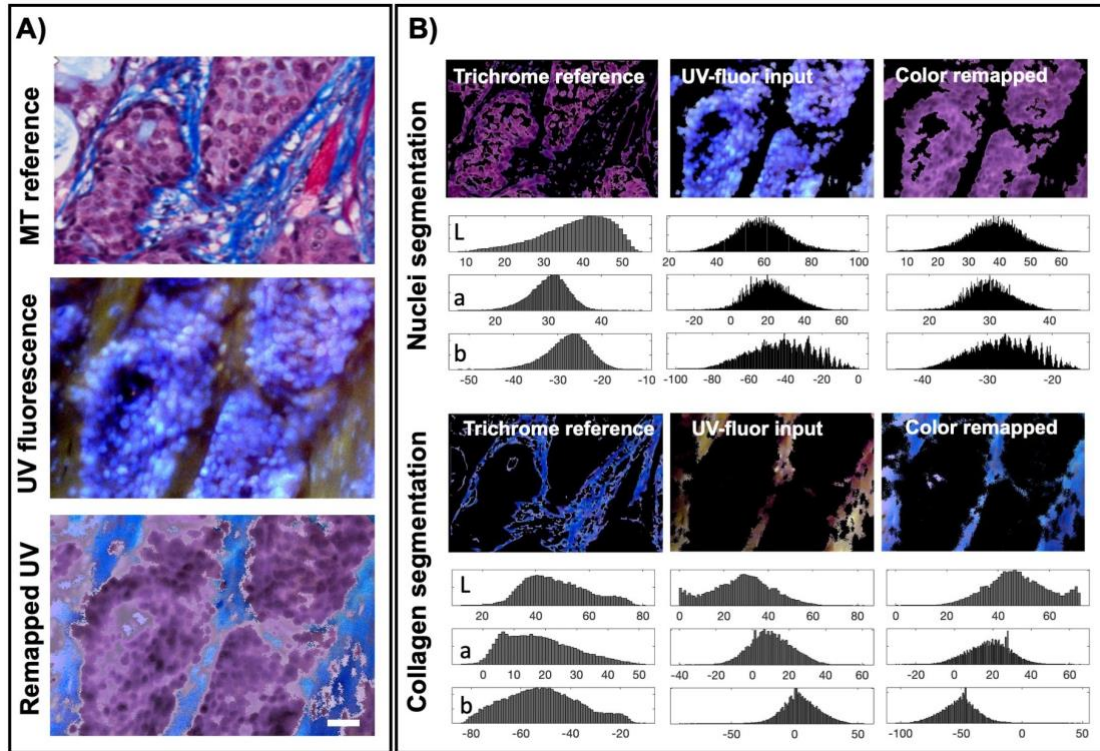


Figure 5.5 Color remapping of UV-fluorescence images allows visualization using Masson's Trichrome staining color scheme. **A)** UV fluorescence image after color remapping showed collagen in blue and nuclei in dark purple, similar to Masson's Trichrome staining results, scale bar = 30 μm . **B)** Illustration of color remapping in L^*a^*b color space, based on structural segmentation. Corresponding histograms of reference, input and output images show that the distribution of color intensities and hues was preserved.

Image data acquired by UV-fluorescence imaging shows that collagen network and viable tumor cells are distinct from each other, due to different emission peaks of Hoechst 33342 and Eosin. **Fig. 5.5A** highlights the feasibility of converting UV-fluorescence data into Masson's Trichrome equivalent color scheme, i.e. collagen as blue, nuclei as dark purple and cytoplasm as light pink. In **Fig. 5.5B**, color remapping process was described for each main structure, i.e. collagen and nuclei. The "L" channels for those structures were

inverted to reflect the color intensity inversion, so the bright purple nuclei in the original UV-fluorescence data appear dark just as depicted in MT staining. As for collagen, all of the channels were flipped to reflect not just the inversion in intensity, but also the hues to truly reflect the color transition in MT staining. The histograms of each channel (L, a and b) in the L*a*b color space show that the distribution of intensity and hue information was preserved after the remapping process.

5.3.3 Classification of Stroma in PDAC Tumors is Feasible in Fresh Tissue via UV-fluorescence Imaging

Heterogeneity of collagen formation in PDAC tumors was captured and classified in **Fig. 5.6**. Collagen fiber visualization general agreement between UV-fluorescence and Trichrome data was visualized in **Fig. 5.6A**. Exact matching between two data sets was not expected due to tissue deformation and tissue changes due to pathology staining process to create trichrome-stained samples. However, direct comparison of the same tissue regions confirms the capability of UV-fluorescence imaging to visualize collagen in ex vivo samples. Quantification of the fluorescence signals also shows a strong agreement with results obtained from trichrome data. **Fig. 5.6B** illustrates the outputs of the fiber strand analysis based on fiber thickness maps for both data sets.

The same algorithm was showed to work well for both. The distribution of collagen fibers in terms of length, thickness and orientation was displayed in **Fig. 5.6C** for both data sets to validate the feasibility of extracting quantitative information from UV-fluorescence imaging on fresh tissues. Results from statistical analysis in **Fig. 5.6D** shows that there was not a significant difference in means between the two data sets in terms of collagen content percentage, collagen fiber length and orientation. 20% difference in means ($\mu_{UV} = 18.8\%$

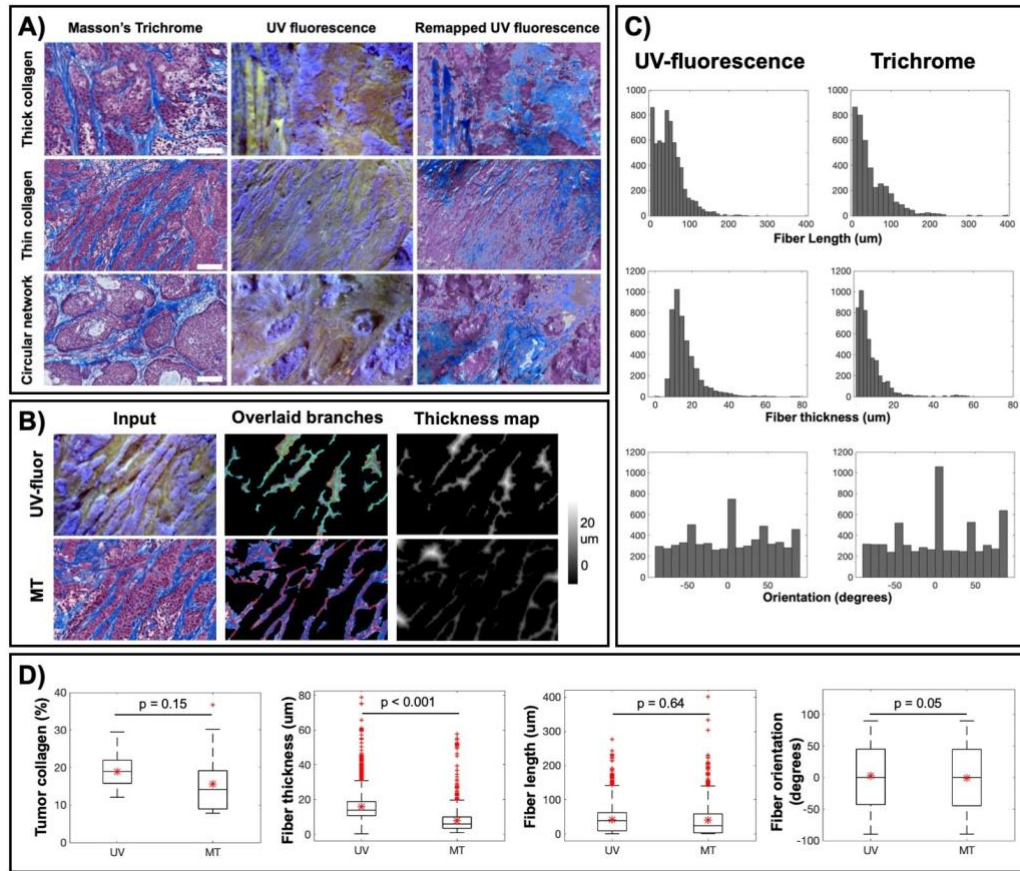


Figure 5.6 Quantification of collagen content in PDAC tumors. *A)* Different types of collagen observed in both Trichrome and UV-fluorescence data sets. *B)* Quantification of collagen fibers. *C)* Distribution of fiber length, fiber thickness and fiber orientation obtained from both data sets *D)* Statistical analysis was performed to show that there is no significant difference in means in terms of tumor collagen content, fiber length and fiber orientation between UV-fluorescence and Trichrome data. However, there was a statistical difference between two data sets for fiber thickness. Mean and standard deviation of UV vs. Trichrome data, respectively, for each category are 18.8 ± 4.2 vs. 15.6 ± 8.1 (collagen content %), 15.9 ± 7.8 vs. 7.9 ± 7.3 (collagen thickness in μm), 48.5 ± 36 vs. 49.3 ± 47 (collagen fiber length in μm), 2.53 ± 51 vs. -0.85 ± 51.3 (collagen fiber orientation in degrees). Data was analyzed for 5 tumors, necrosis areas were excluded, 50 ROIs were randomly selected with ROI size of 0.6×0.4 mm each, total collagen strands from UV data = 6442, from Trichrome data = 6606.

vs. $\mu_{\text{MT}} = 15.6\%$) reported from comparing collagen content data was largely due to the differences in fiber thickness analysis ($\mu_{\text{UV}} = 15.9 \mu\text{m}$ vs. $\mu_{\text{MT}} = 7.9 \mu\text{m}$), which could be

largely attributed to the difficulty of accurate segmentation and separation of fibers from imaging bulk tissue. Another reason for thickness inconsistency was the thresholding applied on the collagen thickness map mentioned in the Methods section. Better image quality with minimized out-of-focus pixels would significantly minimize the inaccuracy from thresholding and close the gap of fiber thickness reported by these two imaging modalities. Total count of collagen strands from both data sets is less than 3% different (6442 strands from UV data and 6606 strands from Trichrome data). Fiber length on average is accurately reported with a discrepancy of less than 2% ($\mu_{UV} = 48.5 \mu\text{m}$ vs. $\mu_{MT} = 49.3 \mu\text{m}$) while orientation shows a difference of 3.4 degrees on average.

5.3.4 UV-fluorescence Imaging could be Utilized as an Assay Platform to Evaluate the Effects of Photodynamic Priming on Collagen Modulation

Fig. 7 showcases additional features of UV-fluorescence imaging in fresh tissues that can be utilized in targeted therapy response assessments. **Fig. 7A** illustrates the capability of imaging perfusion using the same simple imaging optics. Emission from Texas Red (TR) excited by 275-nm illumination was captured by the red channel on the RGB camera. Dextran-perfused samples could then be stained to obtain structural information without interference from TR signals. In **Fig. 7B**, yellow outline was drawn to identify the tissue imaging surface while red outline locates the regions of necrosis due to photodynamic priming effect. This illustration highlights the capability of visualizing necrosis areas in fresh tissues, which normally is hard to delineate in brightfield images therefore in need of pathological confirmation. Furthermore, the capability of imaging collagen in situ demonstrated in this study could be utilized to assess the collagen modulation effect as an outcome of acute photodynamic priming,²³ as reported in Obaid et

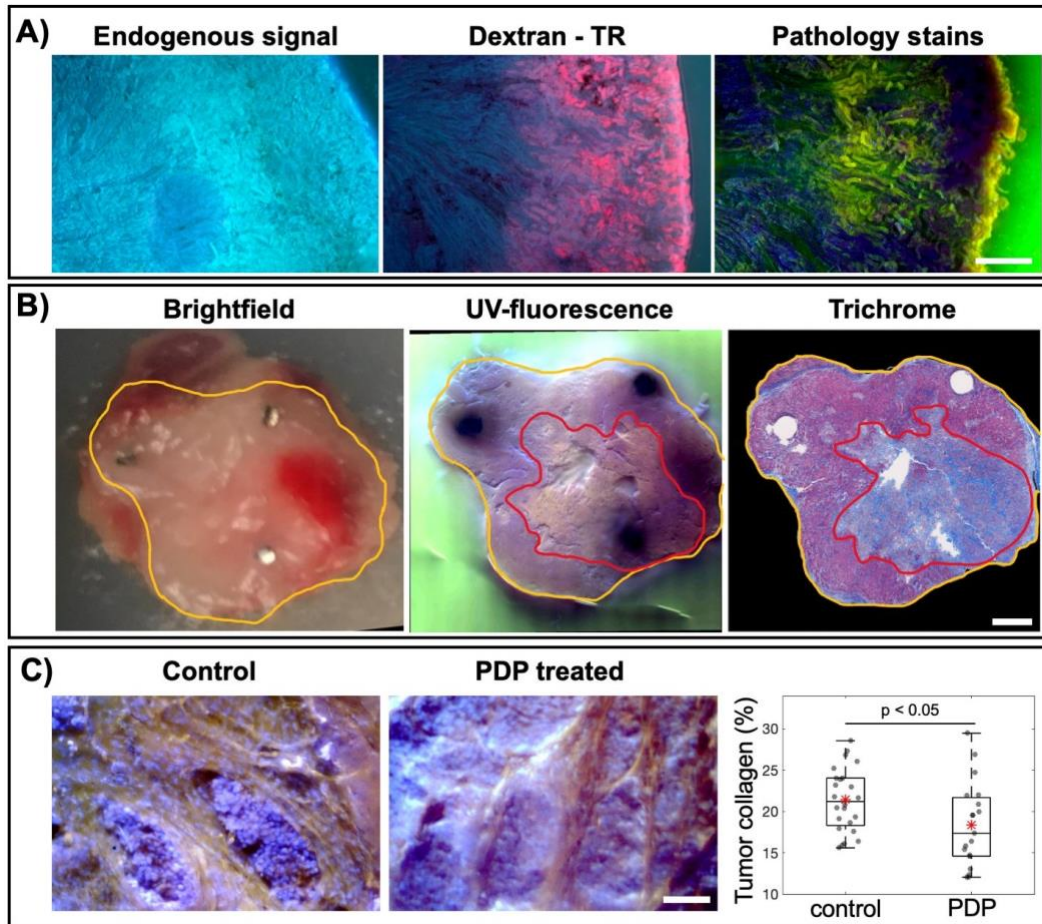


Figure 5.7 *UV-fluorescence imaging as a fresh tissue assay platform to evaluate photodynamic priming responses. A)* Perfusion imaging of dextran tagged with Texas Red in kidney samples. UV-excited Texas Red shows perfused dextran in kidney samples (middle) as compared to endogenous fluorescence without any dextran injection (left). Dextran-perfused tissues could then undergo pathological staining (right) to obtain structural information, scale bar = 500 μm . **B)** Tissue imaging surface was outline in yellow. Necrosis outlined in red is hard to distinguish in brightfield image (left), but observable under UV-fluorescence imaging (middle) which is confirmed by trichrome staining (right), scale bar = 1 mm. **C)** A comparison of collagen content in control and PDP treated tumors. Collagen modulation effect was observed, in which the PDP treated tumors show a 13% reduction in collagen content ($n = 2$ animals per group, control ROIs = 23, treated ROIs = 19), scale bar = 100 μm .

al. Preliminary data acquired by UV-fluorescence imaging has showed possible reduction in desmoplasia for PDAC treated tumors in **Fig. 5.7C**, which suggests that collagen content was reduced by 13%.

5.4 Discussion

This study was designed to test the feasibility of using UV-fluorescence imaging to extract quantitative morphological information from fresh PDAC tumors in xenograft models, at both microscopic and macroscopic levels. The combination of PDAC tumor's desmoplastic nature, collagen-eosin fluorescence enhancement, and superficial optical sectioning of deep UV illumination have made stromal imaging in fresh tissue feasible. Results from **Fig. 5.4** and **Fig. 5.6** show the high fidelity of imaging PDAC stroma using this technique, with quantitative information comparable to Masson's Trichrome staining data. Collagen fibers were found to be in the range of 5-30 μm thickness, with the majority of lengths to be under 50 μm and organized in a chaotic orientation. This is the first time that PDAC tumor stroma was visualized and quantified directly from fresh tissues under UV excitation light. Microscopy with UV surface excitation has been used on a variety of tissues and organs to demonstrate its capability of replacing H&E staining,^{24,25} however, stromal signals have not been a major focus. PDAC tumors have inherent desmoplasia, often consisting of thickened, heavily cross-linked collagen fibers. This abnormally high content of stroma and its direct, well-established relationship to progression and drug transport resistance makes this study particularly useful to assess the responsiveness of PDAC tumors to experimental therapies. Image data to showcase fresh collagen imaging from BxPC-3 tumors in this study suggests that future directions to study other pancreatic tumor types would be beneficial. It has been observed from other pancreatic tumor studies that the collagen fiber shape varies with different tumor types. One of our previous studies showed that more pronounced stiffness heterogeneity was linked to tumors with thicker collagen strands, which inversely affects drug perfusion¹⁷.

Studies since the 1960s have observed the enhancement of collagen fluorescence especially when introduced to Eosin staining,²⁶ and there are many speculations on the mechanism of why collagen signals are enhanced by Eosin. Despite the lack of a clear mechanism, the fact that Eosin is excited by deep UV and produces strong emission has been part of the realization that imaging collagen in fresh tissue would be possible without fixation. Our empirical results show that while Rhodamine helped stain the cytoplasm, Eosin enhanced the collagen fluorescence in PDAC tumors. This approach provides a very flexible and cost-effective tool for thin section imaging of surface exposed tissues, instead of relying solely on collagen autofluorescence. Perhaps the most important factor in this is that this approach provides high resolution images, that can be achieved without fixation or thin section cutting, nor any post imaging registration of the images for analysis. This study also demonstrated color transfer with the goal of remapping UV-fluorescence to a conventional color scheme like Masson's Trichrome. While UV-fluorescence imaging intrinsically acquire data at a larger axial thickness as compared to Masson's Trichrome, better image quality especially in image contrast will help improve fiber segmentation and collagen strand analysis so that errors in fiber thickness could be reduced. Future studies will involve improvements in these aspects.

The potential of imaging collagen using UV-fluorescence is even more prominent due to the capability of wide-field imaging to capture whole-specimen field of view. Due to the highly irregular tissue surface, collagen visualization with this technique does not provide the same image contrast as would be expected from other collagen imaging methods such as second harmonic imaging. However, the short exposure time (50ms per frame) allows image acquisition of whole specimen within minutes. Wide-field imaging at

microscopic resolution of tumor cells and collagen content offer an efficient tool for assessment of macroscopic targeted therapy responses, in terms of collagen modulation, tumor necrosis and tumor perfusion. **Fig. 5.7** illustrates additional features of this imaging tool besides stromal identification. Perfusion imaging was demonstrated by intravenously injecting dextran tagged with Texas Red in the mice. Kidney samples in **Fig. 5.7A** showed Texas Red emitted strongly when excited with 275-nm light source. That same tissue sample then could be stained as fresh tissues and/or fixed, sectioned and stained to reveal structural information. The selective staining of nuclei using Hoechst allowed necrosis assessment as displayed in **Fig. 5.7B**. With preliminary data in **Fig. 5.7C** showing possible reduction in desmoplasia due to acute PDP, a future application of this imaging technique aims to evaluate treatment responses of photodynamic priming on PDAC tumors, a targeted therapy that was proven to cause necrosis and modulate collagen,²³ which resulted in better drug delivery.²⁰

5.5 Conclusion

This study has demonstrated that high-resolution wide-field collagen imaging is feasible in fresh PDAC tumor tissues, with the employment of conventional pathology dyes and deep UV-illumination. Collagen quantification obtained from this UV-fluorescence imaging can be as quantitatively useful as data from Masson's Trichrome stained thin sections, but can be taken without the need for fixation, cutting and post processing for registration. Additional features such as perfusion imaging and necrosis assessment make this simple imaging tool an attractive technique to evaluate targeted therapies such as photodynamic therapy.

5.6 Acknowledgments

This work was funded by NIH grant P01 CA084203. The authors acknowledge the NCCC light microscopy shared resource (IPIM) and the Pathology shared resource (PSR) supported in part by NCI Cancer Center Support Grant P30 CA023108. The authors acknowledge very useful discussions with Professors Farzad Fereidouni and Richard Levenson, UC Davis.

5.7 References

1. Neesse, A. *et al.* Stromal biology and therapy in pancreatic cancer. *Gut* **60**, 861–8 (2011).
2. Kota, J., Hancock, J., Kwon, J. & Korc, M. Pancreatic cancer: Stroma and its current and emerging targeted therapies. *Cancer Lett.* **391**, 38–49 (2017).
3. Nissen, N. I., Karsdal, M. & Willumsen, N. Collagens and Cancer associated fibroblasts in the reactive stroma and its relation to Cancer biology. *J. Exp. Clin. Cancer Res.* **38**, 115 (2019).
4. Laklai, H. *et al.* Genotype tunes pancreatic ductal adenocarcinoma tissue tension to induce matricellular fibrosis and tumor progression. *Nat. Med.* **22**, 497–505 (2016).
5. Van Mackelenbergh, M. G. *et al.* Clinical trials targeting the stroma in pancreatic cancer: A systematic review and meta-analysis. *Cancers* **11**, (2019).
6. Rhim, A. D. *et al.* Stromal Elements Act to Restrain, Rather Than Support, Pancreatic Ductal Adenocarcinoma. *Cancer Cell* **25**, 735–747 (2014).
7. Özdemir, B. C. *et al.* Depletion of carcinoma-associated fibroblasts and fibrosis induces immunosuppression and accelerates pancreas cancer with reduced survival. *Cancer Cell* **25**, 719–34 (2014).
8. Apte, M. V. *et al.* Pancreatic cancer: The microenvironment needs attention too! *Pancreatology* **15**, S32–S38 (2015).
9. Xu, Z., Pothula, S. P., Wilson, J. S. & Apte, M. V. Pancreatic cancer and its stroma: A conspiracy theory. *World Journal of Gastroenterology* **20**, 11216–11229 (2014).
10. Li, J. *et al.* Tumor Cell-Intrinsic Factors Underlie Heterogeneity of Immune Cell

- Infiltration and Response to Immunotherapy. *Immunity* **49**, 178-193.e7 (2018).
11. Martins Cavaco, A. C., Dâmaso, S., Casimiro, S. & Luís Costa, &. Collagen biology making inroads into prognosis and treatment of cancer progression and metastasis. doi:10.1007/s10555-020-09888-5
 12. Haeberle, L. *et al.* Stromal heterogeneity in pancreatic cancer and chronic pancreatitis. *Pancreatology* **18**, 536–549 (2018).
 13. Zoumi, A., Yeh, A. & Tromberg, B. J. Imaging cells and extracellular matrix in vivo by using second-harmonic generation and two-photon excited fluorescence. *Proc. Natl. Acad. Sci. U. S. A.* **99**, 11014–9 (2002).
 14. Walther, J. *et al.* Depth-resolved birefringence imaging of collagen fiber organization in the human oral mucosa in vivo. *Biomed. Opt. Express* **10**, 1942 (2019).
 15. Fereidouni, F. *et al.* Microscopy with ultraviolet surface excitation for rapid slide-free histology. *Nat. Biomed. Eng.* **1**, 957–966 (2017).
 16. Wang, H. *et al.* Elastography can map the local inverse relationship between shear modulus and drug delivery within the pancreatic ductal adenocarcinoma microenvironment. *Clin. Cancer Res.* clincanres.2684.2018 (2018). doi:10.1158/1078-0432.CCR-18-2684
 17. Vincent, P. *et al.* High-resolution ex vivo elastography to characterize tumor stromal heterogeneity in situ in pancreatic adenocarcinoma. *IEEE Trans. Biomed. Eng.* 1–1 (2020). doi:10.1109/tbme.2019.2963562
 18. Xie, Q., Jia, L., Liu, Y.-H. & Wei, C.-G. Synergetic anticancer effect of combined gemcitabine and photodynamic therapy on pancreatic cancer in vivo. *World J. Gastroenterol.* **15**, 737 (2009).
 19. Huang, H.-C. *et al.* Photodynamic therapy synergizes with irinotecan to overcome compensatory mechanisms and improve treatment outcomes in pancreatic cancer. *Cancer Res.* **76**, 1066 (2016).
 20. Huang, H.-C. *et al.* Photodynamic Priming Mitigates Chemotherapeutic Selection Pressures and Improves Drug Delivery. *Cancer Res.* **78**, 558–571 (2018).
 21. Aguet, F., Van De Ville, D. & Unser, M. Model-Based 2.5-D Deconvolution for Extended Depth of Field in Brightfield Microscopy. *IEEE Trans. IMAGE Process.* **17**, (2008).
 22. Reinhard, E., Ashikhmin, M., Gooch, B. & Shirley, P. Color transfer between images. *IEEE Comput. Graph. Appl.* **21**, 34–41 (2001).

23. Obaid, G. *et al.* Impacting Pancreatic Cancer Therapy in Heterotypic in Vitro Organoids and in Vivo Tumors with Specificity-Tuned, NIR-Activable Photoimmunonanoconjugates: Towards Conquering Desmoplasia? *Nano Lett.* **19**, 7573–7587 (2019).
24. Xie, W. *et al.* Microscopy with ultraviolet surface excitation for wide-area pathology of breast surgical margins. *J. Biomed. Opt.* **24**, 1 (2019).
25. Yoshitake, T. *et al.* Rapid histopathological imaging of skin and breast cancer surgical specimens using immersion microscopy with ultraviolet surface excitation. *Sci. Rep.* **8**, 1–12 (2018).
26. Goldstein, D. J. *The fluorescence of elastic fibres stained with Eosin and excited by visible light. Histochemical Journal, I (1969)*

Chapter 6: Modifying PDAC Tumor Stroma with Angiotensin II Receptor Blockers to Improve Verteporfin Delivery

This chapter is derived from:

P. Vincent, et al., "Modifying pancreatic tumor stroma with angiotensin II receptor blockers to improve verteporfin delivery." *Proc. SPIE*. (2019) 10860.

<https://doi.org/10.1117/12.2508796>

6.1 Introduction

The nearly constant 5-year survival rate of 7% for pancreatic cancer¹ over the past few decades has called for more active research especially in novel treatment therapies. Besides traditional practice of surgical resection and chemotherapy, targeted therapies have emerged as a promising field. In pancreatic cancer, the tumor microenvironment has become a strong candidate for targeted therapies due to its involvement with systemic drug delivery.² It is well-established that PDAC stroma contains dense fibroblasts.³⁻⁵ This desmoplastic reaction results in an overproduction of extracellular matrix macromolecules such as collagen and hyaluronan. The excess of these macromolecules creates a high solid stress which is hypothesized to collapse nearby vessels, leading to limited drug uptake. Therefore, targeting the tumor microenvironment to reduce the interstitial pressure could improve systemic delivery.

To alleviate the pancreatic stroma reaction, our study focused on inhibiting the production of CAFs by using losartan - an angiotensin II receptor currently in clinical trials for pancreatic cancer⁶. Previous studies have shown the normalizing effect of losartan on tumor vasculature and collagen synthesis inhibition which improved chemotherapy drug

delivery^{7,8}. In this study, losartan was administered to a mouse xenograft model bearing human-derived AsPC-1 pancreatic cell line to evaluate photodynamic therapy treatment efficacy in terms of photosensitizer uptake enhancement. Biological tissue parameters such as collagen content, vascular patency and regional stiffness were obtained at high resolution over a whole tumor section. This set of data allowed analysis on both a large scale of millimeters and smaller scale of hundreds of microns to examine losartan effect on the tumor microenvironment. Evaluating image data on different scales would provide more insights on stroma heterogeneity and drug penetration relationship in PDAC.

6.2 Materials and Methods

6.2.1 Animal Tumor Model

All animal procedures were conducted under the protocol approved by the Dartmouth Institutional Animal Care and Use Committee (IACUC). 6 female athymic nude mice between the age of 6 to 8 weeks were used in this study. All mice were injected with human-derived pancreatic cell line AsPC-1 (ATCC, Cat#CRL-1682). Approximately 1×10^6 tumor cells were mixed with Matrigel (BD Biosciences, San Jose, CA) and RPMI-1640 medium then orthotopically implanted into the mouse pancreas. The tumors were grown for 2 weeks then randomized into 2 groups: control (n = 3) and losartan (n = 3). All mice were confirmed of tumor growth by palpation before treatment started.

6.2.2 Drug Preparation

Angiotensin inhibitor losartan (TCI America, Portland, OR, USA) was purchased in the form of powder. Losartan was dissolved in purified water at a concentration of 4 mg/ml.

Photosensitizer verteporfin (USP, Rockville, MD, USA) was dissolved in dimethyl sulfoxide at 1 mg/ml concentration and was diluted with PBS to obtain final concentration of 0.1mg/ml. Fluorescein labeled lectin (Vector Laboratories, Cat#FL-1211) at 2 mg/ml concentration was purchased as a marker for vascular patency.

6.2.3 Drug Delivery

Two weeks post-implantation, losartan was administered intraperitoneally (ip) each day for 7 days at 40 mg/kg. The control groups were ip injected with PBS correspondingly. Verteporfin (1 mg/kg) was intravenously injected one hour before sacrifice and lectin (1mg/kg) was also iv injected two minutes before sacrifice.

6.2.4 Verteporfin Fluorescence Imaging

Verteporfin was used to quantify drug uptake in this study. Verteporfin (1mg/kg) was iv injected one hour before animal sacrifice. After resection, the pancreatic tumor was embedded in 10% gelatin then sliced in half. Fluorescence imaging was performed by a flatbed scanner (GE Typhoon 7000) using a 473nm excitation source and 670nm long-pass filter. Fluorescence intensity was normalized by a reference material and calculated by the formula below:

$$\text{Normalized Fluorescence Signal} = \frac{\text{Sample signal} - \text{Background signal}}{\text{Reference signal} - \text{Background signal}}$$

6.2.5 Tumor Stiffness Mapping

Ex vivo tumor stiffness was determined by compression testing with 3-step loading at a maximum of 5% strain. The fiber optic pressure sensor (FISO, Quebec, Canada) was coupled with an xyz motorized table to perform compression testing at 300-micron resolution on the tumor surface. The sensor measured pressure at each of the 3-step loading using a micro-opto-mechanical system (MOMS) built in the sensor while the motorized

table kept track of the x-y coordinates and z-displacement. This mapping procedure provided regional stiffness information of AsPC-1 tumors.

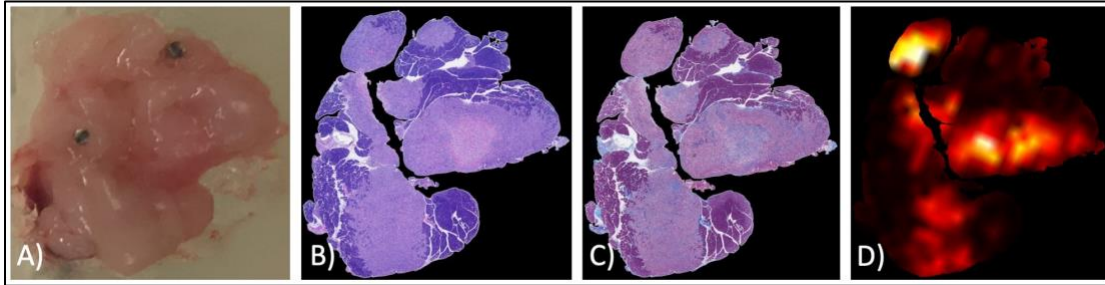


Figure 6.1 Tumor image data (A) Fresh tumor tissue was embedded in 10% gelatin with metal pins inserted to provide common points for image coregistration. (B) H&E staining of the corresponding tumor section provided markers for tissue identification (more details explained in section 2.7). (C) Masson's Trichrome staining highlighted collagen fibers in blue from which a systemic segmentation was performed to extract collagen content of tumor tissue. (D) Stiffness map of tumor tissue was coregistered to pathology data to assess regional stiffness of the tumor.

6.2.6 Pathology Images of Tissue Parameters

Tissue parameters of interest such as collagen content (Masson's Trichrome staining/white light imaging) and confirmatory tumor tissue (H&E staining/white light imaging) were obtained from 4-um thick tumor sections after being fixed with 10% formalin and embedded in paraffin. All tissue slides were scanned using a PerkinElmer Vectra3 slide scanner at 10 \times magnification.

6.2.7 Image Processing for Tumor Identification and Collagen Content

All image data was co-registered to Masson's Trichrome image using cpselect in MATLAB to obtain common points. H&E images were used to eliminate non-tumor tissues and imaging artifacts by manual ROIs. This step was crucial to make sure relevant biological parameters were extracted on tumor tissue only. Complexed tumor margins with normal pancreas or spleen tissue were discarded. **Figure 6.1A** showed that pancreas and

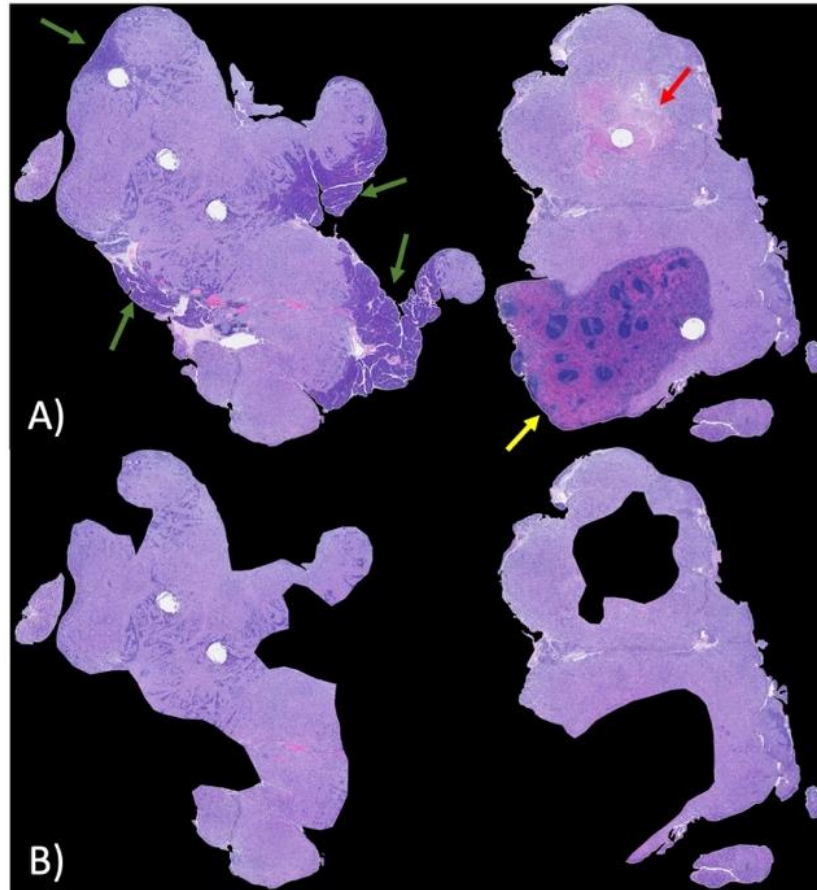


Figure 6.2. *Tissue identification from H&E staining was a first crucial step in assessing tumor biological parameters from pathology data. (A) On the left tissue, green arrows indicated normal pancreas tissue which was stained dark purple. On the right tissue, the red arrow showed the necrosis area which should be excluded from tumor analysis since this area mostly contained dead cells. The yellow arrow pointed out the spleen tissue which was often attached to the resected tumor in mouse models. Spleen tissue was also excluded before implementing any tumor analysis. (B) The two images on this second row represented the tissue samples after eliminating non-tumor artifacts such as pancreas tissue, spleen tissue and tumor necrosis.*

tumor tissues were indistinguishable in appearance. Therefore, it was likely that tumor resection process would also include normal pancreas tissue. In some cases, spleen tissue was also attached to the tumors. Therefore, manual ROIs were drawn for each tumor section to ensure artifacts were eliminated. **Figure 6.2** highlighted the tumor identification process. Arrows in different colors showed artifacts such as pancreas, spleen and necrosis

tissue. Necrosis areas were excluded because they only contained dead cells. **Figure 6.2A** illustrated H&E staining on two tumor sections and figure 2B highlighted only the tumor tissue of interest. Artifact elimination ensured accurate assessment of photosensitizer uptake and collagen profile.

Collagen content was segmented from white light images of Masson's Trichrome staining. The raw images were first converted to HSV color space in which each channel contained information on hue, saturation and value coordinates. All tumors were segmented with $0.5 < h < 0.7$, $s > 0.3$ and $v > 0.7$ which accounted for all shades of blue representing collagen fibers.

6.3 Results

6.3.1 Photosensitizer uptake and vascular perfusion enhancement in AsPC-1 tumors treated by angiotensin inhibitors

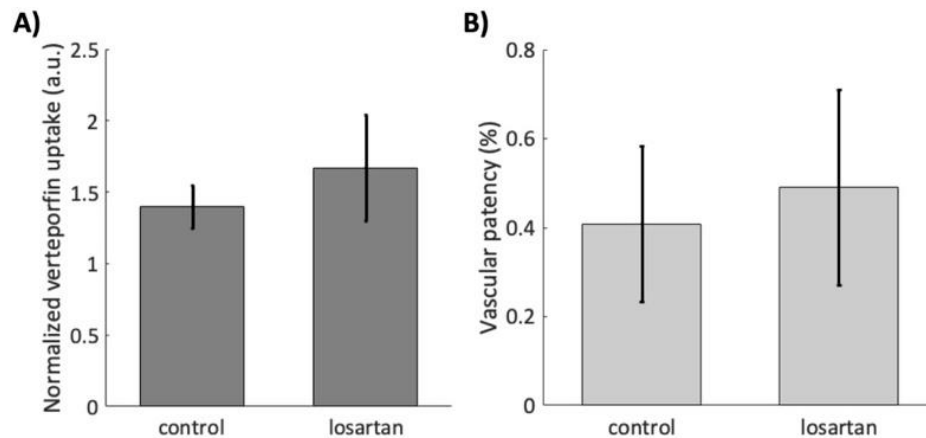


Figure 6.3 Normalized verteporfin uptake in control and treated AsPC-1 bearing mice ($n = 3$ per group). Error bars indicate one standard deviation. Preliminary data showed photosensitizer uptake enhancement in treated mice.

Preliminary data on control ($n=3$) and treated ($n=3$) AsPC-1 bearing mice showed verteporfin enhancement in mice treated with losartan. Vascular perfusion was slightly increased in the treated group. Statistical analysis was not performed due to the small

number of mice per group. Large variation within the treated group indicated that the treatment was more effective in some mice than others. Since AsPC-1 tumor cell line often displayed heterogeneous morphology, it was expected that treatment effects would not be uniform and easily explained. However, drug uptake enhancement and vascular perfusion was clearly observed in some mice, giving a ground for more testing on a larger set of mice. Specifically, under the assumption of $\alpha = 0.05$ and power = 0.8, 13 animals would be needed to observe a 25% difference in mean between the control and the treated group.

6.3.2 Modification of collagen structure and tumor stiffness heterogeneity reduction observed in treated mice

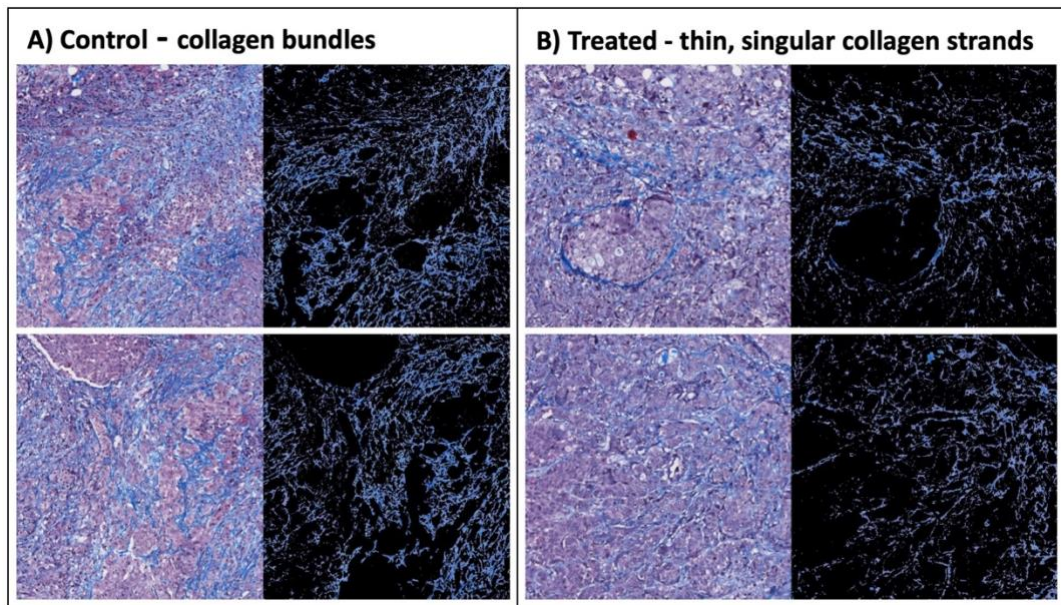


Figure 6.4. Collagen structure modification in treated mice was observed. (A) In the control group, collagen structure appeared to be made of thick bundles which included randomly oriented strands. (B) In the treated group, collagen structure was comprised of singular strands organized into thinner bundles.

While angiotensin II receptor blockers are known for their effects on collagen synthesis inhibition⁹, this study found no significant decrease in collagen production based on the analysis of tumor section as a whole. A closer look at regional collagen profile revealed an interesting observation on collagen structure modification between the control and treated groups. **Figure 6.4** displayed Masson's Trichrome staining data with collagen profile segmented by extracting blue pixels. In **Figure 6.4A**, the collagen structure consisted of thick bundles, which were comprised of thinner strands in no order. Meanwhile, collagen profile obtained from losartan treated mice showed thinner strands with less bundling. This observation was aligned with the finding from Diop-Frimpong et al. in which losartan treated tumors destabilized the mesh-like collagen structure.⁹ Quantitative confirmation of this observation would require more texture analysis in future studies. The fact that collagen profile was obtained from high resolution images of pathology data which showed a whole slice of tumor enabled the opportunity to assess the drug effect on tumor both on a larger scale of millimeters as a whole section and on a smaller scale down to micron resolution to examine regional heterogeneity.

6.3.3 No effect on tumor shrinkage and future improvement of treatment protocol

This study did not find any improvement on tumor shrinkage between the control and treated mouse groups. With the fact that AsPC-1 is an extremely malignant tumor line with short tumor growth time, it was hypothesized that angiotensin II receptor blocker treatment could yield a better result if the treatment start time was optimized. Given that pancreatic tumors are deep-seated, tumor palpation on mice was not adequate to confirm early tumor growth. Therefore, another method to confirm tumor growth in mice such as

ultrasound imaging would be crucial to exploit the narrow treatment window for AsPC-1 tumors.

6.4 Conclusion

This study has showed that losartan could be used to increase photosensitizer delivery in AsPC-1 tumor bearing mice. Collagen structure modification was observed in treated group which required more texture analysis to quantify the morphology based on high resolution data available. Future analysis methods include fractal dimension, lacunarity, collagen strand thickness assessment and clustering to quantify the size of collagen bundles. More mice would be needed to confirm the enhancement effect of photosensitizer uptake and vascular perfusion. The treatment protocol will be optimized with additional imaging method to confirm tumor growth, which is crucial for malignant tumors with fast growth rate like AsPC-1. The effect of losartan on fibroblast synthesis will also be examined with other PDAC tumor lines whose collagen structures are different than AsPC-1.

6.5 Acknowledgements

This work was funded by NIH grant P01CA084203. The authors also acknowledge the NCCC light microscopy shared resource (IPIM) supported in part by the NCI Cancer Center Support Grant 5P30 CA023108-37.

6.6 References

1. Howlader, N., Noone, A. M., Krapcho, M., Garshell, J., Miller, D., Altekruse, S. F., Kosary, C. L., Yu, M., Ruhl, J., Tatalovich, Z., Mariotto, A., Lewis, D. R., Chen, H. S., Feuer, E. J., and Cronin, K. A., 2015, "SEER Cancer Statistics Review," SEER, 28 June 2017, https://seer.cancer.gov/csr/1975_2014/
2. Stromnes, I. M., DelGiorno, K. E., Greenberg, P. D. & Hingorani, S. R. Stromal reengineering to treat pancreas cancer. *Carcinogenesis* **35**, 1451–1460 (2014).

3. Feig, C. *et al.* The pancreas cancer microenvironment. *Clin. Cancer Res.* **18**, 4266–76 (2012).
4. Mbeunkui, F., Johann, D. J. & Jr. Cancer and the tumor microenvironment: a review of an essential relationship. *Cancer Chemother. Pharmacol.* **63**, 571–82 (2009).
5. Neesse, A., Algül, H., Tuveson, D. A. & Gress, T. M. Stromal biology and therapy in pancreatic cancer: a changing paradigm. *Gut* **64**, 1476–1484 (2015).
6. Proton w/FOLFIRINOX-Losartan for Pancreatic Cancer - Full Text View - ClinicalTrials.Gov.” Accessed February 20, 2019. <https://clinicaltrials.gov/ct2/show/NCT01821729>.
7. Chauhan, V. P. *et al.* Angiotensin inhibition enhances drug delivery and potentiates chemotherapy by decompressing tumour blood vessels. *Nat. Commun.* **4**, 2516 (2013).
8. Kumar, V. *et al.* Noninvasive Assessment of Losartan-Induced Increase in Functional Microvasculature and Drug Delivery in Pancreatic Ductal Adenocarcinoma 1. *Transl. Oncol.* **9**, 431–437 (2016).
9. Diop-Frimpong, B., Chauhan, V. P., Krane, S., Boucher, Y. & Jain, R. K. Losartan inhibits collagen I synthesis and improves the distribution and efficacy of nanotherapeutics in tumors. *Proc. Natl. Acad. Sci. U. S. A.* **108**, 2909–14 (2011).

Chapter 7: Stiffness Heterogeneity as an Indicator of Drug Delivery Enhancement by Photodynamic Priming in Pancreatic Adenocarcinoma

This chapter is on-going work in preparation for submission:

P. Vincent, et al., “Stiffness heterogeneity as an indicator of drug delivery enhancement by photodynamic priming in pancreatic adenocarcinoma.” **In preparation.**

7.1. Introduction

A total of 80% of pancreatic cancer patients are diagnosed with pancreatic ductal adenocarcinoma (PDAC), and these patients have an abysmal 5-year survival rate of 8% that has been unchanged for the past 30 years.¹ The disease is commonly diagnosed at a late stage, and so has only a 20% rate of tumor resectability^{2,3}. This situation calls for more premeditated research efforts into finding alternative treatment regimens that work for these advanced stage tumors. Besides conventional options such as surgery and chemotherapy, targeted therapies have emerged to offer novel approaches to PDAC treatments.^{4,5} While there are more options, tumor drug transport remains the governing mechanism to determine treatment efficacy. As more evidence is revealed to support the role of the tumor microenvironment (TME) on the pathophysiology that affects drug transport⁶⁻⁸, recent combination treatment have focused on using a neoadjuvant therapy to target the TME followed by a more conventional option such as chemo or immunotherapy.^{9,10} Alongside with this growing trend, photodynamic therapy (PDT) has been studied as a method of preparing the tumor for subsequent chemotherapy. Traditionally, PDT as a localized treatment is very effective in killing tumor cells via necrosis. Recent preclinical findings, however, have showed that low-dose PDT could

prepare the tumors efficiently by targeting the TME parameters associated with drug transport. Huang et al provided evidence for the benefits of low-dose PDT in enhancing vascular permeability while Obaid et al highlighted the possibility of tumor collagen depletion.^{11,12} While early data supports the use of low-dose PDT as an effective method to normalize the TME for subsequent treatments, positive treatment effect confirmation requires sample collection and analysis at a cellular level and/or with additional pathology and immunohistochemistry staining, both of which come as costly and challenging for clinical adoption.

In this study, the low-dose PDT effects upon the TME was investigated using an orthotopic mouse model implanted with BxPC-3, a human-derived tumor cell line with particularly dense and thick stroma as observed in characteristic PDAC patients. Besides collagen modulation and the corresponding enhanced drug uptake as treatment effects, the study specifically focused on establishing the relationship between such microscopic-level changes with tumor stiffness, a relevant biomechanics parameter that could be imaged wide-field at a resolution adequate for drug transport evaluation. Tumor stiffness heterogeneity was measured from fresh, ex vivo samples using a previously established high-resolution mapping system.¹³ Whole-tumor assessment was conducted to evaluate the low-dose PDT effects on the tumor collagen, vascular patency and drug uptake as well as the feasibility of using stiffness information to indicate such changes in the TME. Since recent elastography imaging advancements show reasonably promising progress towards clinical use with the capability of wide-field imaging (tens of mms) at an improved spatial resolution, the ability to confirm apparent changes in stiffness and how it might be

indicative of drug delivery and treatment responses would signify a critical step towards clinical PDAC treatment.

7.2 Materials and Methods

7.2.1 Orthotopic mouse model

All animal procedures were conducted under the protocol approved by the Dartmouth Institutional Animal Care and Use Committee (IACUC). A total of 12 nude mice ranging from 6-8-week-old were used in this study. The mice were orthotopically injected with the BxPC-3 tumor cell line (ATCC, Cat# CRL-1687) in the pancreas. 1×10^6 tumor cells were mixed with Matrigel at a 1:1 ratio to a total of 50- μ L injection volume. Tumors were allowed to grow for 5-7 weeks until approximately 10-mm diameter, as assessed by external palpation.

7.2.2 Photodynamic priming treatment

The 12 mice were randomized into a control group of 5 mice and a treated group of 7 mice. The control group did not receive any drug injection or light treatment. The mice in the treated group were intravenously injected with BPD 0.5 mg/kg (Visudyne, NJ). One-hour after the injection, the pancreas was exposed and light treatment was given via a 690-nm fiber optic cable at a dose of 75 J/cm² and irradiance of 100 mW/cm². After light treatment, the pancreas was closed and the mice were sacrificed 48 hours after. Dextran (Thermo Fisher Scientific, Cat#D1830) was intravenously injected 1-hour before sacrifice as a marker for drug uptake while Lectin (Vector Laboratories, Cat#FL-1171-1) was injected 2-min before sacrifice to mark vascular patency.

7.2.3 Imaging of biological parameters

Dextran fluorescence imaging as drug uptake marker

The tumors were harvested for ex vivo imaging of interested biological parameters including dextran (drug uptake), stiffness and collagen, all of which were performed on the fresh tumor tissue. Dextran fluorescence was imaged by a flatbed scanner (GE Typhoon 700) using a 532-nm source and a 580-nm long pass filter.

Tumor stiffness heterogeneity imaging

The tumor stiffness was then collected by a point probe stiffness mapping system as described in Vincent et al.¹³ In brief, the system scanned through the whole tumor surface at 300-micron resolution steps. At each location, three pressure values corresponding to three indentations were collected to calculate the Young's modulus, or stiffness in kPa. A map of tumor stiffness heterogeneity was generated to visualize the stiffness as a image that could be spatially correlated with pathology images.

Pathology staining and imaging of necrosis and vascular patency

The tumors were then prepared for pathology staining to identify collagen (Masson's Trichrome), and necrosis or cell death (H&E), by formalin fixation followed by paraffin embedding and slicing at 4 microns. The pathology slides were imaged at 10x magnification using a PerkinElmer Vectra3 slide scanner. Vascular patency was determined by lectin fluorescence also at 10x magnification.

7.2.4 Image processing

All images were co-registered to Trichrome image in matlab using rigid transformation. Collagen content extracted from Trichrome images were determined by calculating the

percentage of segmented blue pixels over the total pixels representing tumor tissue. The color segmentation was performed in hue-saturation-value space with cutoff values as followed: $0.5 < \text{hue} < 0.7$, $\text{saturation} > 0.5$ and $\text{value} > 0.7$. Necrosis area was manually identified from H&E images, then an area percentage of necrosis over tumor tissue was calculated. These manually drawn necrosis ROIs, along with spleen and pancreas tissue ROIs, were used to exclude corresponding regions from the rest of the image data, so that PDP effects were assessed only on tumor regions with viable tumor cells. Dextran fluorescence intensity was calculated with a normalized threshold of 0.2. Background subtraction was necessary for lectin image data followed by a normalized threshold of 0.25 with a control checkpoint that blood vessels typically fell in the range of 1-5% of tumor tissue area.

7.2.5 Texture analysis

Texture analysis was performed on stiffness data by first creating the gray-level co-occurrence matrices (GLCMs) using the *graycomatrix* functions in matlab. GLCM texture features were generated with no data binning. The gray limits were the absolute minimum and maximum stiffness value collected from the 12 tumors. GLCM texture features such as homogeneity, contrast, correlation and energy (or uniformity) were calculated by the matlab function *graycoprops*.

7.2.6 Statistical analysis

Student's t-test performed in matlab was used to evaluate the difference in means between the control and the treated tumor groups, with no assumption of equal variance and $\alpha = 0.05$.

7.3 Results

7.3.1 PDP relieved overall stiffness and collagen density, more vascular patency and enhanced delivery

In **Figure 7.1A**, the average tumor size for the control and the treated groups are 422 mm³ and 469 mm³, respectively. A student's T-test with $p = 0.65$ suggested that there is no statistically significant difference in the size, indicating that tumors were harvested at the same growing stage so the collagen profile was apparently unaffected by tumor progression. Therefore, changes in collagen content between the two groups are due to the treatment effect. **Figure 7.1B** displaying the marked difference in necrosis area percentage between the control and the treated groups (7% and 19%, respectively) was reported to confirm that PDT treatment was given successfully in the treated group. The 7% necrotic area observed in the control group also suggests that the tumors had inherent necrosis as part of their progression. **Figure 7.1C-F** summarizes the PDP treatment effect observations, in which the treated group resulted in 20% more dextran uptake ($p = 0.011$), 28% more vascular patency ($p = 0.073$), 30% reduction in collagen percentage ($p = 0.001$) and 21% decrease in overall tumor stiffness in kPa ($p = 0.008$). These changes are reported with the exclusion of all necrosis areas, and also with the exclusion of 1 treated mouse that displayed unusually high collagen and stiffness profile.

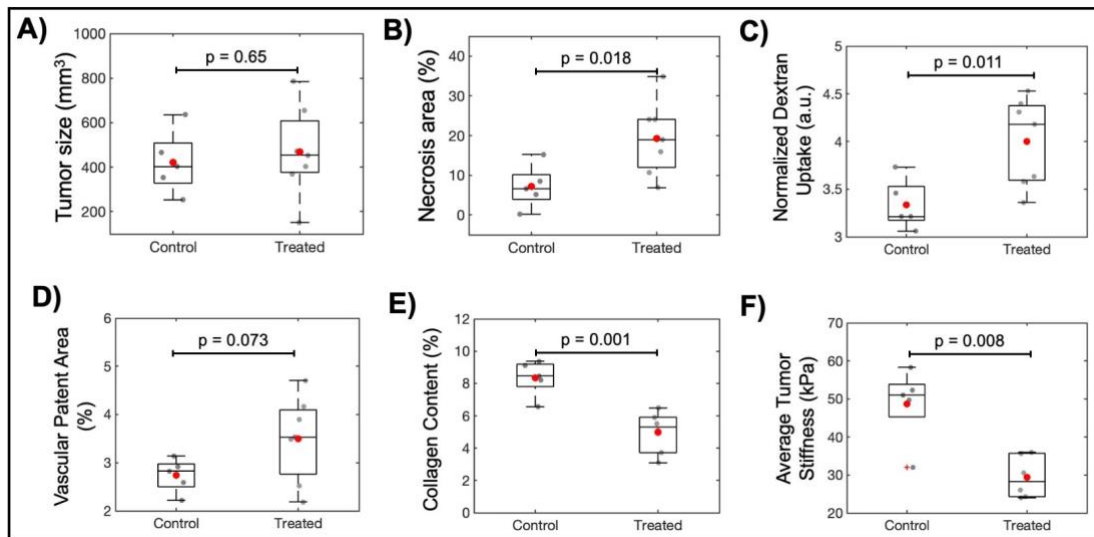


Figure 7.1 PDAC Tumor Microenvironment Modulation Effects from Photodynamic Priming Treatment **A)** Tumor size measured after resection showed no statistical difference between the control and the treated group ($p = 0.65$), implying that tumors were harvested at the same growing stage which eliminated potential for collagen proliferation variations due to different tumor progression time. **B)** There was a statistical difference in necrotic areas after PDT, as identified from H&E staining between the groups ($p = 0.018$). The control group had inherent necrosis due to the nature of tumor progression and the treated group resulted in 2-fold of necrosis, confirming successful PDT treatment. **C)** Normalized dextran fluorescence intensity was used to evaluate drug uptake. There was a 22% increase in drug uptake from the treated group ($p = 0.011$). **D)** Lectin fluorescence was quantified to show that vascular patent area increases by 28% in the treated tumors ($p = 0.073$). **E)** Collagen content percentage calculated from Masson's Trichrome staining showed a 30% decrease as a result of PDT treatment ($p = 0.001$). **F)** Average tumor stiffness was decreased by 21% as compared to the control group ($p = 0.008$). Control group $n = 5$, treated group $n = 7$ (Figure A-E) and $n = 6$ (Figure 1F).

7.3.2 Tumor stiffness could be used to predict tumor drug uptake and treatment response

Visualization of the PDP effects on tumor collagen, stiffness and drug uptake as compared across the control tumor ($n = 5$), treated tumors ($n = 7$) including an outlier highlighted in **Figure 7.2A**. Besides the marked difference in all three parameters between the control and the treated, this visual panel is displayed to show the dense stroma observed in the

outlier tumor. Despite a large necrosis area as evidence of treatment given, this tumor had dense collagen and an unusually high overall stiffness was measured. Correlations between parameters relevant to tumor drug delivery are illustrated in the plots of **Figure 7.2B**. A high correlation between vascular patency and the amount of dextran fluorescence uptake was expected ($R^2 = 0.79$), which remains true across all tumors in the study. While the

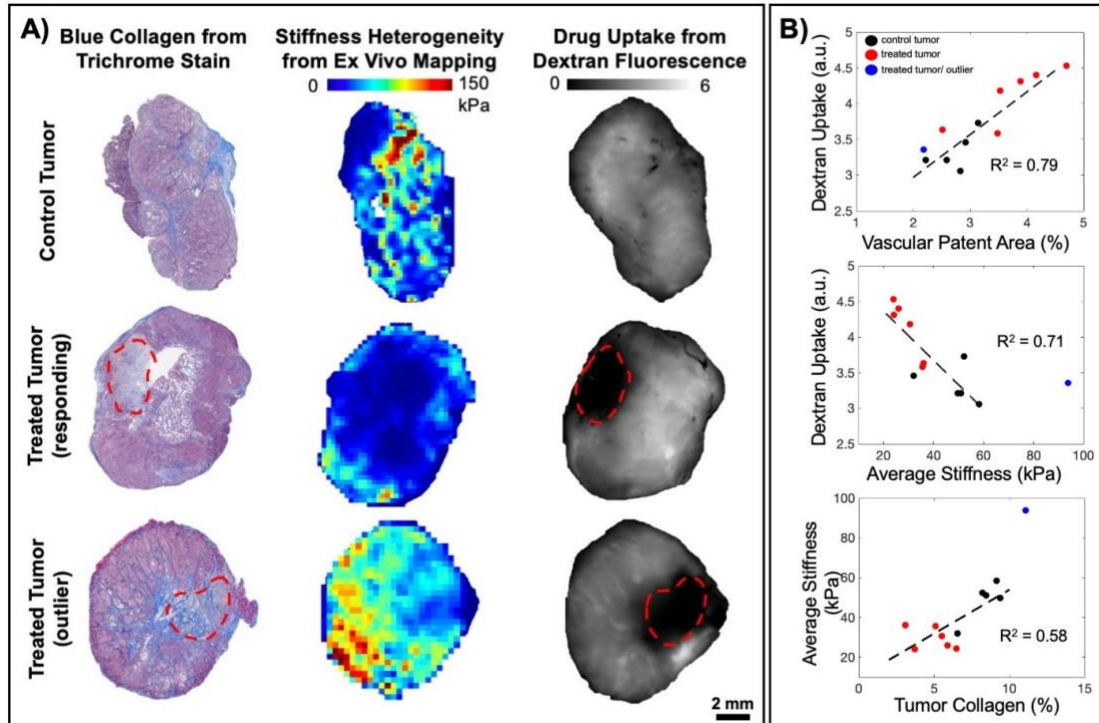


Figure 7.2 PDP relieves overall stiffness and collagen density which allowed more dextran delivery in treated tumors A) A panel of tumors divided into three categories is presented (control = 5 tumors, responding = 6 tumors, outlier = 1 tumors). Visualization of collagen distribution as blue staining from Trichrome data is displayed in the first column. Necrosis areas are identified by the red dotted line to confirm that treatment was given. The middle column shows stiffness heterogeneity with values ranging from 0 to 150 kPa. The last column highlights dextran fluorescence as tumor drug distribution. B) For all the tumors in this study ($n = 12$), dextran uptake and vascular patency are strongly correlated ($R^2 = 0.79$). Average stiffness is inversely correlated to drug uptake ($R^2 = 0.71$) but is correlated to tumor collagen content ($R^2 = 0.58$). The linear regression generated with stiffness data in the last two plots excluded the outlier tumor (blue dot) due to its unusually high stiffness value.

outlier tumor with very high stiffness value was excluded from the two plots below, both the control tumors ($n = 5$) and the responding tumors ($n = 6$) validate the inverse relationship between stiffness and dextran uptake ($R^2 = 0.71$) and the proportional relationship between average stiffness and tumor collagen ($R^2 = 0.58$). The results in this section corroborate the idea of using tumor stiffness as an indicator of drug delivery efficiency and corresponding treatment responses for PDAC tumors.

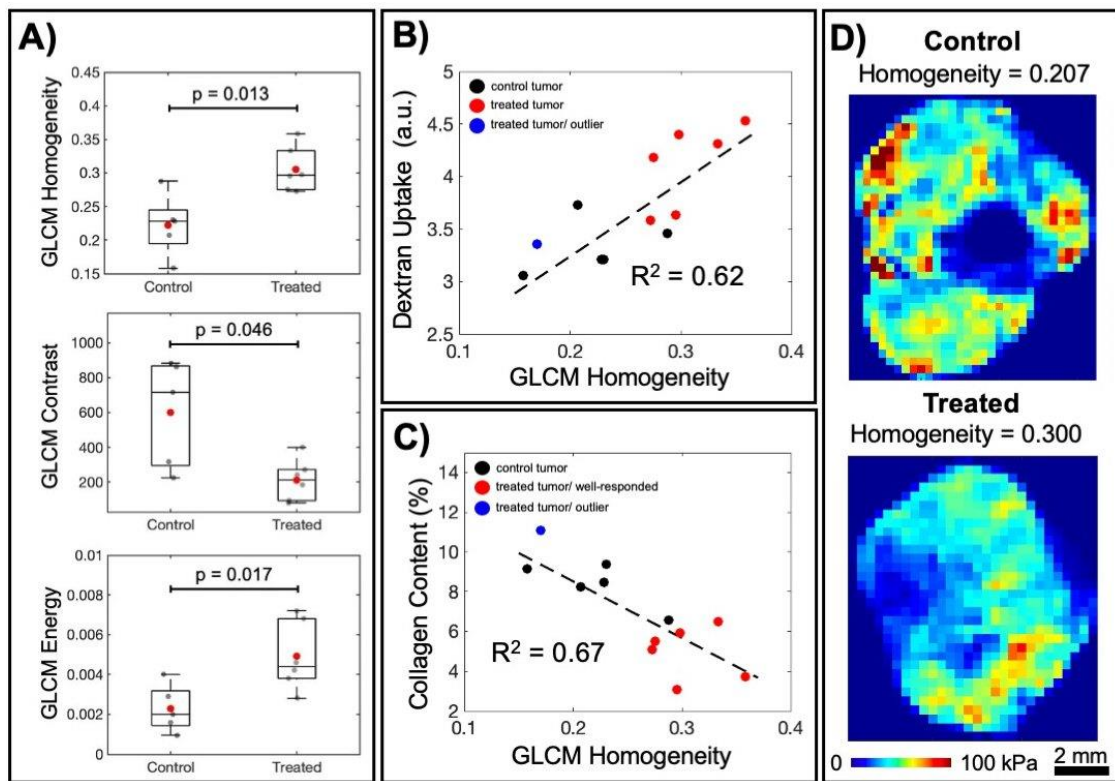


Figure 7.3 Texture Analysis of Tumor Stiffness Shows Homogeneity as an Indicator of Treatment Response A) Results of GLCM texture analysis on tumor stiffness data is demonstrated. Homogeneity and Energy (or Uniformity) of stiffness values are found to be increased after PDT treatment ($p = 0.013$ and $p = 0.017$, respectively), while GLCM contrast or variation is decreased after treatment ($p = 0.046$). B-C) GLCM Homogeneity is correlated with dextran uptake in both control and treated tumors ($R^2 = 0.62$) and is inversely correlated with collagen content ($R^2 = 0.67$), indicating that this texture feature could be used to predict treatment outcome. D) Visualization of stiffness homogeneity in control and treated tumors with their corresponding GLCM Homogeneity scores.

7.3.3 Tumor heterogeneity is reduced after PDT treatment, as measured by texture analysis.

Texture analysis features from the GLCM package are reported in **Figure 7.3A** for the control and the treated tumors. The three texture features are in agreement that after treatment, the tumors became more homogenized (Homogeneity $p = 0.013$, Energy/Uniformity $p = 0.017$). The contrast within the tumors in the treated group is reduced (Contrast $p = 0.046$). More interestingly, the GLCM Homogeneity feature obtained from stiffness data also shows a strong correlation with dextran uptake ($R^2 = 0.62$) and the tumor stroma ($R^2 = 0.67$), as illustrated in **Figure 7.3B-C**. It is noticeable that the outlier tumor with very high mean stiffness (blue dot) has a very low Homogeneity score. A visual comparison of stiffness values between a low and a high Homogeneity score of is displayed in **Figure 7.3D**. The texture analysis results in this section suggested that tumor stiffness homogeneity could be a reliable indicator of tumor treatment responses as it reflects the stroma and the resulting drug uptake for all the tumors in this study.

7.4 Discussion

PDT treatment of solid tumors can target multiple cell death pathways^{14,15} and enhances vascular permeability¹⁶⁻¹⁸, making this therapeutic regimen an effective acute mechanism for combination therapies when combined with a systemic regimen. While evidence suggests that PDT offers additive and synergistic effects to chemotherapy and immunotherapy, little is known about the possibility of stroma modification. This study was motivated by recent findings that advocate for the use of PDT in modulating tumor collagen, a well-established hindering factor of intratumoral drug distribution. Li et al reported a significant reduction of cancer-associated fibroblasts followed by a decrease of

tumor collagen and an enhancement of nanoparticle uptake in 4T1 tumors after PDT treatment.¹⁹ Obaid et al showed evidence for collagen photomodulation in mice receiving PDT treatment with their optimized nanoconjugate.¹² In this study, BxPC-3 tumors in an orthotopic mouse model were employed to examine the stromal modulating effects of this treatment, as BxPC-3 recapitulates very dense stroma with thick collagen fibers often observed in PDAC patients. Accordingly, results from **Figure 7.1** and **7.2**, the treatment caused a reduction of 30% in collagen content and consequently a 20% enhancement in dextran fluorescence. The study exploited treatment-induced necrosis information only to confirm when positive treatment was given, since significant necrosis is well-documented as a PDT effect. By only analyzing the TME factors from the non-necrotic tumor areas, the study provided strong evidence for the use of PDP as a neoadjuvant scheme to prepare the tumor for subsequent therapeutic options that depend on a systemic drug delivery.

The need for a reliable, clinically translatable biomarker that could indicate the TME pathophysiology relevant to tumor drug distribution, either with or without treatment, is a significant problem that this study was motivated to address. Tumor stiffness information and its relationship to the stroma and the drug uptake has been established as such a biomarker in this study. While **Figure 7.1F** suggested a 21% reduction in overall average stiffness between the control and PDT treated groups, a correlation between tumor stiffness and other parameters of interests was established in **Figure 7.2**. The inverse correlation with drug uptake ($R^2 = 0.71$) and the proportional relationship with collagen content ($R^2 = 0.58$) were reported to be consistent throughout both the control and the treated tumors, indicating that stiffness information was a reliable surrogate for tumor drug delivery efficiency and also PDT treatment efficacy in this case. The visualization and the plots

provided in in **Figure 7.2** also highlight the one tumor that received treatment, showed clear treatment-induced necrosis but no changes in dextran uptake or collagen profile. Interestingly, the average stiffness measured for this tumor was three times higher than the rest of the tumors in the study (outlier = 94 kPa, remaining treated group = 30 kPa). Correspondingly, the collagen profile illustrated an extreme desmoplasia with the highest density located at where necrosis occurred, i.e., where maximum light treatment was given. It is hypothesized that such particular collagen density hindered the priming effects of PDT, therefore, no dextran uptake enhancement was observed in the remaining viable tumor region.

Since tumor heterogeneity promoting selective drug resistance at the cellular level has been corroborated by both preclinical and clinical studies²⁰⁻²³, this study focused on the TME heterogeneity specifically. There was also an attempt to investigate the intratumoral stiffness variations as a possible surrogate for tumor drug uptake at a macroscopic level. With the emphasis on finding a clinically translatable marker, heterogeneity information was collected at whole-sample field of view (tens of millimeters) and transport-relevant resolution (hundreds of microns) to capture the changes within the whole tumor. Stiffness homogeneity calculated by the well-established GLCM approach was found to have a strong correlation with dextran uptake ($R^2 = 0.62$) and tumor collagen ($R^2 = 0.67$) for all tumors in this study. It is noticeable from **Figure 7.3B-C** that the outlier tumor with unusually high mean stiffness was among the tumors with the lowest GLCM Homogeneity score, suggesting that stiffness heterogeneity could potentially be a reliable marker to predict PDAC tumor drug uptake regardless of absolute stiffness measurements. With current wide-field stiffness imaging techniques such as ultrasound or magnetic resonance

elastography capable of producing 1-mm resolution mapping, it is encouraging to recognize not only the significance of elastography information with respect to intratumoral drug delivery, but also the feasibility of employing elastography in a clinical setting.

Perhaps most importantly, the observation of this one outlier tumor indicates the necessity to longitudinally image tumors before and after PDT treatment, to properly assess the pre-existing conditions of necrosis and stiffness, such that differences from a baseline can be established. This was not possible in this *ex vivo* analysis study, but would potentially be possible with diagnostic imaging methods.

7.5. Conclusion

Results from this study support the use of low-dose PDT to target PDAC tumor stroma as an effective approach of normalizing the TME and thus enhancing the intratumoral drug uptake. Furthermore, tumor stiffness information from both the control and the treated tumors is demonstrated to reflect the collagen content, and stiffness shows a strong inverse relationship with drug distribution. Imaging of absolute stiffness along with texture analysis on the stiffness spatial variations at transport-relevant spatial resolution shows the fundamental validations needed to consider the eventual feasibility of clinical elastography data to be used as a surrogate biomarker of intratumoral drug delivery in PDAC.

7.6. Acknowledgements

This work was funded by NIH grant P01 CA084203. The authors acknowledge the NCCC light microscopy shared resource (IPIM) and the Pathology shared resource (PSR) supported in part by NCI Cancer Center Support Grant P30 CA023108.

7.7 References

1. Sun, H., Ma, H., Hong, G., Sun, H. & Wang, J. Survival improvement in patients with pancreatic cancer by decade: a period analysis of the SEER database, 1981-2010. *Sci. Rep.* **4**, 6747 (2014).
2. Siegel, R., Naishadham, D. & Jemal, A. Cancer statistics, 2013. *CA. Cancer J. Clin.* **63**, 11–30 (2013).
3. Gillen, S., Schuster, T., Meyer zum Büschenfelde, C., Friess, H. & Kleeff, J. Preoperative/Neoadjuvant Therapy in Pancreatic Cancer: A Systematic Review and Meta-analysis of Response and Resection Percentages. *PLoS Med.* **7**, e1000267 (2010).
4. Rossi, M. L., Rehman, A. A. & Gondi, C. S. Therapeutic options for the management of pancreatic cancer. *World Journal of Gastroenterology* **20**, 11142–11159 (2014).
5. Nevala-Plagemann, C., Hidalgo, M. & Garrido-Laguna, I. From state-of-the-art treatments to novel therapies for advanced-stage pancreatic cancer. *Nature Reviews Clinical Oncology* **17**, 108–123 (2020).
6. Kota, J., Hancock, J., Kwon, J. & Korc, M. Pancreatic cancer: Stroma and its current and emerging targeted therapies. *Cancer Lett.* **391**, 38–49 (2017).
7. Stylianopoulos, T., Munn, L. L. & Jain, R. K. Reengineering the Physical Microenvironment of Tumors to Improve Drug Delivery and Efficacy: From Mathematical Modeling to Bench to Bedside. (2018). doi:10.1016/j.trecan.2018.02.005
8. Stromnes, I. M., DelGiorno, K. E., Greenberg, P. D. & Hingorani, S. R. Stromal reengineering to treat pancreas cancer. *Carcinogenesis* **35**, 1451–1460 (2014).
9. Gallagher-Colombo, S. M. *et al.* Erlotinib pretreatment improves photodynamic therapy of non-small cell lung carcinoma xenografts via multiple mechanisms. *Cancer Res.* **75**, 3118–3126 (2015).
10. Bao, R. *et al.* Enhancing Anti-PD-1/PD-L1 Immune Checkpoint Inhibitory Cancer Therapy by CD276-Targeted Photodynamic Ablation of Tumor Cells and Tumor Vasculature. *Mol. Pharm.* **16**, 339–348 (2019).
11. Huang, H.-C. *et al.* Photodynamic Priming Mitigates Chemotherapeutic Selection Pressures and Improves Drug Delivery. *Cancer Res.* **78**, 558–571 (2018).
12. Obaid, G. *et al.* Impacting Pancreatic Cancer Therapy in Heterotypic in Vitro Organoids and in Vivo Tumors with Specificity-Tuned, NIR-Activable Photoimmunonanoparticles: Towards Conquering Desmoplasia? *Nano Lett.* **19**, 7573–7587 (2019).

13. Vincent, P. *et al.* High-resolution ex vivo elastography to characterize tumor stromal heterogeneity in situ in pancreatic adenocarcinoma. *IEEE Trans. Biomed. Eng.* 1–1 (2020). doi:10.1109/tbme.2019.2963562
14. Mroz, P., Yaroslavsky, A., Kharkwal, G. B. & Hamblin, M. R. Cell death pathways in photodynamic therapy of cancer. *Cancers* **3**, 2516–2539 (2011).
15. Moor, A. C. E. Signaling pathways in cell death and survival after photodynamic therapy. *Journal of Photochemistry and Photobiology B: Biology* **57**, 1–13 (2000).
16. Snyder, J. W., Greco, W. R., Bellnier, D. A., Vaughan, L. & Henderson, B. W. Photodynamic Therapy: A Means to Enhanced Drug Delivery to Tumors. *Cancer Res.* **63**, 8126–8131 (2003).
17. Gao, W. *et al.* Photodynamic therapy induced enhancement of tumor vasculature permeability using an upconversion nanoconstruct for improved intratumoral nanoparticle delivery in deep tissues. *Theranostics* **6**, 1131–1144 (2016).
18. Seshadri, M. *et al.* Tumor Vascular Response to Photodynamic Therapy and the Antivascular Agent 5,6-Dimethylxanthenone-4-Acetic Acid: Implications for Combination Therapy. (2005).
19. Li, L. *et al.* Photosensitizer-Encapsulated Ferritins Mediate Photodynamic Therapy against Cancer-Associated Fibroblasts and Improve Tumor Accumulation of Nanoparticles. *Mol. Pharm.* **15**, 3595–3599 (2018).
20. Haeberle, L. *et al.* Stromal heterogeneity in pancreatic cancer and chronic pancreatitis. *Pancreatology* **18**, 536–549 (2018).
21. Shah, A. T., Diggins, K. E., Walsh, A. J., Irish, J. M. & Skala, M. C. In Vivo Autofluorescence Imaging of Tumor Heterogeneity in Response to Treatment. *Neoplasia* **17**, 862–870 (2015).
22. Lim, Z. F. & Ma, P. C. Emerging insights of tumor heterogeneity and drug resistance mechanisms in lung cancer targeted therapy. *Journal of Hematology and Oncology* **12**, (2019).
23. Wang, X., Zhang, H. & Chen, X. Drug resistance and combating drug resistance in cancer. *Cancer Drug Resist.* **2**, 141–160 (2019)

Chapter 8: Radiomics Analysis on CT Scans of Patients Receiving PDT Treatment to Quantify PDP Effects

The following manuscript will be submitted to Physics in Medicine and Biology:

P. Vincent, et al., “CT radiomic features of photodynamic priming in clinical pancreatic adenocarcinoma treatment.” **Prepared for Submission.**

8.1 Introduction

Pancreatic ductal adenocarcinoma (PDAC) accounts for more than 90% of all pancreatic malignancies¹ with an abysmal 5-year survival rate of 8%.² Limited treatment options, with only 20% of the patients surgically resectable,^{3,4} have fueled a drive towards developing and advancing alternative PDAC treatments that combine ablative technologies with systemic therapies. Along with this effort, photodynamic therapy (PDT) has been studied as a promising localized and well-tolerated focal treatment option for solid tumors.⁵⁻⁷ A light-activated drug is systemically introduced into the body but only at the regions treated with light will singlet oxygen be generated to cause cell death. Beyond focal treatment effects, recent studies in murine models have reported that a lower dose of PDT, termed “photodynamic priming” (PDP), could prove beneficial as a neo-adjuvant method to prime or alter the tumors to enhance chemotherapy or immunotherapy.⁸⁻¹⁰ Pre-clinical data have showed that PDP effectively relieves the physical tumor drug delivery barriers by targeting protein expressions responsible for drug resistance¹¹ and modulating desmoplasia,¹² allowing for a lower dose of chemotherapy to achieve the same efficacy. However, while PDT effects could be observed by identifying necrotic areas on a patient’s CT scan,¹³ PDP effects are more difficult to discern and often require ex vivo imaging

techniques or further pathology staining, both of which are not clinically feasible with PDAC treatment. In this study, the CT scan alterations seen in clinical treatments were examined in a pilot cohort, to assess the potential of detecting successful PDP outcomes.

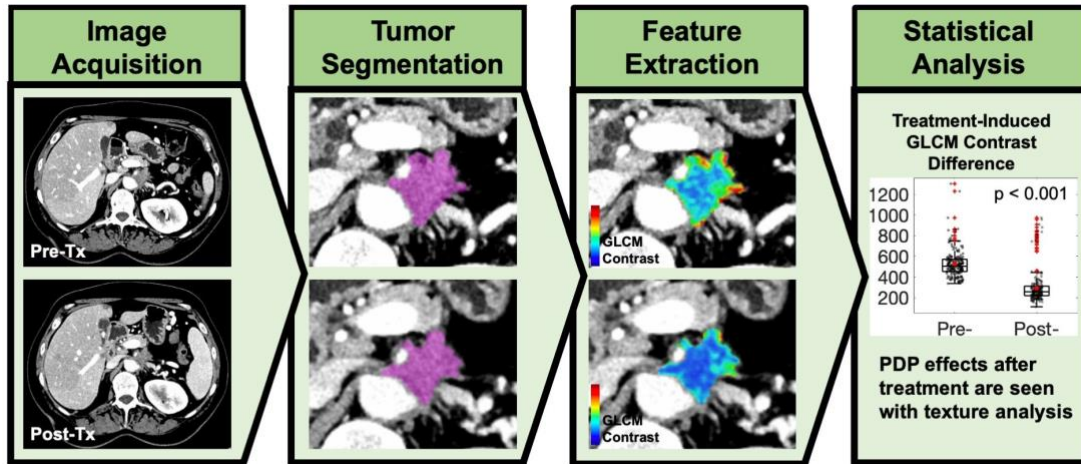


Figure 8.1 Overview of texture analysis in assessment of photodynamic therapy treatment on PDAC patients. Each patient received a pre-treatment and a post-treatment CT scan. Pancreatic tumor segmentation was performed, and texture analysis was carried out to extract underlying features that showed significant differences after the treatment.

Radiomics has recently emerged as an effective method to obtain further information from clinical image data.^{14–16} PET, CT and MRI are widely used to assist doctors in both diagnosis and therapy, yet only a limited amount of image data is extracted. For example, CT scans are acquired to identify tumor stages, but quantitative data reported remains on first-order parameters such as tumor size and average CT density value in Hounsfield Units (HU). Texture analysis with the goal of extracting further information indiscernible to simple inspection has offered a tool to provide quantitative data that are proven to be clinically valuable. In the field of pancreatic cancer, a few studies have been conducted using texture analysis to evaluate treatment effects,¹⁷ predict survival outcomes¹⁸ or stratify different types of cystic lesions.¹⁹ Since PDAC has significant stromal components^{20–22} often leading to lack of perfusion and high heterogeneity, texture

analysis is speculated to be of potential utility. Furthermore, biopsy is typically avoided in PDAC so diagnostic information from CT can be particularly valuable as CT imaging is perhaps the most widely used tool to assess tumor status.

This study was carried out with the objective of using texture analysis to examine CT scans before and after photodynamic light treatment to assess the underlying effects (**Figure 8.1**). LIFEx software, a widely used Radiomics package,²³ was used to segment regions of interest and perform texture analysis. The first aim of the study focused on comparing tumor regions that responded to light treatment with focal necrosis (termed PDT regions). The second part of the study was to analyze areas that did not show apparent necrosis but were suspected to be within the treated tumor (termed PDP regions). This second aim to employ texture analysis for evidence of PDP was done by comparing pre-treatment and post-treatment CT scans to identify differences that would show underappreciated texture-based changes in the images.

8.2 Materials and Methods

8.2.1 Patient population

Locally advanced PDAC patients were recruited at the Mayo Clinic (Rochester, MN) for the photodynamic therapy trial. There were 7 patients receiving treatment in this pilot study and their pre-treatment and post-treatment CT scans were used. All scans were fully anonymized prior to access and analysis. A summary of patient characteristics is provided in **Table 8.1**. Most patients were in T3 stage with tumor site located at the pancreatic head. The initial tumor volume range was $23 \pm 17 \text{ cm}^3$. The patients received a pre-treatment CT scan to identify the tumor site around one week before the treatment occurred (with the exception of Patient 06 whose pre-treatment scans were 20 days before).

One hour before the light treatment, Visudyne (Novartis, East Hanover, NJ) at 0.4 mg/kg body weight was intravenously injected. Light treatment with endoscopic ultrasound guidance was performed using a 690-nm light source (Model PSU-FC, Changchun New Industries Optoelectronics Technology Co. Ltd., Jilin, China) at 40 J/cm. The light source fiber was inserted via the duodenum into the tumor. 48 hours after the treatment, a post-treatment CT scan was acquired to evaluate the treatment effects.

8.2.2 Image Acquisition and Segmentation

Patient	Age (y)	Sex	Disease Stage	Tumor Site	Tumor Volume (cm ³)		Tumor Attenuation (HU)	
					Pre-Tx	Post-Tx	Pre-Tx	Post-Tx
01	65	M	T3	Pancreatic Head, Tail, and Neck	54	45	86 ± 32	77 ± 26
02	53	M	T2	Pancreatic Head	8	6	68 ± 27	67 ± 24
03	73	F	T3	Pancreatic Head	30	28	61 ± 23	47 ± 20
04	57	F	T3	Pancreatic Body and Tail	11	11	76 ± 24	68 ± 19
05	63	F	T3	Pancreatic Head	36	39	81 ± 35	69 ± 24
06	62	M	T1	Pancreatic Head	7	6	96 ± 33	64 ± 39
07	75	M	T3	Pancreatic Neck	17	18	74 ± 31	63 ± 23

Table 8.1 Summary of patient characteristics

All CT scans were acquired by a Siemens Force DS/129 scanner with the tube voltage in the range of 100-120 kVp, the tube current in between 97-166 mAs, the pixel spacing varying between 0.742 – 0.859 mm and the slice thickness of 1mm. Non-ionic contrast media iohexol (Omnipaque 300 mg I/mL, GE Healthcare Ireland, Cork, Ireland) with bolus tracking was used in the image acquisition process. Scans were acquired post-injection at 35 seconds for late arterial phase and 90 seconds for portal venous phase. Texture analysis was performed on the portal phase of the scans.²⁴⁻²⁶ Also, previous studies^{27,28} have reported that the tube current variation does not affect tissues with high level of texture such as tumorous tissues.

Pancreatic tumor segmentation was performed by a clinical radiologist from the Department of Radiology at Dartmouth-Hitchcock Medical Center (Lebanon, New Hampshire). The radiologist was informed that the CT scans were acquired for a PDT

treatment at the pancreatic tumor site and received a 1-hour training on how to perform ROI segmentation in the software LIFEx. Slice-by-slice delineation of tumor boundary was manually drawn on the tumors of all patients. The basis of tumor boundary delineation was determined based on the late arterial scans since they provided a better tumor margin visualization. Additionally, for patients that showed a treatment-induced necrosis, those areas were also specified. A trained graduate student then complete the ROI filling based on the specified tumor boundaries. Air, dense calcification and large blood vessels were excluded from the ROIs. The complete tumor ROIs were then reviewed by the radiologist before texture analysis.

8.2.3 Texture Analysis

Texture analysis was performed using a software called LIFEx with built-in first and second order texture features.²³ The CT portal venous phase scans were first resampled to a voxel size of 1mm, and absolute boundaries using the minimum and maximum CT numbers of the ROIs were used. 2D texture analysis was used with no binning. The ROIs' CT density values in HU were referred to as "CT number" in LIFEx.

To account for the effects of the patient-by-patient variations and evaluate any possible inconsistencies in the imaging acquisition process, a few normalization and control testing steps were performed. Physical tumor size change before and after light treatment was reported with no considerable changes to ensure a fair comparison between the baseline CT scan and post-treatment scans as ROI sizes could affect texture analysis. Recommended resampling to 1mm voxel size was done on all scans which previously had a range of pixel spacing in between 0.742 and 0.859 mm. The time differences between the two scans with respect to the nature of PDAC tumor progression were considered as

mentioned in Section 8.2.1 and the Discussion section. Contrast media concentration variation was tested by examining the liver and the spleen ROIs from the pre-treatment and post-treatment scans. Mean and standard deviation of CT numbers for these organs were reported in **Figure 8.4** and the changes before and after treatments were less than 7% for most patients (except for Patient 06). This average change ($6.6 \pm 2.6\%$) was considerably smaller than the average changes observed in the tumor regions ($14 \pm 7.3\%$), which confirmed that in the tumor regions, treatment-induced changes were dominant. Patient-by-patient variations were accounted for in the statistical analysis. ROC analysis with leave-one-out cross-validation and the generated ROC curve for combined classifiers provided evidence for PDP effects in most patients despite Patient 01 as an inherent outlier, which was discussed in the Discussion section.

8.2.4 Statistical Analysis

A student's t-test was used to compare the differences in means without the assumption of equal variance using the two-tail analysis with $\alpha = 0.05$. Combined classifiers to classify pre-treatment vs post-treatment CT images were then developed using the statistically significant radiomic features. Radial basis function support vector machine (RBF-SVM) classifiers were optimized and evaluated using leave-one-patient-out cross validation. A custom Python script to perform model optimization and receiver operating characteristic (ROC) analysis was developed using Scikit-Learn.²⁹ Briefly, the dataset was organized by CT image with the previously identified statistically significant radiomic features. Additional parameters were the patient ID which was assigned after anonymizing and randomizing patient data, and a binary label for pre vs post-treatment image. Iterating over the data by patient, RBF-SVM models were fit to all but the one patient withheld for

testing. After fitting, the model was used to predict the binary label all the images of the test patient. The probability output for each image alongside the ground truth labels were used to calculate an ROC curve for each patient. An average ROC curve was calculated by taking the mean and standard deviation at point on the curve across all patients. Area under the curve was calculated for each patient with the mean and standard deviation across all patients also reported.

8.3 Results

8.3.1 Post-treatment CT scans show a reduction in mean and standard deviation of tumor region values, suggesting a decrease in tumor density.

Figure 8.2A reports tumor size as a result of slice-by-slice segmentation on pre- and post-treatment CT scans. The tumor size ranges from 8 to 54 cm³, but there was not a significant change in size after treatment (paired t-test with p-value = 0.36). This finding is consistent with the patient's radiology reports. More interestingly, the average and standard deviation of CT number both show a statistically significant decrease after PDT treatment with the largest reduction of 33% in average HU and paired t-tests with p-values of 0.01 and 0.04, respectively (**Figure 8.2B-C**). Such reductions are good indicators that the tumor homogeneity is increased. The range of CT number maximum and minimum per tumor is also reduced in 5 out of 7 patients, again suggesting the intratumor variation has been decreased after PDT treatment. The overview of these first-order parameters shows a consistent trend suggesting a possible correlation between tumor density changes and PDT treatment effects, which could be quantified by texture analysis.

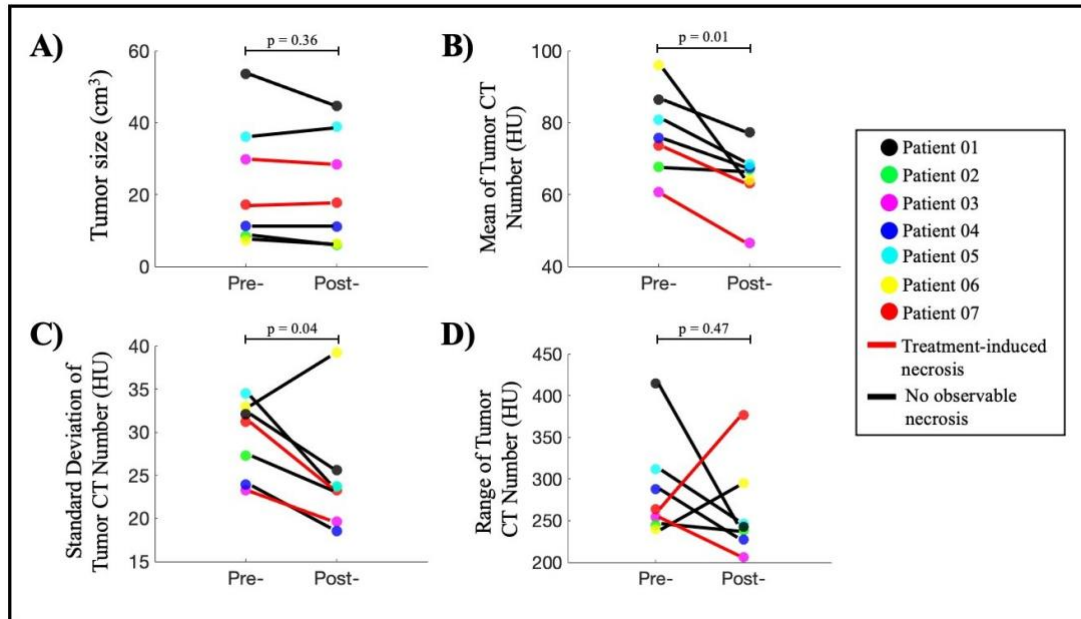


Figure 8.2 Overview of PDT-induced changes observed between pre- and post-treatment CT scans. A) Tumor size measured from 3D segmentation of tumors shows no significant change (paired t-test, p-value = 0.36). B) All patients show a reduction in mean tumor CT number, indicating the tumor density has decreased after PDT treatment (paired t-test, p-value = 0.01). C) 6 out of 7 patients show a reduction in standard deviation of tumor CT number, suggesting that the intratumor variation has decreased after treatment (paired t-test, p-value = 0.04). D) Range of CT number is decreased for 5 out of 7 patients which indicates the reduction of intratumor variation after PD (paired t-test, p-value = 0.47).

8.3.2 Texture analysis of pre-treatment CT scans can predict tumor areas that are pre-disposed to PDT induced necrosis response

From post-treatment CT scans, 40 tumor slices with a visible necrotic area as a result of photodynamic therapy treatment were identified (**Figure 8.3A**). For each tumor slice, manual segmentation performed by the radiologist separated the necrotic area in pink (PDT region) from the remaining of the tumor tissue in yellow (PDP region). These ROIs were then re-mapped back onto the pre-treatment CT scans in which texture analysis was performed. Results showed in **Figure 8.3B** provided the texture features that were

statistically significant between PDT and PDP regions. Those features included the tumor mean and standard deviation, GLCM contrast, dissimilarity and entropy, and GLRLM gray-level non-uniformity (paired t-test, $p < 0.001$).

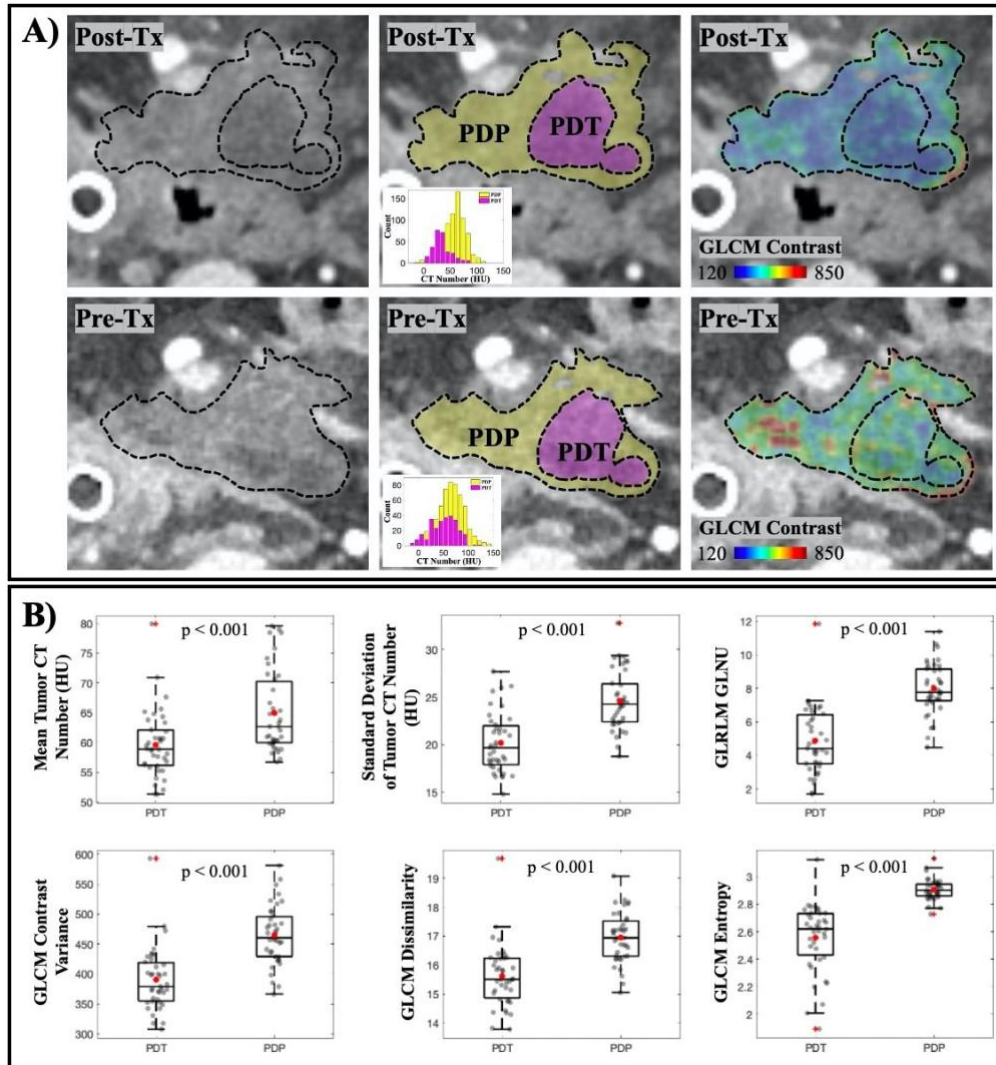


Figure 8.3 Treatment-induced necrosis areas could be predicted by texture analysis in the *Pre-Tx scan*. A) Visualization of tumor in Post-Tx (top row) and Pre-Tx (bottom row) CT scans. Observable necrosis area (PDT) in pink and remaining tumor region (PDP) in yellow are delineated in Post-Tx scans, which were then mapped onto Pre-Tx scans for texture analysis. GLCM Contrast feature for both regions in the Pre-Tx scans is illustrated to show that necrosis occurred at the area with lower contrast. B) Other first-order texture features that are found to be statistically significant when comparing the PDT and the PDP regions in Pre-Tx scans ($n = 40$ tumor slices).

8.3.3 Changes between pre-treatment and post-treatment CT scans in PDAC tumors indicate treatment effects, as referenced by other organ values.

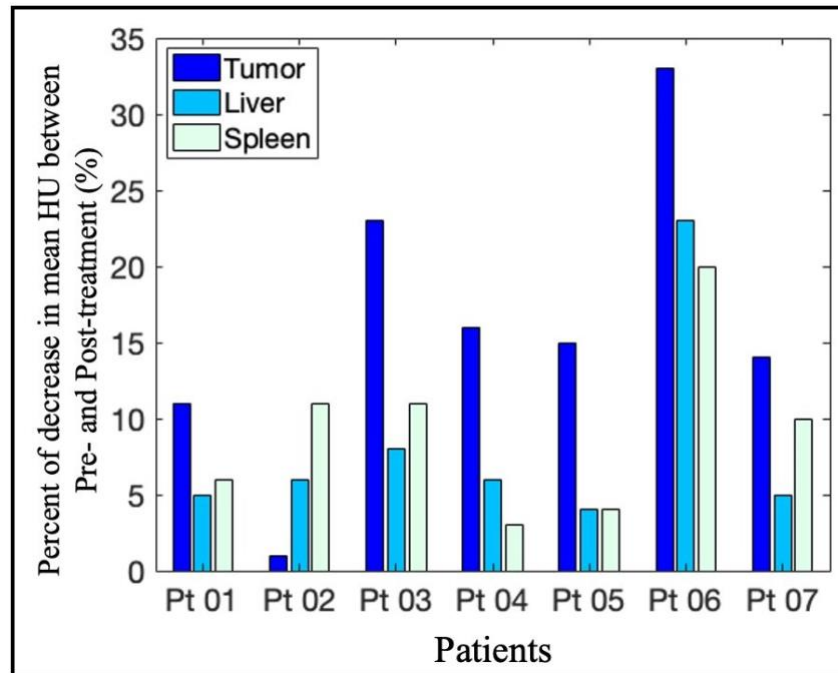


Figure 8.4. Percentage of changes after light treatment between pre-treatment and post-treatment scans in the PDP regions of tumors, as compared to the normal liver and spleen values. For each patient, the percentage change in CT mean was reported for the non-necrotic regions of PDAC tumor, liver and spleen. Mean CT number decreased in all ROIs from all patients, with the tumor regions consistently expressing the biggest reduction in CT number. This observation suggested that there were treatment-induced effects on the tumor CT numbers across the patient cohort.

Besides visible necrotic effects observed in some patients, it was noticeable that in patients without tumor necrosis, there was a significant reduction in mean CT number between pre-treatment and post-treatment scans (**Figure 8.4**). This decrease in CT number was shown to be significant when compared with that of neighboring normal organs such as liver and spleen. While changes in the liver and spleen across 6 out of 7 patients were $5.6 \pm 1.3\%$ and $7.7 \pm 3.3\%$, respectively, the decrease in non-necrotic (or PDP) tumor regions

on average was $14 \pm 7.3\%$. In some cases, the change in the tumor was more than doubled the changes in the liver and the spleen. It was important to realize that all ROIs from Patient 06 displayed more than 20% difference between the pre- and post-treatment scans, which was likely due to the 20 days elapsed before the acquisition of post-treatment scans as compared to within a week for other patients. Therefore, the differences observed in Patient 06 partially account for the rapid disease progression characteristic of PDAC. Overall, for most patients, the considerable difference in tumor CT number before and after treatment implies changes that are dominant by treatment effects and not just inherent variations in between different CT image acquisitions.

8.3.4 PDP effects could be quantified with texture analysis of pre- and post-treatment CT scans

Texture analysis was performed on non-necrotic tumor regions across all patients to study the underlying intratumoral changes as a result of PDT light treatment. **Figure 8.5A** illustrates the differences between pre-treatment and post-treatment CT scans. The first panel identified the ROIs in dotted yellow lines with corresponding histograms that showed a skewness to the left, indicating the decrease in mean CT number after treatment. A visualization of three GLCM parameters, homogeneity, contrast and dissimilarity, was also highlighted in **Figure 8.5A** to showcase the differences between pre-treatment and post-treatments scans that are not appreciated in a conventional CT scan evaluation. **Figure 8.5B** reported the six most statistically significant texture features when compared between pre- and post-treatment scans with 5 out of 6 features showing a p-value of less than 0.001. In **Figure 8.5C**, an ROC curve with corresponding AUC value for each of the six texture features was generated. The ROC curves accounted for all patients but Patient 01. This

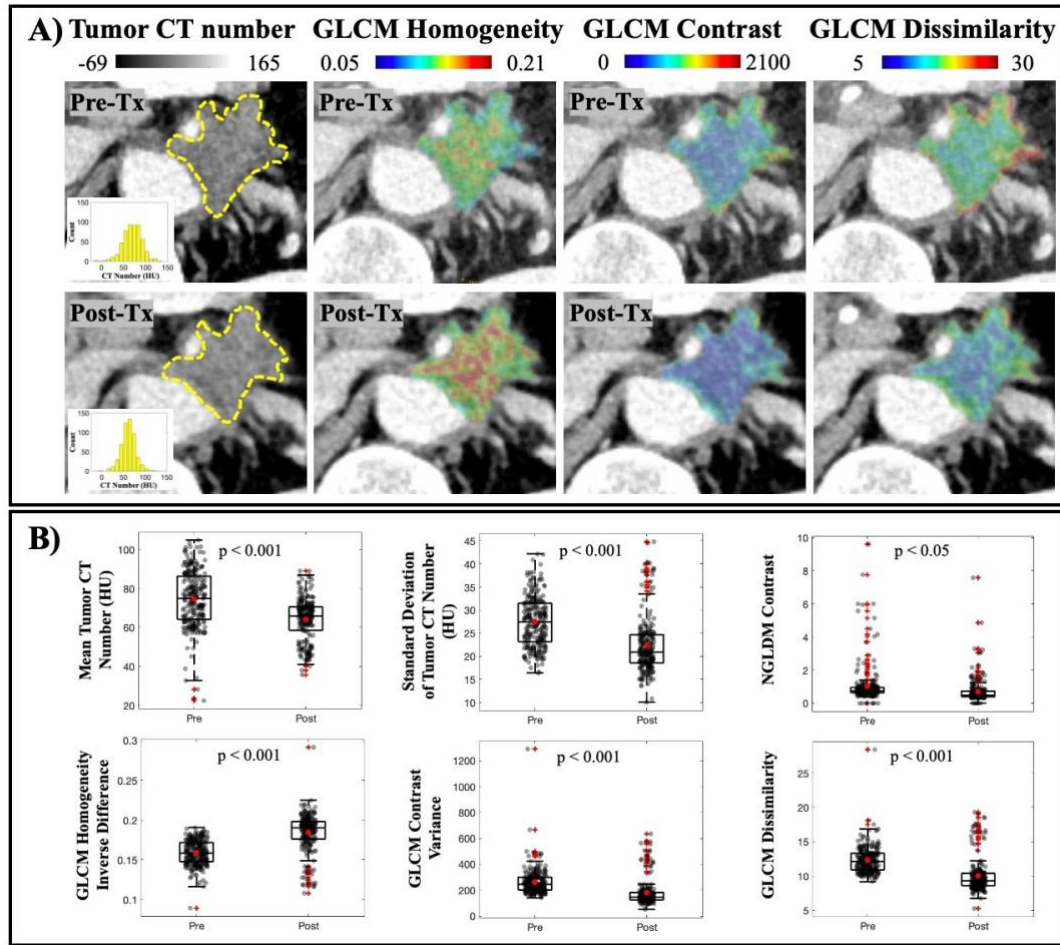


Figure 8. 5 PDP effects after light treatment are seen with texture analysis. A) A visualization of intratumor changes due to light treatment quantified by GLCM texture analysis. Means of tumor CT number before and after treatment are 74 ± 23 HU and 67 ± 17 HU, respectively. Tumor homogeneity is increased, while levels of contrast and dissimilarity are decreased, indicating a more uniform tumor attenuation profile. B) Texture features that showed a statistical significance between Pre-Tx and Post-Tx scans are reported ($n = 235$ tumor slices) patient was excluded from the classification process due to the large tumor volume, i.e., 130% larger than mean tumor size with tumor diameter reaching 5 cm. This considerably large tumor volume was convinced to not fully receive light treatment, therefore it was very unlikely to benefit from any PDP effects. Overall, **Figure 8.5C** with overlaid ROC curves for all radiomic features as single classifiers showed that second-order GLCM

features provided a better indicator of treatment effects as compared to tumor mean or standard deviation, emphasizing the need for texture analysis in this case.

Figure 8.5D displays the ROC curves for combining all six texture features into a classifier using the SVM model. Compared to using each feature as a single classifier with AUC value in the range of 0.75 to 0.80, a combination of all six yielded a better performance with a reported AUC value of 0.93 ± 0.07 . Furthermore, an attempt to validate this classification method is also reported using the leave-one-patient-out cross validation approach as described in Section 2.4. Each of the thinner ROC curves in **Figure 8.5D** was generated to evaluate this classification method given the limited patient data. The shaded area displaying ± 1 standard deviation was plotted to visualize the effect of patient-by-patient variation on the classification. While Patient 01 was excluded as explained

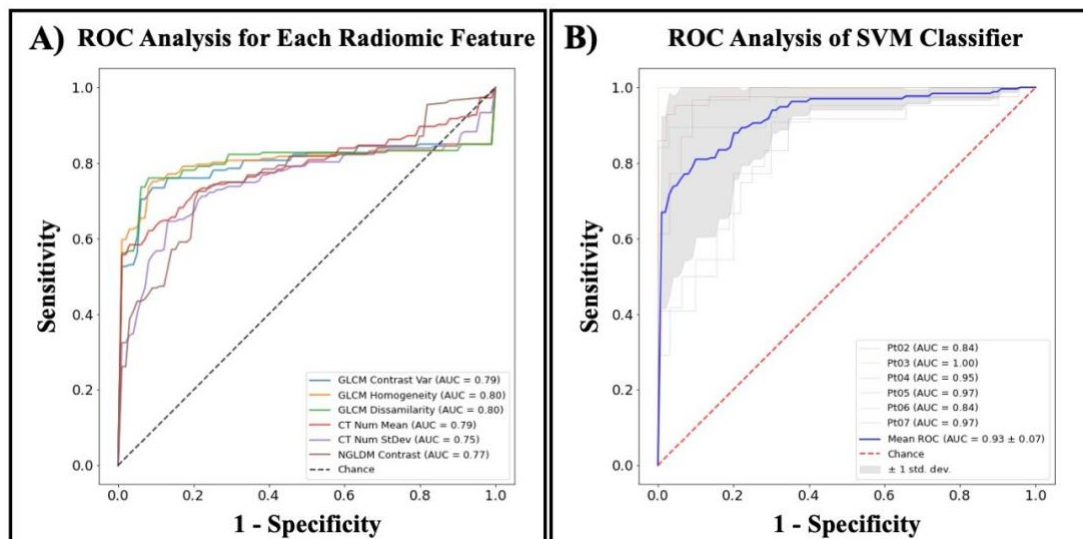


Figure 8.6 Classification for each feature and a combined classifier by SVM model A) Mean ROC curve for each reported feature calculated for all patients except for Patient 01, showing AUC values in the range of 0.75 to 0.80. B) Mean ROC curve of combined classifiers using SVM model in blue yielded a better performance than any single classifier (AUC value is 0.93 ± 0.07). Leave-one-patient-out cross validation ROC curves are showed for all patients except Patient 01, and the shaded area indicated the ± 1 standard deviation of this cross validation.

previously, the remaining patient cohort demonstrated a convincing classification with high AUC values in the range of 0.84 to 1.00. The ROC analysis in **Figure 8.5D** provided evidence that identified texture features could be of great use when combined as a single classifier to evaluate the subtle intratumoral changes as a result of photodynamic therapy treatment on non-necrotic tumor regions.

8.4. Discussion

PDAC aggressiveness combined with advanced stage at diagnosis has led to a desperate need for alternative therapeutic approaches. While research has focused on realizing new treatment options, it is equally important to identify effective approaches for accurate prediction of treatment outcomes and efficient assessment of treatment effects. In the case of photodynamic therapy, evidence have showed that the most promising treatment effects are on the microscopic level which requires additional imaging and/or special pathology staining of tumor samples. Low-dose photodynamic therapy, also known as photodynamic priming, in preclinical data promises the relieving effects on the tumor microenvironment. Compared to the most visible effect of cell death via necrosis which could be visualized on a patient's CT scan, the other benefits are more subtle, emphasizing the employment of further CT image analysis as validated in this study.

Texture analysis on pre-treatment CT scans focusing on the necrosis-induced tumor slices only showed that certain features could be used to predict tumor areas that are well-responded to photodynamic therapy. Since analysis was only performed on pre-treatment images of tumor slices that later on expressed necrosis, each tumor slice contained a PDT and a PDP region to create paired data samples (**Figure 8.3A**). Although the sample pool was limited ($n = 40$ tumor slices), paired samples assure that the differences reported are

due only to the intrinsic tumor physiology. **Figure 8.3B** reported the six most statistically significant features when compared between PDT and PDP regions in pre-treatment scans. These features, namely tumor mean/stdev, GLCM contrast, dissimilarity and entropy, and GLRLM GLNU, all showed a p-value of less than 0.001. They also consistently support the idea that well-responded tumor areas are less dense, less disordered and more uniformed. While the limited data might not give a convincing statement on using these features as future treatment outcome identifiers, the data has indicated, for the first time, that tumor density and homogeneity directly affect photodynamic therapy treatment outcome in clinical PDAC patients.

Data from **Figure 8.2** and **Figure 8.4** highlighted the intratumoral variation between pre-treatment and post-treatment CT scans as a result of photodynamic priming. Since all post-treatment CT scans were acquired 48 hours after PDT, tumor shrinkage was not observed. The relatively constant tumor size across most patients ensures that comparison between pre- and post-treatment scans are consistent. The significant reduction in patients' tumor CT number corroborates with preclinical findings that PDT alleviates desmoplasia,^{12,30} an intrinsic characteristic of PDAC tumors responsible for elevated pressure and stiffness.^{31,32} Interestingly, the decrease in the standard deviation of tumor CT number for most patients (**Figure 8.2C**) supports the hypothesis that tumor microenvironment heterogeneity, a physical barrier of intratumoral drug delivery efficiency, become more uniformed after PDT treatment. This change in tumor heterogeneity was not only reflected by the decrease in CT number standard deviation, but it was further supported by GLCM texture features such as Homogeneity, Contrast and Dissimilarity reported in **Figure 8.5**. While **Figure 8.5A** provides a visualization of

treatment-induced changes in tumor heterogeneity, the ROC analysis in **Figure 8.5C** confirms that these second-order texture features performed better at identifying subtle intratumoral changes after light treatment. Moreover, combining all six of these features using SVM model greatly improved the classification performance with mean AUC value of 0.93 ± 0.07 . The leave-one-patient-out cross validation was necessary given the limited patient cohort and the small patient-by-patient variation showed in **Figure 8.5D** confirmed that a combination of these classifiers provided a great tool to evaluate PDP treatment effects. The exclusion of Patient 01 with considerably large tumor volume in the classification process was validated by the physical limitations of photodynamic therapy, in which treatment efficacy relies on both the drug concentration and the amount of light exposure at the tumor site.

8.5 Conclusion

This study has validated the use of texture analysis on CT scans in predicting treatment outcome and assessing therapeutic effects on PDAC patients undergoing photodynamic therapy. The study shows that well-responded tumor regions were less dense, had lower average CT number and more uniform. These observations align with preclinical data and are classified via GLCM and GLRLM texture features. More importantly, the indiscernible, microscopic-level effects of photodynamic priming on alleviating tumor heterogeneity have been visualized and quantified by comparing pre- and post-treatment CT scans. Besides noticeable reductions in tumor CT number and its standard deviation, second-order GLCM features provided better classifiers, demonstrating for the first time with clinical data that tumor density and homogeneity played a key role in modulating PDT treatment effects.

8.6 Acknowledgements

This work was funded by NIH grant P01 CA084203.

8.7 References

1. Adamska, A., Domenichini, A. & Falasca, M. Pancreatic Ductal Adenocarcinoma: Current and Evolving Therapies. *Int. J. Mol. Sci.* **18**, (2017).
2. Kota, J., Hancock, J., Kwon, J. & Korc, M. Pancreatic cancer: Stroma and its current and emerging targeted therapies. *Cancer Lett.* **391**, 38–49 (2017).
3. Gillen, S., Schuster, T., Meyer zum Büschenfelde, C., Friess, H. & Kleeff, J. Preoperative/Neoadjuvant Therapy in Pancreatic Cancer: A Systematic Review and Meta-analysis of Response and Resection Percentages. *PLoS Med.* **7**, e1000267 (2010).
4. Siegel, R., Naishadham, D. & Jemal, A. Cancer statistics, 2013. *CA. Cancer J. Clin.* **63**, 11–30 (2013).
5. Karakullukcu, B. *et al.* Photodynamic therapy of early stage oral cavity and oropharynx neoplasms: An outcome analysis of 170 patients. *Eur. Arch. Oto-Rhino-Laryngology* **268**, 281–288 (2011).
6. Yano, T. *et al.* Photodynamic therapy as salvage treatment for local failure after chemoradiotherapy in patients with esophageal squamous cell carcinoma: A phase II study. *Int. J. Cancer* **131**, 1228–1234 (2012).
7. Kostron, H. Photodynamic diagnosis and therapy and the brain. *Methods Mol. Biol.* **635**, 261–280 (2010).
8. Huang, H.-C. *et al.* Photodynamic Priming Mitigates Chemotherapeutic Selection Pressures and Improves Drug Delivery. *Cancer Res.* **78**, 558–571 (2018).
9. Canti, G. *et al.* Antitumor immunity induced by photodynamic therapy with aluminum disulfonated phthalocyanines and laser light. *Anticancer. Drugs* **5**, 443–447 (1994).
10. Korbelik, M. Induction of tumor immunity by photodynamic therapy. *J. Clin. Laser Med. Surg.* **14**, 329–334 (1996).
11. Huang, H.-C. *et al.* Photodynamic therapy synergizes with irinotecan to overcome compensatory mechanisms and improve treatment outcomes in pancreatic cancer. *Cancer Res.* **76**, 1066 (2016).
12. Obaid, G. *et al.* Impacting Pancreatic Cancer Therapy in Heterotypic in Vitro

Organoids and in Vivo Tumors with Specificity-Tuned, NIR-Activable Photoimmunonanoconjugates: Towards Conquering Desmoplasia? *Nano Lett.* **19**, 7573–7587 (2019).

13. Jermyn, M. *et al.* CT contrast predicts pancreatic cancer treatment response to verteporfin-based photodynamic therapy. *Phys. Med. Biol.* **59**, 1911–1921 (2014).
14. Gillies, R. J., Kinahan, P. E. & Hricak, H. Radiomics: Images are more than pictures, they are data. *Radiology* **278**, 563–577 (2016).
15. Lambin, P. *et al.* Radiomics: The bridge between medical imaging and personalized medicine. *Nature Reviews Clinical Oncology* **14**, 749–762 (2017).
16. Rizzo, S. *et al.* Radiomics: the facts and the challenges of image analysis. *European Radiology Experimental* **2**, (2018).
17. Chen, X. *et al.* Assessment of treatment response during chemoradiation therapy for pancreatic cancer based on quantitative radiomic analysis of daily CTs: An exploratory study. *PLoS One* **12**, e0178961 (2017).
18. Cozzi, L. *et al.* Computed tomography based radiomic signature as predictive of survival and local control after stereotactic body radiation therapy in pancreatic carcinoma. *PLoS One* **14**, e0210758 (2019).
19. Dalal, V. *et al.* Radiomics in stratification of pancreatic cystic lesions: Machine learning in action. *Cancer Letters* **469**, 228–237 (2020).
20. Rhim, A. D. *et al.* Stromal Elements Act to Restrain, Rather Than Support, Pancreatic Ductal Adenocarcinoma. *Cancer Cell* **25**, 735–747 (2014).
21. Feig, C. *et al.* The pancreas cancer microenvironment. *Clin. Cancer Res.* **18**, 4266–76 (2012).
22. Neesse, A., Algül, H., Tuveson, D. A. & Gress, T. M. Stromal biology and therapy in pancreatic cancer: a changing paradigm. *Gut* **64**, 1476–1484 (2015).
23. Nioche, C. *et al.* Lifex: A freeware for radiomic feature calculation in multimodality imaging to accelerate advances in the characterization of tumor heterogeneity. *Cancer Res.* **78**, 4786–4789 (2018).
24. Cheng, S.-H., Cheng, Y.-J., Jin, Z.-Y. & Xue, H.-D. Unresectable pancreatic ductal adenocarcinoma: Role of CT quantitative imaging biomarkers for predicting outcomes of patients treated with chemotherapy. *Eur. J. Radiol.* **113**, 188–197 (2019).
25. Eilaghi, A. *et al.* CT texture features are associated with overall survival in

- pancreatic ductal adenocarcinoma - a quantitative analysis. *BMC Med. Imaging* **17**, 38 (2017).
26. Sandrasegaran, K., Lin, Y., Asare-Sawiri, M., Taiyini, T. & Tann, M. CT texture analysis of pancreatic cancer. *Eur. Radiol.* **29**, 1067–1073 (2019).
 27. Mackin, D. *et al.* Effect of tube current on computed tomography radiomic features. *Sci. Rep.* **8**, 2354 (2018).
 28. Fave, X. *et al.* Preliminary investigation into sources of uncertainty in quantitative imaging features. *Comput. Med. Imaging Graph.* **44**, 54–61 (2015).
 29. Pedregosa FABIANPEDREGOSA, F. *et al.* *Scikit-learn: Machine Learning in Python* Gaël Varoquaux Bertrand Thirion Vincent Dubourg Alexandre Passos PEDREGOSA, VAROQUAUX, GRAMFORT ET AL. Matthieu Perrot. *Journal of Machine Learning Research* **12**, (2011).
 30. Li, L. *et al.* Photosensitizer-Encapsulated Ferritins Mediate Photodynamic Therapy against Cancer-Associated Fibroblasts and Improve Tumor Accumulation of Nanoparticles. *Mol. Pharm.* **15**, 3595–3599 (2018).
 31. Nieskoski, M. D. *et al.* Collagen Complexity Spatially Defines Microregions of Total Tissue Pressure in Pancreatic Cancer. *Sci. Rep.* **7**, 10093 (2017).
 32. Vincent, P. *et al.* High-resolution ex vivo elastography to characterize tumor stromal heterogeneity in situ in pancreatic adenocarcinoma. *IEEE Trans. Biomed. Eng.* 1–1 (2020). doi:10.1109/tbme.2019.2963562

Chapter 9: Conclusion

9.1 Overview

Previously, each chapter has presented a study relevant to the thesis objectives and addressed the corresponding key conclusion points. In this chapter, the thesis work is summarized and discussed with respect to the 4 Specific Aims established in Chapter 1.

For each of the Aims, 3 main points are presented:

1. Macroscopic view of the results and how they fit in with current relevant research effort
2. Limitations of the work in terms of technical development, experimental designs, and assumptions or any considerations that were not accounted for
3. Recommendations for future improvements and future research directions

9.2 Conclusion for Aim 1

Aim 1: Image wide-field tumor stiffness heterogeneity at transport-relevant resolution to investigate the relationship between tumor stiffening, desmoplasia and drug transport

9.2.1 Results of Aim 1 from a Macroscopic View

As mentioned in Chapter 1, there has been considerable research into characterizing how solid tumor biomechanics is associated with intra-tumoral pressure and the interrelationship between SS and IFP. However, discrete probe measurements of tissue pressure, although accurate in nature, can only account for regional assessments, which does not provide insight into the overall tumor spatial heterogeneity of these values. With evidence showing drastic local variations in tumor pressure, it is possible that biomarkers

of the tumor biomechanics can be used to capture insights about the heterogeneity. The results from Aim 1 have demonstrated that tumor stiffness satisfies these conditions. A strong correlation between tumor stiffness and collagen was established, and more importantly, the inverse relationship between stiffness heterogeneity and drug distribution was demonstrated. These findings confirmed, that from a tumor pathophysiology standpoint, tumor stiffness is the more relevant indicator of any tumor drug transport barriers, than would be interstitial pressure or other measures.

Furthermore, the field of elastography has advanced with novel approaches to stiffness imaging that are both non-invasive and wide field. The high stiffness heterogeneity inherent in PDAC tumors necessitates whole-tumor sampling at transport-relevant resolution (hundreds of microns) over techniques that yield microscopic information from a limited field of view. The recent advancements such as UE and MRE hold some promise for clinical translation of stiffness imaging for PDAC patients, although they typically suffer from relatively low spatial resolution.

9.2.2 Limitations of Aim 1

Even though EVE system was able to generate whole-tumor stiffness heterogeneity map at high resolution, the mechanism remains a point-probe based approach, with considerable acquisition time required due to the uneven surface of stiff PDAC tumors. While measurements are not destructive to the specimen, sample preparation steps such as gelatin embedding and tumor cutting to reveal a flat surface are not negligible tasks and require some experience and technique development. Since the raw data collected is pressure at different compression displacements, a conversion factor to convert from pressure data to stiffness values is required. In Aim 1, this conversion factor was established using a series

of phantom studies and only pressure values in the range of PDAC tumor tissue were accounted for. Thus, more calibration will be necessary for biological samples or tumor organoids that are much softer than xenograft PDAC tumors. Still the values obtained for this part of the work were realistic and likely accurate, and regional relative differences across a tumor would always be valid.

9.2.3 Recommendations and Future Directions for Aim 1

If the system was to be used with much softer samples (< 5kPa), a more comprehensive phantom study should be conducted so that the conversion factor between pressure readings and absolute stiffness values was more robust down to these lower values. Major improvements with acquisition time could also be considered and one possible direction involves acquiring tumor surface roughness variation maps. There have been studies to image the topography of biological samples¹, and with this information as a LabVIEW input, the system could greatly reduce the time taken to detect the tumor surface. Currently this is responsible for the largest fraction of the acquisition time.

9.3 Conclusion for Aim 2

Aim 2: Visualize and quantify PDAC tumor collagen network from fresh samples using fluorescence imaging with ultraviolet illumination

9.3.1 Results of Aim 2 from a Macroscopic View

Collagen imaging is a mature research field with advanced techniques capable of capturing a large field of view at microscopic resolution. However, these imaging systems come at a high cost and with complicated optics. Meanwhile, fluorescence imaging with ultraviolet excitation offers a simple yet effective approach to wide-field imaging of tissue structures

at microscopic resolution and with inherent depth sectioning on the surface of thick samples. Results from Aim 3 demonstrated that such imaging technique could be employed to visualize PDAC tumor stroma, for the first time. Although this method is highly reproducible and more research effort has been put into pushing it towards clinical translation, it is unlikely that UV-fluor could be utilized to extract tumor stromal information in a clinical setting because of the logistics of imaging just a surface with applied dyes. While it is possible to make the imaging apparatus more compact or turn it into a hand-held device, the trade-off between depth of field and resolution is governed by optics and therefore it is not possible to compromise. Any specimen would either need to be flat or use multiple optical sectioning to see into it. Still, UV-fluor has proven to be an excellent imaging tool for ex vivo assessment of fresh biological samples at whole-specimen field of view and preserving microscopic spatial resolution. The system is capable of capturing the PDAC stromal heterogeneity from fresh bulk tissues in a non-destructive manner so that conventional pathology staining could still be performed subsequently. These benefits are highly valued as an experimental tool, especially in pre-clinical small animal studies where whole-tumor samples are a reasonable size. Drug and treatment studies involving fibroblast depletion also benefited from the advantages UV-fluor. In particular, the study of photodynamic priming treatment, with the goal of reducing PDAC stroma, was conducted on nude mice presented in Aim 3 of this thesis work and this tool was an ideal fast imaging pathway to document these macroscopic changes in the tumors.

9.3.2 Limitations of Aim 2

Due to the considerable tumor surface irregularity and the limited depth of field of

microscopy lenses (up to 10 μm for a 10X lens), acquisition of a large image stack at each location is required to minimize out of focus pixels. While the depth of field correction algorithm used in Aim 2 was very robust, stiff PDAC tumors resulted in extreme surface uneven imaging planes. Despite a large z-stack acquisition and an open-top epi-illumination setup, this still did not yield satisfactory image quality without extensive use of software postprocessing. Meanwhile, illumination source using LEDs in the UVC range is cost-effective but required an exposure time of 100 ms for the illuminances used in the study. Considering that current UV-LED technology offers very limited intensity, this exposure time is quite reasonable, but still less than ideal when image acquisition demands required a large image stack of vertical focusing depths at each location in the image. Although again, for laboratory work, this was manageable and still faster than post processing of tissues by a pathology research service.

The staining procedure was well-established to highlight collagen strands, but there is room for improvement to ensure even more consistent staining quality. It was noticeable that due to the highly uneven surface, residual of the staining mixture could be left behind on top of the tumor surface if washing was not thorough. This remaining staining dye cocktail could contribute to the low image contrast problem. Post processing of the raw image data was developed specifically for PDAC collagen profiles, so more training data would be necessary if the algorithm was applied to different types of tissues that have different collagen characteristics. Additionally, this computational technique was demonstrated with only BxPC-3 tumor line in the study, and so could need alteration if tested on other tumor lines with significantly different characteristics.

9.3.3 Recommendations and Future Directions for Aim 2

Since image contrast remained the biggest problem throughout this study, a better imaging setup or cutting technique to address the unevenness of the stiff tumor surface would be beneficial for improvement. It would be convenient to keep the open-top setup so stiffness mapping and collagen mapping are streamlined. However, an external force applied on top of the tumor surface to flatten it out will be necessary to reduce the image stack size and minimize out of focus pixels. Alternatively, a better approach for collagen imaging would be to consider pressing the tumor upside-down on a UV-transparent platform with illumination sources and the camera positioned from the bottom-up. This setup would ensure a flat imaging surface even though the exposure time per acquisition might be extended due to the attenuated intensity of UV-LEDs when illuminated through a UV-glass platform. This compromise should be minor, as compared to the larger problems with suitable image contrast. Therefore, it is recommended that current imaging setup is improved with reducing the tumor surface irregularity as the top priority. Solving this problem will not only help increasing the image quality but will also should result in better collagen quantification from post-processing.

9.4 Conclusion for Aim 3

Aim 3: Evaluate collagen and stiffness modulation effects by photodynamic therapy treatment to enhance intratumoral drug uptake

9.4.1 Results of Aim 3 from a Macroscopic View

The benefits of low-dose PDT, or PDP, have been demonstrated to induce intratumoral changes mostly on the microscopic level.^{2,3} Strong evidence of PDP working synergistically with chemotherapy as a combination treatment suggested cellular level

effects in regulating gene expressions and signal pathways. Desmoplasia modulation induced by PDP has been recently introduced and results from Aim 3 are among the first studies to document this TME remodeling effect. Beyond the treatment-induced collagen depletion as reported in both this thesis work and other studies⁴, stiffness heterogeneity normalization and average stiffness reduction by PDP treatment are established for the first time. This finding not only supports early evidence of PDP-induced stromal depletion but more importantly, it also reaffirms the proposal of using tumor stiffness information as an indicator of tumor drug uptake as presented throughout this thesis work. The impact is further elucidated when considering the promise of elastography imaging in clinical translation as compared to the additional burden from costly and time-consuming procedures of immunohistochemistry staining and/or imaging techniques to provide cellular level information to confirm PDP treatment effects. It is even more exciting that texture analysis of tumor stiffness data showed a reduction in tumor heterogeneity in the treated mice, which has motivated the work in Aim 4 and supported the use of texture analysis of clinical patient data to quantify PDP effects.

9.4.2 Limitations of Aim 3

While the results of Aim 3 support a consistent relationship between tumor stiffness, collagen content and drug uptake established throughout this thesis work, the modulation effects induced by PDP treatment of PDAC xenograft mouse model were inferred from a small number of animals per group with only BxPC-3 tumor line being investigated. Consistent tumor size between the control and the treated group as an indicator of equivalent tumor progression required both a staggering tumor implantation schedule and frequent tumor size monitoring. This study employed tumor palpation methods, for which

experience on working with PDAC orthotopic models is needed, due to the subtle nature of pancreatic tumor location. The use of ultrasound imaging to monitor tumor size would yield a more accurate and unbiased approach and would not require prior experience. The current xenograft model used immunocompromised mice, which were not ideal to investigate immune cell recruitment as a potential PDP effect, but served as a reasonable compromise for studying the biophysical nature of the treatments.

9.4.3 Recommendations and Future Directions for Aim 3

While our study was reasonably solid, a larger number of animals per group would be beneficial to validate the findings reported in this study. Additional PDAC tumor lines could also be investigated, as desmoplasia complexity has been observed to vary significantly among different phenotypes. While preliminary data showed dextran perfusion as a marker for tumor drug uptake, it would be more convincing to use a chemotherapy drug fluorescence, or tagged with a fluorophore if needed, to assess tumor drug distribution. Several chemotherapy agents have inherent UV fluorescence and could be used for this purpose, although gemcitabine does not seem to have this. The current dose of PDT drug and light has resulted in approximately 20% necrosis, therefore an even lower dose of PDT could be administered in future studies to truly represent the sub-lethal concept of PDP treatment.

One possible method to determine the threshold of low-dose PDT effects is to mark the tumor position when exposed to light treatment during surgery. Then, treatment-induced modulation on tumor collagen, stiffness, vasculature and drug uptake should be analyzed radially outward to visualize the gradient of PDP effects with respect to attenuated light intensity. If resources permitted, it would be beneficial to conduct the same

experiment with transgenic mouse models so that the effects on immune cells could be examined, which would be valuable to the assessment of combination treatment with PDT and immunotherapy.

9.5 Conclusion for Aim 4

Aim 4: Quantify photodynamic priming effects using radiomics analysis on clinical PDAC CT scans

9.5.1 Results of Aim 4 from a Macroscopic View

While preclinical findings have reported supporting evidence that low-dose PDT, or PDP, results in tumor growth inhibition either via targeting certain cellular signaling pathways or the tumor microenvironment, clinical outcomes of PDAC patients receiving PDT treatment have been limited to examining macroscopic changes such as necrosis, tumor size and neighboring major vasculature involvements via CT scans. Although the aforementioned tumor changes are reliable indicators of PDT treatment effects, they do not reflect the PDP benefits that hold the clinical promise of priming the PDAC tumors for combination treatment. Results from Aim 4 have demonstrated, for the first time, that PDP effects could be observed and quantified by radiomics analysis in PDAC patients receiving PDT treatment. Besides a strong agreement between clinical data and preclinical findings, the convenience of information extraction directly from the standard CT scans has made this approach even more attractive and feasible for clinical translation. Being able to visualize and quantify the tumor priming effects efficiently with CT radiomics marks an important step towards realizing PDT as a neoadjuvant therapy for combination treatment.

9.5.2 Limitations of Aim 4

Although extra control and validation testing steps were taken to account for the inherent patient variability, it is important to recognize the limited patient cohort presented in this study. Tumor segmentation was performed by a trained, board-certified radiologist. However, human bias could be considered present as segmentation results came from one only one radiologist, and a more detailed analysis for a radiology audience would require more readers. While LIFE_x software offers a streamlined, user-friendly interface to perform segmentation and texture analysis, it is not open-source, so information on the back-end code was only given via the user manual. Thus there is little control of the analysis algorithms, but given the widespread use of this package in publications it was felt that this would be acceptable for the introductory level of this study. Quantitative normalization methods were considered but they were not fully executed on raw CT data, so only classification process to account for patient variability were performed on texture results. Lastly, it was assumed that most non-necrotic regions of the tumors received some at least partial PDT treatment, as there were no records of the exact optical fiber insertion location. This assumption was fair to small and medium tumors but is likely not that accurate with considerably large tumors, as observed in Patient 01. In the future, more detailed studies might keep track of the insertion location at least, to determine the area of the tumor to track for radiomic signature changes.

9.5.3 Recommendations and Future Directions for Aim 4

It is crucial that efforts are put into recruiting more patients in prospective studies, so that the proposed combined classifier by the SVM model is properly validated for future use of determining treatment-induced tumor homogeneity. While the current study has shown evidence that changes in tumor CT numbers were dominant by light treatment, it would be

beneficial to apply a normalization method to account for CT scan variation factors, whether introduced by unexpected errors in scanning techniques or intrinsic patient variability. To realize these extra steps in data pre-processing, an open-source texture analysis package would be useful so that implementation of normalization, control and validation testing becomes easier to implement. The assumption used in this study that all non-necrotic tumor regions partially received PDT treatment and thus were classified as PDP regions could be improved if the exact location of the light fiber insert was identified. Further estimations of tumor regions receiving low-dose PDT would be more accurately determined using tools such as the light modeling described in Jermyn et al to approximate the treatment dose given at a certain location.⁵ To acquire such information would require additional collaboration and expertise from the clinicians, which was feasible as proven in the past studies. Therefore, it is highly recommended that future studies regarding PDT treatment for PDAC patients consider acquiring an extra low-dose CT scan to help identify the fiber location.

9.6 Final Remarks

PDAC survival rate has remained unchanged for the past 30 years despite considerable efforts to characterize the disease progression and explore potential treatment regimens. The well-established complexity of PDAC tumor biology and physiology has called for combination treatments as an effective solution to simultaneously and synergistically target multiple pathways of tumor progression. The findings presented in this thesis work support the use of photodynamic therapy as an efficient neoadjuvant step that primes the PDAC tumors for subsequent treatments. In this study we primarily examined the potential for priming to relieve the tumor heterogeneity and enhance intratumoral drug distribution. By

focusing on the tumor mechanical microenvironment, the work provided consistent evidence throughout all Aims to support the inverse relationship between stiffness heterogeneity and intratumoral drug uptake, inferring the use of tumor stiffness as a surrogate for drug delivery efficiency. A strong emphasis was placed on acquiring heterogeneity information at a whole-tumor field of view and transport-relevant resolution to truly capture the complexity of drug delivery mechanism in PDAC.

With the ultimate goal of translational research, this thesis has tested two novel approaches to tackle assessment of PDAC treatment efficacy. Specifically, the use of stiffness imaging to predict tumor drug delivery is well-supported and deemed highly applicable by the growth of promising elastography techniques suitable for clinical settings. However, because of resolution limitations in the clinical techniques for elastography with ultrasound or MRI, the focus here was on pre-clinical imaging of response with direct in situ elastography and UV-fluorescence stromal imaging. This thesis has also highlighted the potential of texture analysis in quantifying tumor homogeneity improvements after photodynamic therapy treatment of PDAC patients, all of which are feasible via conventional CT scans. Even though clinical adoption of these two proposed ideas is far from realized, the findings have set a stepping stone towards improving PDAC treatment evaluation.

9.7 References

1. Wainwright, D. K., Lauder, G. V. & Weaver, J. C. Imaging biological surface topography in situ and in vivo. *Methods Ecol. Evol.* 8, 1626–1638 (2017).
2. Huang, H.-C. et al. Photodynamic therapy synergizes with irinotecan to overcome compensatory mechanisms and improve treatment outcomes in pancreatic cancer. *Cancer Res.* 76, 1066 (2016).

3. Huang, H.-C. et al. Photodynamic Priming Mitigates Chemotherapeutic Selection Pressures and Improves Drug Delivery. *Cancer Res.* 78, 558–571 (2018).
4. Obaid, G. et al. Impacting Pancreatic Cancer Therapy in Heterotypic in Vitro Organoids and in Vivo Tumors with Specificity-Tuned, NIR-Activable Photoimmunonanoconjugates: Towards Conquering Desmoplasia? *Nano Lett.* 19, 7573–7587 (2019).
5. Jermyn, M. et al. CT contrast predicts pancreatic cancer treatment response to verteporfin-based photodynamic therapy. *Phys. Med. Biol.* 59, 1911–1921 (2014).

Appendices

This section includes the important Matlab codes that were used for image processing tasks performed in the projects highlighted in Chapter 3 through 7. The majority of data was obtained via a microscope or RGB cameras, with the exception of stiffness data being collected by LabVIEW programming that integrated the FISO pressure signaling module with a translational stage. The codes included below are not exhaustive of scripts that were used to perform data analysis in this thesis, but they are the most representative of central imaging processing tasks required to obtain the experimental results.

A.1-Converting pressure reading data imported from Excel into stiffness maps

```
%% Load data
filename=fullfile('..','Excel','20200827','M02.xlsx'); %specify path to
excel file
xlRange='N:N';
sheet = 1;
data = xlsread(filename,1,'A:A');
X = 29; %input the X-Y size of tumor based on translational stage step
(1 step = 300 micron)
Y = 24;
%% Delete all pre-allocated data (value = 95) while the stage is moving
before the pressure readings are taken
ind95 = find(data==95);
delind = zeros(numel(ind95),1);
for i = 1:numel(ind95)-1
    indtemp = ind95(i);
    if data(indtemp+1)==95
        delind(i) = indtemp+1;
    end
end
delind(delind==0) = [];
data(delind)=[];

%% Get number of points and Rsquare of linear fit
cycle = 4;
%Find index of 95kPa
ind95 = find(data==95);
%Check to find where pins are
temp = 1:4:numel(ind95)*4;
temp = temp';
vdiff = temp-ind95;
indpin = find(vdiff ~= 0);
vec = zeros(10000,1);
```

```

data2 = data;

%Add data to fill the pin holes
while ~isempty(indpin)
    ind = temp(indpin(1));
    data2 = vertcat(data2(1:ind-1),95,data2(ind:end));
    ind95 = find(data2==95);
    temp = 1:4: numel(ind95)*4;
    temp = temp';
    vdiff = temp-ind95;
    indpin = find(vdiff ~= 0);
end

%% Get Young's Modulus via calculating the slope of 3-point pressure
reading data
numpts = numel(ind95);
stress = zeros(3,1);
length = 0.5*10^-2; %0.5cm
strain = 6.3*(10^-6)*[15 20 25]'/length;
slope = zeros(numpts,1);
Rsquare= zeros(numpts,1);
for i = 1:numpts
    k = ind95(i);
    stress(:,1)=data2(k+1:k+3);
    [fitObj,gof]=fit(strain,stress,'poly1');
    Rsquare(i,1)= gof.rsquare;
    slope(i,1)=fitObj.p1;
end

%% Locate and index all negative YM values (occasionally the pressure
probe misrecords a value which makes YM a negative value)
ind = true(size(slope)); %true = good points, false = bad points

smean = mean(slope(:));
ind((slope<0)) = false; %negative slope = false
negind = find(slope<0); %index of slope < 0

%% Assign the average of the surrounding YMs to replace the negative
YMs
indsum = size(negind,1);
slopecorr = slope;
for i = 1:indsum
    k = negind(i); %index of negative slope
    kb = k-1; ka = k+1;
    while slope(kb)<0; kb = kb-1;end
    while slope(ka)<0; ka = ka+1;end
    slopecorr(k) = (slope(kb)+slope(ka))/2;
end

%% Turn into matrices/map using the X-Y values for each tumor
vecs = slopecorr;
[r1,c1] = size(vecs(1:end));
smap = reshape(vecs(1:end),[Y,X]);
smap2 = transpose(smap);

```



```

%% Visualize the map
figure
image(smap2, 'CDataMapping', 'scaled');
axis equal
axis off
colormap hot
caxis([0 max(slopecorr(:))])
set(gca, 'FontSize', 24)
set(gcf, 'Color', 'white')
colorbar
%% Save stiffness map (smap) as .mat files
mapfile = fullfile('..', 'Vectra', 'StiffnessMap', 'M02_map.mat');
%specify local file path
save(mapfile, 'smap2')
%load(mapfile, 'smap2')

```

A.2-Co-registration of image data using rigid transformation with Trichrome image data as the reference

```

%%Load data
animal = 'M02'; %animal name
%get stiffness map
dirraw = fullfile('..', 'Vectra', 'StiffnessMap');
dirinfo = dir(fullfile(dirraw, '*M02_map*'));
pfile = fullfile(dirraw, dirinfo(1).name);
load(pfile, 'smap2');

%get binary stiffness mask
mask = imread(fullfile('..', 'Vectra', 'StiffnessMask', 'M02_mask.tiff'));

%get Trichrome image data to use as reference
vinfo = dir(fullfile('..', 'Vectra', '10x_crop', '*M02*'));
co = imread(fullfile('..', 'Vectra', '10x_crop', vinfo(1).name));

%% Modify pmap to image for visualization
pmap = smap2.*mask;
%normalize double image to 0 - 1
pmapn = pmap./max(pmap(:));
pmapind = uint8(floor(pmapn * 255));
Map = jet(255);
pmaprgb = ind2rgb(pmapind, Map);

%% Match common points
cpselect(pmaprgb, co) %transform pmaprgb to co, co is the reference

%% Apply transformation
tform =
fitgeotrans(movingPoints, fixedPoints, 'nonreflectivesimilarity');
tformfile =
fullfile('..', 'Vectra', '10x_single_aligned', 'tform_smap', [animal
'.mat']);
save(tformfile, 'tform')
%load(tformfile, 'tform')
Jregistered = imwarp(pmaprgb, tform, 'OutputView', imref2d(size(co)));

%% Save transformed image out

```

```

Jregistered = imwarp(pmaprgb,tform,'OutputView',imref2d(size(co)));
dirim = fullfile('..','Vectra','10x_single_aligned','smap');
if exist(dirim,'dir')==0;mkdir(dirim);end
imname = [animal '_smap.tiff'];
imfile = fullfile(dirim,imname);
imwrite(Jregistered,imfile);

%% Apply tform to pmap (not just the image form of pmap)
Jregistered2 = imwarp(smap2,tform,'OutputView',imref2d(size(co)));
dirim = fullfile('..','Vectra','10x_single_aligned','transmap-
stiffness');
if exist(dirim,'dir')==0;mkdir(dirim);end
transmap = Jregistered2;
mapfile = fullfile(dirim,[animal '_transmap.mat']);
save(mapfile,'transmap');

```

A.3-Color segmentation on pathology images

```

% Color segmentation on pathology data to get blood vessels or Collagen
%% load data
animal = 'M05';
slice=1;
dirraw = fullfile('..','Vectra','10x_crop');
dirinfo = dir(fullfile(dirraw,'*M05_*'));
he = imread(fullfile(dirraw,dirinfo(slice).name));
[r,c,l] = size(he);
%% Convert from RGB to HSV
hehsv = rgb2hsv(he);
imshow(hehsv)
%% Segmentation in HSV space
h = hehsv(:,:,1);
s = hehsv(:,:,2);
v = hehsv(:,:,3);
mask = true(r,c);
mask(h<0.4)=false; % empirical HSV value cutoffs depending on the
structure
mask(h>0.7)=false;
mask(s<0.4)=false;
mask(v<0.3) =false;
imshow(mask)

%% Get rid of tiny clusters that are not structural information
mask2 = bwareaopen(mask,50);

%% Write out binary mask
segname = [animal '_C_mask.tiff'];
outfile =
fullfile('..','Vectra','10x_single_aligned','C_mask_hsv',segname);
imwrite(mask,outfile);

%% Visualize a region on original and segmented image as part of QA
process
im = he;
    imshow(im,[])
    a = imrect;

```

```

reg = wait(a);
x1 = floor(reg(2)); x2 = floor(reg(2)+reg(4));
y1 = floor(reg(1)); y2 = floor(reg(1)+reg(3));
im1 = im2double(he(x1:x2,y1:y2,:));
%im1 = im2double(collagen(x1:x2,y1:y2,:));
%im2 = coll2(x1:x2,y1:y2);
m = mask2(x1:x2,y1:y2);
im2 = hehsv(x1:x2,y1:y2,:);
im3 =cat(3,m.*im1(:,:,1),m.*im1(:,:,2),m.*im1(:,:,3));
figure
imshowpair(im1,im3,'montage')

```

A.4- Get lectin percentage from pathology images

```

% This script calculates lectin percentage area
%% Load data from local path
animal = 'M21';
dirraw = fullfile('..','Vectra','10x_single_aligned');
lec = imread(fullfile(dirraw,'L',[animal '_L.tiff']));
mask = imread(fullfile(dirraw,'Masks_corr_PDP',[animal
'_C_mask_corr_PDP.tiff']));
maskpdp = logical(mask);
he = imread(fullfile('..','Vectra','10x_crop',[animal '_C.tiff']));
lec = im2double(lec);

%% BG subtraction for lectin
imshow(lec)
title('Select background area')
a = imrect;
reg = wait(a);
close(gcf)
bgim = imcrop(lec,reg);
bg = mean(bgim(:));
lecn = lec-bg;
imshow(lecn)

%% Use C mask to get lectin signal
lecim = lecn.*maskpdp;

%% Get lectin by C mask
lec1 = imbinarize(lecim,X); %X = thresholding level
imshow(lec1)

%% QA step - make sure artifacts are eliminated
title('Select region of artifact')
a = roipoly(lec1);
lec1 = lec1-a;

%% Count pixel to get percentage
totalvec = find(maskpdp==1);
totalpix = length(totalvec);
lecimvec = find(lec1==1);
lecpix = length(lecimvec);
ratio = lecpix/totalpix*100

```

A.5-Collagen analysis to obtain structural information

```
%% Collagen analysis from Trichrome/UV-fluor images
%load data from local paths
animal = 'M05';
mt = imread(fullfile('..','Vectra','10x_crop',[animal '_C.tiff']));
cmask =
imread(fullfile('..','Vectra','10x_single_aligned','C_mask_hsv',[animal
'_C_mask.tiff']));
pdpmask =
imread(fullfile('..','Vectra','10x_single_aligned','Masks_corr_PDP',[an
imal '_C_mask_corr_PDP.tiff'])); %pdp = no necrosis
pdpmask=logical(pdpmask);
maskmt = cmask&pdpmask;

%% Get collagen binary mask from UV-fluor images
i=1;
imlist = dir(fullfile('..','Vectra','10x_crop','*.tiff'));
lalist = dir(fullfile('..','Vectra','labelmt','*.tiff'));
iname = imlist(i).name;
uv = imread(fullfile('..','Vectra','10x_crop',imlist(i).name));
la = imread(fullfile('..','Vectra','labelmt',['label_'
imlist(i).name]));
maskuv = la==4;
%% Get rid of tiny clusters
maskmt = bwareaopen(maskmt,20); %get rid of clumps smaller than X
pixels

%% Fill in holes on collagen strands for strand counting
im = maskmt;
im2 = ~bwareaopen(~im, 500);

%% bothat filtering
sebot = strel('disk',3);
imbot =imbothat(im2,sebot);
imsum = imbot+im2;

%% Merge all small holes within collagen strand
imsum3 = imcomplement(imsum2);
imcol = bwareaopen(imsum3,800);

%% Find dist of collagen to BG (which is an indicator of the collagen
strand thickness)
[d,ind] = bwdist(imcol); %dist of coll pixel to nearest BG
% dout = fullfile('..','Data','duv',['d_' iname(1:end-4) 'mat']);
% save(dout,'d')

%% Break up weak strands by thresholding - MT
im = d;
im(im<1)=0;
immask = bwareaopen(im,2000);
colmap = im;
```

```

%% Get percentage of collagen
total = size(colmap,1)*size(colmap,2);
colind = find(colmap~=0);
colper= length(colind)/total

%% Get skeleton of colmap
core = bwskel(logical(colmap), 'MinBranchLength',100);
se = strel('disk',5);
core2 = imdilate(core,se);
bp = bwmorph(core, 'branchpoint');
bpbreak = core-bp;

%% QA step - Double check the segmentation
imshow(labeloverlay(mt.*uint8(logical(colmap)),core2, 'Colormap', 'hot'))

%% Count regions based on connectivity
cc = bwconncomp(bpbreak);
ccout = fullfile('..', 'Vectra', '10x_single_aligned', 'cc_new', [animal
'_cc.mat']);
save(ccout, 'cc')

%% Load structure
load(fullfile('..', 'Vectra', '10x_single_aligned', 'cc_new', [animal
'_cc.mat']));

j=1;
numob = cc.NumObjects;
regind = cc.PixelIdxList; % 1 x numob cell array
regcount = labelmatrix(cc);
s = regionprops(cc, 'Orientation', 'MajorAxisLength', 'MinorAxisLength',
'Eccentricity', 'Centroid', 'Area', 'PixelIdxList'); % all collagen
strands

%% Get collagen fiber length
len = [s.MajorAxisLength]; %length in pixel
lenm = len.*1; %1pix = 0.35 micron, scaling depending on pathology or
UV-fluor images
figure
histogram(lenm,30, 'FaceColor', 'k', 'EdgeColor', 'k')
set(gca, 'FontSize', 25)

%% Get collagen thickness
thic = zeros(length(s),1);
for k = 1:numel(s) %go thru all strands in one image
    vecind = s(k).PixelIdxList; % ind of all pixels in the region
    dtemp = colmap; %distance map
    maskreg = regcount==k; %mask of each strand
    vec = dtemp(maskreg);
    thic(k)=mean(vec(:)); %average thickness of each length
end

thicm = thic.*1; % 1pix = 0.35micron
%figure
histogram(thicm.*1,30, 'FaceColor', 'k', 'EdgeColor', 'k')
set(gca, 'FontSize', 25)

```

```
%% Get collagen orientation
ori = [s.Orientation];
histogram(ori,20,'FaceColor','k','EdgeColor','k')
set(gca,'YTickLabel',[]);
set(gca,'FontSize',25)
```